Oxygen Reduction Reaction by Copper Complex based Electrocatalysts

A Dissertation Presented for the

Doctor of Philosophy

Degree

The University of Tennessee, Knoxville

Congling Zhang

May 2015

Acknowledgements

Over the past four and half years I have received support and encouragement from a large number of people. I cannot list all of them here, but I am grateful for their contribution.

First I would like to thank my advisor, Professor Thomas Zawodzinski for providing resources to make this work possible, for teaching me the philosophy of scientific research, for allowing me to work at my own pace and for the opportunities of going to multiple conferences. My next thanks go to Dr. Gabriel Goenaga for teaching me the basic skills of electrochemical testing of electrocatalysts at the beginning of my work. Without his devotion, the lab would not have been operated in a clean and organized environment. I would like to thank the help from Dr. Shane Foister in the catalyst synthesis in his lab, from explaining the reaction mechanism, controlling reaction conditions to using ICP. I owe special thanks to Dr. Jamie Lawton for teaching me using EPR, for her great patience in guiding me and for many in-depth discussions about experiments, results and papers. I would also like to thank my committee member Dr. Alex Papandrew for his professional advice and kind help.

There are a number of people I want to thank in Z group. This is a group full of helpful, friendly, creative and funny people who make an awesome environment to work at. I benefit a lot from the discussion with former group member Doug Aaron, current group member Dr. Zhijiang Tang, Dr. Ming Qi, Dr. Yujia Bai, Rob Atkinson and Diana Constanza. Dr. Zhijiang Tang also helped me with some experiment setup. Outside the group, Dr. Ashesh Belapure and Chinmay Dabke, who both graduated from UT and are in India now, helped me with the work in the Department of Chemistry.

Outside of research group, UTK Dance Miracle provided great friends with overflowed positive energy and great exercise and fresh air after work. UTK campus Bible study group helped me grow and improve spiritually.

Of course, I always thank my family, my parents, my brother and my grandparents. They always respect my decision and support me to realize my dream. Without their support, I would not have been here pursuing my PhD degree.

Abstract

My research focuses on catalysis of oxygen reduction reaction (ORR) by a series of Cu(II) [copper with positive two valence] -1,2,4-triazole complex-based electrocatalysts at the cathode of PEMFC (polymer electrolyte membrane fuel cell), an efficient and environmental friendly energy conversion system compared to internal combustion engines in use today. The sluggish kinetics of ORR considerably limited the performance of PEMFCs. Understanding of ORR mechanism is important for developing affordable, active and durable ORR catalysts for such devices.

The first part of my work focused on improving the ORR performance of Cu(II)-1,2,4-triazole complex-based catalysts in an acidic environment by exploring synthesis conditions including carbon support pretreatment, anions of Cu(II) compounds and reactants stoichiometry. Further mechanistic study of ORR by Cu(II)- DATZ (3,5-amino-1,2,4-triazole) complex-based catalyst provided information about the Tafel slope, and reaction orders of possible reactants involved in RDS (rate-determining step). An ORR mechanism for this catalyst was proposed based on these experimental results. Electronic properties of the Cu(II)-triazole complex-based catalysts were investigated by varying the substituents on the triazole ring. Results from calculated electron densities of N in the triazole ring and ORR performance of substituted catalysts showed that electron-donating groups are more favorable for ORR catalysis in general.

The last part addresses the problem of nature of Cu(II) complexes which are regarded as catalytic centers of ORR for synthesized electrocatalysts. Solid state EPR (electron paramagnetic resonance) spectra shows that the Cu(II) centers of the five substituted catalysts bear a tetragonal coordination feature with an elongated or compressed

coordination at axial positions. The design of an *in situ* electrochemical cell in the EPR spectrometer enables direct observation of Cu [copper] species coupling with O_2 [oxygen] species in Cu-DATZ-based electrocatalyst. This technique was applied to a synthesized Cu catalyst and its pyrolyzed sample, which demonstrates the highest ORR activity among the pyrolyzed Cu catalysts reported so far. This *in situ* study found that the Cu(II) sites decompose rapidly in the presence of electrolyte for the pyrolyzed sample while Cu(II) acts as major active sites in the non-pyrolyzed sample during ORR catalysis.

Table of Contents

1 Non-precious metal catalysts for ORR 1

1.1 Electrocatalysts for Oxygen reduction reaction (ORR) 1

1.2 Non pyrolyzed metal chelate-based catalysts 5

1.2.1 Effect of central metals on ORR activity 5
1.2.2 Effect of magnetic properties of complexes on ORR activity 10
1.2.3 Effect of redox potential of complexes on ORR activity 10
1.2.4 Effect of ligands and supported substrates on ORR 12
1.3 Pyrolyzed metal chelate-based catalysts 15

1.3.1 Central metal and ORR active sites 16
1.3.2 Carbon supports 18
1.3.3 Heat treatment conditions 19
1.4 Conclusions 21

1.5 Overview 22

2 Electrochemical characterization of ORR by copper complex-based electrocatalysts 25

2.1 Introduction 25

2.2 Experimental procedures 26

2.2.1 Chemicals 26
2.2.2 Complexation 27
2.2.3 Carbon surface diazotization (diazonium coupling) 28
2.2.4 Carbon surface oxidation 28
2.2.5 Electrode preparation from synthesized catalysts 30
2.2.6 Rotating ring-disk electrode technique (RRDE) and Cyclic Voltammetry (CV). 30
2.2.7 Inductively coupled plasma (ICP)-optical emission spectrometry (OES) 31
2.3 Dependence of ORR performance for adsorbed catalysts on different carbon supports and oxidation pretreatment 32

2.4 Dependence of ORR performance for covalently bonded catalysts obtained via carbon diazotization 35

2.5 Decomposition mechanism of immobilized catalysts based on Cu-DATZ 40

2.6 Dependence of ORR activity on different Cu/DATZ ratio in the synthesis 42

2.7 Dependence of ORR performance on catalyst/Nafion ionomer ratio 45

2.8 Dependence of ORR performance on different anions of Cu salts 48

2.9 Summary 55

3 Mechanistic study of ORR by Cu(II)-DATZ based electrocatalysts 57

3.1 Introduction 57
3.2 Experimental Procedures 61
3.2.1 Chemicals 61
3.2.2 Different Oxygen concentration experiment 61
3.2.3 Different catalyst loadings on the disk electrode 62
3.2.4 Addition of H_2O_2 in the electrolyte 62
3.2.5 Dependence of ORR on the pH of the electrolyte 62
3.3 Dependence of ORR activity on O_2 concentrations in the electrolyte 62
3.4 Dependence of ORR performance on catalyst loadings 67
3.5 Reaction order of Cu species of Cu(II)-DATZ-based catalyst in ORR 69
3.6 Addition of H_2O_2 in the electrolyte 69
3.7 Dependence of ORR performance on pH values of electrolytes 71
3.8 Proposed ORR mechanism for Cu-DATZ-based catalyst 74
4 ORR catalysis by Cu with different substituted triazole-based electrocatalysts 77
4.1 Introduction 77
4.2 Experimental procedures 78
4.3 Computational method 78
4.4 Catalysis based on Cu(II)-3-amino-5-substituent-1,2,4-triazoles complexes. 79
4.5 Dependence of ORR performance on Mulliken charges on nitrogen in triazole ring 85
4.6 Conclusions 87
5 Elemental analysis and spectroscopic studies of Cu(II) based electrocatalysts 89
5.1 Introduction 89
5.2 Experimental procedures 90
5.2.1 Attenuated total reflected FT-IR (ATR-FTIR) 90
5.2.2 Elemental analysis 90
5.2.3 EPR measurement 90
5.3 Simulation method 91
5.4 ATR-FTIR spectra of Cu based electrocatalysts 91
5.5 Elemental analysis of Cu based electrocatalysts 93
5.6 EPR spectra of Cu-substituted triazole-based electrocatalysts 99
5.7 Conclusions 105
6 Simultaneous electrochemical EPR study 107
6.1 Introduction 107

6.2 Experimental procedure 108
6.2.1 Cell Design of in situ electrochemical cell in EPR spectrometer 108
6.2.2 Electrode preparation 109
6.3 Electrochemical characterization of the *in situ* cell 111
6.3.1 Potential step experiment 111
6.3.2 Transient EPR experiment 115
7 Semi-quantitative study using *in situ* electrochemical EPR spectroscopy 118
7.1 Introduction 118
7.2 Experimental procedure 119
7.3 Cell performance comparison of *in situ* electrochemical cell and RDE cell 119
7.4 Transient EPR experiment at different O_2 concentrations 120
7.5 Potential step experiment at different O_2 concentrations 123
7.6 Conclusion 130
8 Simultaneous electrochemical EPR study of electrocatalysts before and after pyrolysis 132
8.1 Introduction 132
8.2 Experimental procedure 132
8.2.1 Catalyst synthesis and electrode preparation 132
8.2.2 EPR measurement 133
8.3 Solid state study of powder catalyst before and after pyrolysis 134
8.4 Potential step experiments with as-prepared catalysts 136
8.5 Potential step experiment of catalyst after pyrolysis 139
8.6 Conclusions 142
9 Summary 144
9.1 Carbon surface functionalities improves the ORR performance of the Cu-DATZ-based electrocatalyst. 145
9.2 Cu complexes adsorbed on carbon surface are mainly responsible for the ORR activity of Cu-1,2,4-triazole-based electrocatalysts. 146
9.3 Dinuclear Cu(I)-Cu(I) active site binds O_2 molecule. 147
9.4 Electron donating groups are favorable for ORR performance of Cu-3-amino-5-substitutents-1,2,4-triazole based catalysts 148
9.5 Catalysts as prepared and after pyrolysis studied in Goenaga *et al*‘s work demonstrate different catalytic centers for ORR. Cu(II) centers are responsible for the

catalytic sites in catalyst as prepared while Cu(II) decomposed rapidly and was not observed for this sample after pyrolysis during ORR catalysis. 148

9.6 H_2O_2 is an intermediate in ORR, rather a side product for Cu-DATZ based catalyst. 150

List of References 152

VITA 164

List of Tables

Table 2.1 Properties of different carbon supports[102] (data from reference 102)..... 32

Table 2.2 Recovered mass for samples with different Cu:DATZ ratios added after synthesis..... 44

Table 4.1 Experimental data of E^{O2}_{onset} , $E^{O2}_{1/2}$, $E^{Cu(II)}_{onset}$ and $E^{0'}$ of five Cu(II)-triazole complex-based catalysts and Mulliken atomic charges on N1, N2 and N4 in triazole ring calculated from electrostatic potential analysis by Gaussian 09 program..... 84

Table 4.2 Single point energies E of three most possible tautomers for five substituted triazoles in gas phase, The more negative of ΔE values, the lower energy of the tautomer than L1 and vice versa. 86

Table 5.1 Elemental analysis for complexes Cu(II)-3-amino-5-substituent-1,2,4-triazoles. 99

Table 5.2 Implication from g values..... 102

Table 5.3 Simulated results for EPR spectra of catalysts when the substituents are NH_2, H and $COOCH_3$. 105

Table 8.1 g factors g ⊥and g ‖ and hyperfine tentors A ⊥ and A ‖ for simulated EPR spectra in Fig. 8.1..... 136

List of Figures

Figure 1.1 Metal (Me)-ligands complexes structures[4] 3

Figure 1.2 Copper sites of Trametes hirsute laccase. The blue circles indicate copper. The blue parts in the ring indicate nitrogen.[16] (Copied from reference 16)..... 4

Figure 1.3 d electron configuration of the central metal of porphyrin chelates[26] (copied from reference 26.)..... 6

Figure 1.4 electron donation and back donation in oxygen-transition metal bonding[26] (copied from reference 26.)..... 6

Figure 1.5 Two binding modes between metal (M) and O_2 (O=O)[26] (copied from reference 26.) 7

Figure 1.6 Cu-DATZ structures proposed by Zhu (a) and Thorum *et al.* (b) (copied from reference 28 and 32)..... 8

Figure 1.7 (a) Electron configuration of $2s^2p^4$ of oxygen (b) electron configuration of d^9 of Cu(II) (c) Bonding between Cu(II) d_{z2} and the antibonding π^* orbital on the O_2, dashed line between two Cu(II) indicates that two Cu(II) centers might be weakly coupled in order to break O-O bond. It does not mean a chemical bond. 9

Figure 1.8 Electrochemical activities for the oxygen reduction by Fe-, Co-, Ni- and Cu-Pc plotted against the first electrochemical oxidation potentials of Me-Pc. η is the overpotential of ORR. (copied from reference 36.)..... 11

Figure 1.9 Structures of (a) Me-phenylenediamine, (b) Me-4-hydroxyanthraquinone, (c) Me-Pfeiffer complex, (d) Me-dihydrobenzotetraazaannulene..... 13

Figure 1.10 Structures of different substituted Pc used in Co-Pc derivatives complexes 14

Figure 1.11 Possible structures of FeN_4/C and FeN_2/C[63] (copied from reference 63) 17

Figure 1.12 ORR cathodic curves measured by RRDE of different materials: 1, as-received carbon black (Ketjen Black EC-300); 2, heat-treated carbon black; 3, heat-treated PANI-C; 4, PANI-Co-C; 5, PANI-FeCo-C(1); 6, PANI-FeCo-C(2); 7, PANI-Fe-C; 8, E-TEK Pt/C(20 μg Pt cm^{-2}). Electrolyte: O_2 saturated 0.5 M H_2SO_4. Sample 6 was obtained by twice pyrolysis with acid leaching in between.[43] (copied from reference 43)..... 20

Figure 2.1 Synthesis approaches: (a) Diazotization (b) Oxidation and (c) Complexation 29
Figure 2.2 Typical cathodic curve from RRDE experiment in O_2 saturated electrolyte at 1600 rpm. 31
Figure 2.3 a. RDE cathodic curves in O_2 saturated electrolyte of adsorbed $Cu(OAc)_2$-DATZ catalysts synthesized based on a. three carbon support BP2K, KB and Vulcan X72 oxidized by soaking them in 30% H_2O_2, 0.5M H_2SO_4 for 14 hours at RT. b. BP2K oxidized by four different conditions: 30% H_2O_2, 0.5M H_2SO_4 at 25^oC for 14 hours; APS (ammonium persulfate), 0.5M H_2SO_4 at 25^oC for 3 hours; APS, H_2SO_4 at 80^oC for 3 hours; APS, HNO_3 at 80^oC for 30min. c. Number of electrons transferred for catalysts based on four oxidized carbon..... 36
Figure 2.4 RDE cathodic curves of adsorbed and immobilized catalysts synthesized based on Cu(II)/DATZ complexes before and after 2000 cycles in O_2 saturated 0.1M H_2SO_4 electrolyte at potential 0.2-0.7V. 38
Figure 2.5 a. RDE cathodic curves in O_2 saturated electrolyte and b. CVs in N_2 saturated electrolyte of (iii) diazotization-modified BP2K reacting with extra DATZ(Blue), (ii) diazotization modified BP2K reacting with extra $Cu(OAc)_2$(red), (i) catalyst: diazotization modified BP2K reacting with both extra $Cu(OAc)_2$ and DATZ(black) in the solution. The Cu(II) loadings in the samples are shown in (a) as mmol/g and determined by ICP from synthesis. inset of b: CV in N_2 saturated electrolyte at scan rate of 1 mV/s. 41
Figure 2.6 Disk (lower panel) and ring (upper panel) currents in a CV of immobilized catalyst based on Cu-DATZ complexes in the N_2 saturated electrolyte while holding the ring electrode potential at -0.2 V vs. RHE, the rotation rate is 1600 rpm. The curve in red indicates anodic scan. The curve in black cathodic scan. 43
Figure 2.7 ORR cathodic curves, inset: number of electrons transferred, b. CVs of immobilized catalysts synthesized using Cu/DATZ ratio 2:1, 1:1, 1:2, 1:3, 1:4 and 1:5..... 46
Figure 2.8 Schematic diagram of membrane –electrode assembly (MEA)[93] (copied from reference 93) 47

Figure 2.9 Variation of Nation ionomer content in the preparation of working electrode. The catalyst amount on the disk electrode was constant for each test in O_2 saturated electrolyte while the amounts of Nafion ionomer are 20, 30, 40 and 50, wt% of the catalyst and Nafion ionomer. inset: number of electrons transferred. 49

Figure 2.10 a. RDE cathodic curves of Cu(II)-DATZ-based catalysts synthesized using copper salts $Cu(OAc)_2$, $CuSO_4$ $Cu(OTf)_2$, $Cu(ClO_4)_2$, $CuCl_2$, $Cu(NO_3)_2$ and $Cu(BF_4)_2$ and oxidized BP2K, OTf = $CF_3SO_3^-$. b. CVs for these catalysts. c. Plot of logarithm of normalized kinetic current i_k/q vs. potential 0.4, 0.3, 0.2, 0.1V..... 50

Figure 2.11 ORTEP (Oak Ridge Thermal-Ellipsoid Plot Program) of a Cu(II)-DATZ complex. H atoms have been omitted for clarity.[39] (copied from reference 39) Circles in red point out the bridge atoms between Cu centers. Circles in green indicate the co-ligand anion or molecule of the Cu centers. 53

Figure 2.12 Dimmer form of Cu(II) acetate monohydrate[116](copied from reference 116) 55

Figure 3.1 a. RDE cathodic curves of Cu(II)-DATZ-based catalyst at O_2 partial pressure 20, 40, 60, 80 and 100% in the purging gas. Inset: number of electrons transferred n. b. Zoom-in picture of kinetic region between 0.2V to 0.4 V. inset: plot of $\log J_k$ vs. $\log c_{O2}$ at potentials 0.20, 0.25, 0.30, 0.35 and 0.40 V and values of reaction order m at these potentials. c. Tafel slope plot at potential region 0.4~0.15 V at different O_2 concentrations. 64

Figure 3.2 a. CVs in N_2 saturated electrolyte. b. RDE cathodic curves in O_2 saturated electrolyte. c. number of electrons transferred at different catalyst loadings, 240, 530, 800 and 1070 $\mu g/cm^2$ on the disk electrode. The scan rate is 10 mV/s. 68

Figure 3.3 Plot of logrithm of kinetic current vs. logrithm of Cu(I) amount at potential region 0.4~0.26 V for each catalyst loading on the disk electrode. The potential inteval between points is 0.02V. Cu(I) amount is calculated by integrating the charge from the onset potential of Cu(I) to the potential where

data poinits are taken. Inset: Tafel slopes for each catalyst loading at potential region 0.4~0.2 V. 70
Figure 3.4 a. CVs of Cu-DATZ based catalyst in the presence of N_2, O_2, N_2 and H_2O_2, O_2 and H_2O_2 in the electrolyte. b. RDE cathodic curves of Cu-DATZ based catalyst in the presence of N_2 and H_2O_2, O_2 and H_2O_2, O_2 in the electrolyte. 72
Figure 3.5 ORR cathodic curves at different pH values. The inset shows a linear fit with a slope of 30mV per pH. 73
Figure 4.1 Structures of ligands used in this study. 79
Figure 4.2 a. RDE cathodic curves of Cu(II)-3-amino-5-substituent-1,2,4-triazoles complex-based catalysts. b. Number of electrons transferred. 81
Figure 4.3 CVs of five Cu(II)-3-amino-5-substituent-1,2,4-triazoles complex-based-catalysts in N_2 saturated 0.1M H_2SO_4. Redox potentials of $Cu(II)L_n/Cu(I)L_m$ in the catalysts are calculated by taking the middle points of the two dark red lines which might be an indication of oxidation and reduction peaks of redox couple. 83
Figure 4.4 Three most favorable tautomers of DATZ in aqueous solution: L1, L2 and L3. 85
Figure 5.1 ATR-FTIR spectra of unmodified BP2K (purple), pure ligand (red), diazotization modified BP2K (blues), Cu(II)-ligand complexes prepared without carbon support (greens), Cu(II)-DATZ complexes adsorbed on carbon support(catalysts, blacks) when the substituents on ligands are $–NH_2$, -H, -SCH_3,-$COOCH_3$, -SH. 94
Figure 5.2 Possible structure frame for Cu: ligand ratio 2:1 98
Figure 5.3 Magic pentagon for determining the value of n in equation 5.2.[141] (copied from reference 141) 101
Figure 5.4 Powder EPR spectra of five substituted catalysts studied in chapter 4 at X band and room temperature (solid lines). The dashed lines are simulated EPR spectra using Easy Spin 4.5.5. The vertical lines of the cross mark are the possible position of g ⊥. 104
Figure 6.1 a. Block diagram of the *in situ* electrochemical EPR apparatus. b. Detail of *in situ* flat cell. c. Electrode arrangement in cell assembly. 110

Figure 6.2 Geometry of etched gold foil. 111
Figure 6.3 EPR spectra measured without applying potential (black), while holding potential of WE 0.57V(red), 0.47V(dark red), 0.37V(cantaloupe), 0.27V(green), 0.17V(blue), 0.07V(Teal), -0.03V(orchid), -0.13V(purple) in N_2 saturated electrolyte for 440s for each potential. L represents DATZ, m and n are the ligand coordination numbers. Inset: intensities of the peaks at the field 320 mT at different potentials after baseline correction. The actual measurement was at potentials ranging from 0.62V to -0.18V with a potential interval of 0.05V. Spectra are shown at a potential interval of 0.1V for the convenience of reading. 113
Figure 6.4 EPR spectra in the presence of N_2 and O_2 at potentials 0.7 V, 0.3 V, 0.2 V. 114
Figure 6.5 a. EPR intensities at constant field 320mT, b. CV at 10mV/s in N_2 saturated 0.1M H_2SO_4 electrolyte. c. EPR intensity at constant field 320mT, d. CV at 10mV/s in O_2 saturated 0.1M H_2SO_4 electrolyte. Scans in red are cathodic scans and in black are anodic scans. 116
Figure 7.1 a. CVs of *in situ* electrochemical cell in N_2 (in red) and O_2 (in black) saturated 0.1 M H_2SO_4 with a flow rate 0.0325 ml/s at scan rate 50 mV/s. b. CVs of catalyst deposited on glassy carbon rotating disk electrode in N_2 (in red) and O_2 (in black) saturated 0.1 M H_2SO_4 with rotation rate 1600 rmp and scan rate 10 mV/s. The blue dashed lines point out the approximate position of the onset potential of ORR. 121
Figure 7.2 a. Transient EPR spectra at constant magnetic field 321 mT and b. CVs from the *in situ* electrochemical cell at different O_2 concentration saturated electrolytes. Solid lines are spectra collected during the cathodic scans of CVs and dotted lines are spectra CVs collected during the anodic scan of CVs. The scan rate is 10mV/s. 122
Figure 7.3 EPR spectra collected at different potentials for each O_2 concentration a) 0%, b) 20%, c) 60%, d) 80%, e) 100% in the 0.1 M H_2SO_4. Each potential step is 400 s. 124
Figure 7.4 Peak heights of EPR signal at different potentials for each O_2 concentration. The corresponding magnetic fields where the peak of Cu(II) EPR signal

occurs shift to high field slightly as potential decreases. At 0.724V, the peak height was taken at the magnetic field 321mT. At 0.524V and 0.424V, the peak heights are measured at 322 mT. At the rest of the lower potentials, the peak heights are measured at 323 mT. 125

Figure 7.5 Typical current response at each potential for different oxygen concentrations in the electrolyte. the values at potential 0.224 V is shown as an example. . 126

Figure 7.6 Potential vs. current density measured from *in situ* electrochemical cell at different O_2 concentration in the electrolytes. In *in situ* electrochemical cell measurement, the potential is the applied potential step; the current is the constant current reached after first few seconds of the applied potential step. Inset: potential vs. logarithm of current density measured from *in situ* electrochemical cell. Legends show the calculated Tafel slopes in mV/decade and the relative coefficients of the dashed fitting lines..... 128

Figure 7.7 Logarithm of current density vs. logarithm of O_2 concentration at kinetic dominant potential region in the *in situ* electrochemical cell. The legend shows the reaction order of m calculated and the relative coefficient of the dashed fitting lines at different potentials. 129

Figure 7.8 Logarithm of current density vs. logarithm of Cu(I) EPR intensity from measurement in *in situ* electrochemical cell at different O_2 concentrations in the electrolytes. The intensity values here are normalized by the intensity at 0.724 V for each O_2 concentration. The legend shows the values of Cu(I) reaction order q and the relative coefficient of the dashed fitting lines. 131

Figure 8.1 Synthesis for non pyrolyzed catalyst[129] (copied from reference 129)..... 133

Figure 8.2 Solid state and *in situ* measurement of catalysts before and after pyrolysis at 950 ^{o}C at room temperature. The dashed lines are fitted curves using Matlab R2012b with toolbox Easyspin 4.5.5. For the spectrum in green, the baseline was corrected using first order polynomial, as shown in spectrum in purple with solid..... 135

Figure 8.3 EPR spectra at different potentials for each O_2 concentration in the electrolyte 137

Figure 8.4 Peak intensity of Cu(II) EPR signal at different potentials. The magnetic field for taking the values of peak intensities are: 321 mT for potential 0.7 to 0.45 V, 322 mT for potential 0.4 to 0.2 V and 323.5 mT for potential 0.1 to -0.1 V. 139

Figure 8.5 EPR spectra of catalyst after pyrolysis at 950 ^{o}C at different potentials for each O_2 concentration in the electrolyte..... 141

Figure 8.6 CVs of the pyrolyzed catalyst at different O_2 concentrations in the *in situ* electrochemical cell. 142

List of Schemes

Scheme 3.1 Reaction scheme for electrochemical oxygen reduction. (copied from reference 49) 60

Scheme 6.1 Proposed first step mechanism for Cu(II) and Cu(I) conversion in the presence of N_2 and O_2. 117

1 Non-precious metal catalysts for ORR

1.1 Electrocatalysts for Oxygen reduction reaction (ORR)

The oxygen reduction reaction is a ubiquitous process extracting energy from carbohydrate compounds in biological systems. Oxygen is also the most common oxidant on earth in terms of its composition of 20.95% in atmosphere. Its abundance contributes substantially to the existence of life on earth and also indicates the fact that oxygen molecules must be moderately inert to maintain a stable environment on earth. Therefore, catalysts are required to lower the activation energy of ORR in order to obtain higher energy output from ORR.

The application of the ORR in a fuel cell, a device converting hydrogen and oxygen into water, motivates the effort of seeking ORR catalysts to gain more energy from the system by increasing the reaction efficiency. PEMFCs are different from conventional combustion engines whose energy-converting efficiencies are limited by the Carnot principle. PEMFCs have the potential of extracting most of the energy in a fuel.[1] Thermodynamically, the reaction of hydrogen and oxygen to form water can deliver 1.23V potential. In practice, PEM fuel cells, which operate at relatively low temperature, can only provide about 40-60% of the thermodynamic value at practical current densities. The major potential drop is caused by slow kinetics of the ORR at the cathode of PEMFCs. This potential is called overpotential and used to drive the reaction. The lower the overpotential, the faster the reaction. The overall four-electron reduction of molecular oxygen in an acidic environment is:

$$O_2 + 4H^+ + 4e \leftrightharpoons 2H_2O \quad E_0 = 1.229V \qquad (1.1)$$

One important side reaction of ORR is the production of hydrogen peroxide:

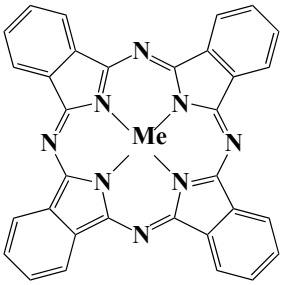
$$O_2 + 2H^+ + 2e \leftrightharpoons H_2O_2 \quad E_0 = 0.695V \qquad (1.2)$$

$$O_2 + H^+ + e^- \rightarrow intermediate \qquad (1.3)$$

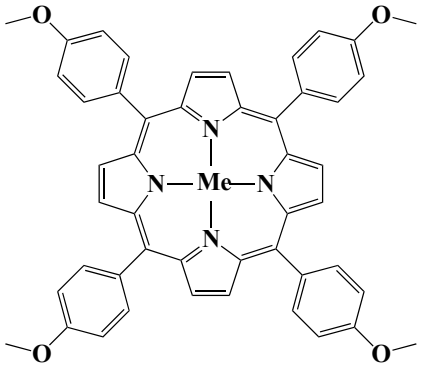
The formation of hydrogen peroxide not only decreases the energy released from reaction (1.1) but also is thought to be harmful to the structure of polymer electrolyte membranes in PEMFCs.

In terms of both activity and stability for PEMFC application, the most practical ORR catalysts so far are platinum based catalysts. The ORR mechanism catalyzed by platinum-based catalysts in acid has been studied extensively. An accepted mechanism of the rate determining step catalyzed by this class of catalysts involves O_2 adsorption with simultaneous charge and proton transfer on platinum surface, which is indicated by reaction (1.3).[2,3] However, the scarcity and high cost of platinum make the commercialization of fuel cells prohibitive. Enormous effort has been devoted to seeking non-precious metal-based catalysts to replace platinum during the past half century.

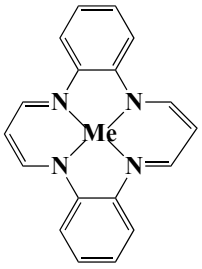
In 1964, Jasinski first discovered the ORR catalytic activity of transition metal phthalocyanine (Me-Pc) (Fig.1.1a) supported on carbon in alkaline conditions.[4] Later, the catalytic activity of various metal-N_4 complexes (Fig. 1.1) supported on carbon was demonstrated in acidic media.[5–8] A significant breakthrough was achieved by the introduction of heat treatment to the catalyst synthesis process.[9–11] This approach increases both the ORR activity and stability of the catalysts. However one of the drawbacks of these pyrolyzed Me-N_4 complex-based catalysts is that it is difficult to identify the formation and nature of active sites produced at high temperature. Furthermore, multiple pyrolysis (900-1000 ℃) and acid treatment steps may not save the cost of catalyst preparation by large-scale production.



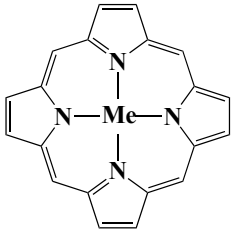
(a) Metal phthalocyanine complex(Me-Pc)



(b) Me-tetra-(p-methoxyphenyl)porphyrin



(c) Me-dibenzotetraazaannulene



(d) Me-porphyrin

Figure 1.1 Metal (Me)-ligands complexes structures[4]

Another category of reported catalysts with high ORR activity are the copper-containing enzymes such as laccase, which catalyze the ORR with almost no overpotential (20 mV).[12] The remarkable activity exhibited by these enzymes offers us an opportunity to develop electrocatalysts with higher activities than platinum from the perspective of biomimetic studies. Multiple research groups have tried to attach the enzymatic structure on an electrode to obtain high performance ORR catalysts.[12–16] Unfortunately, laccase can function only at a narrow pH range and cannot tolerate the acidic environments in PEMFCs. The large molecular size of the enzyme limits the current density as well as the mass transport.[14,17] Extensive efforts have been devoted in studying the mechanism of these multicopper oxidases including laccase, ascorbate

oxidase, ceruloplasmin and Fet3.[18–20] Metal chelates are believed to be an important part of active centers in transferring electrons for ORR in these enzymes.[21,22] Laccase is identified as the simplest of the multicopper oxidases with four copper atoms encompassed by imidazole and sidechains of histidine in this active site.[16,23,24] The copper centers of laccase are illustrated in Fig. 1.2. This fact inspired the development of synthesized copper chelate complexes based electrocatalysts, which is employed in my research.

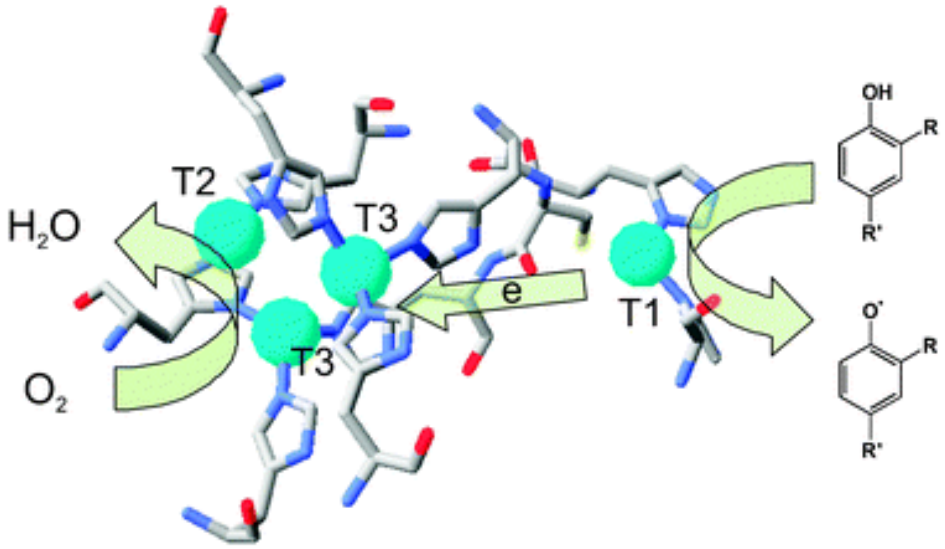


Figure 1.2 Copper sites of Trametes hirsute laccase. The blue circles indicate copper. The blue parts in the ring indicate nitrogen.[16] (Copied from reference 16)

Although non-pyrolyzed metal chelates supported on carbon are less active as cathode catalysts for PEMFCs, they bear the merits of facile synthesis and well-preserved structures. The scope of this literature review focuses on the description of pyrolyzed and non-pyrolyzed metal chelate-based ORR catalysts. The effects of central metals, redox potentials and magnetic properties of complexes and ligands are discussed for non-pyrolyzed metal chelate-based catalysts. The catalytic centers for pyrolyzed metal

chelate-based ORR catalysts are still a subject of extensive debate. Synthesis conditions are determined by trial and error including carbon supports/precursors, metal selection and loading in the catalyst, and heat treatment temperature and time. However, some consensus on catalytic centers has been reached after numerous experiments. The catalytic centers of enzymatic materials will be briefly covered to provide fundamental understanding of ORR catalysis.

1.2 Non pyrolyzed metal chelate-based catalysts

1.2.1 Effect of central metals on ORR activity

As mentioned above, pyrolyzed non-precious metal catalysts have achieved great success as alternatives to platinum-based catalysts. However, the nature of the catalytic centers remains unclear because of thermal treatment during synthesis procedures. Non-pyrolyzed non-precious metal ORR catalysts have been effectively utilized to examine the correlation between the ORR activities and the properties of central metals and coordinated ligands. However, there is still a debate about the involvement of metals in the catalytic centers among pyrolyzed catalysts. Experimental findings showed that the ORR activity decreases in the order of Fe(II) > Co(II) > Ni(II) > Cu(II) using Me-Pc based catalysts in acidic media. The activities decrease in the order of Co(II) > Fe(III) > Ni(II) ~ Cu(II) when the ligands are tetra-(p-methoxyphenyl)porphyrin and dibenzotetraazaannulene.[4,8,25] The structures of metal-ligand complexes are depicted in Fig. 1.1 based on above ligands. Alt *et al.* explained the differences using MO theory based on the energy level of the d-orbitals of the transition metal in porphyrin complexes calculated by Zener and Gouterman, as shown in Fig. 1.3.[26,27]

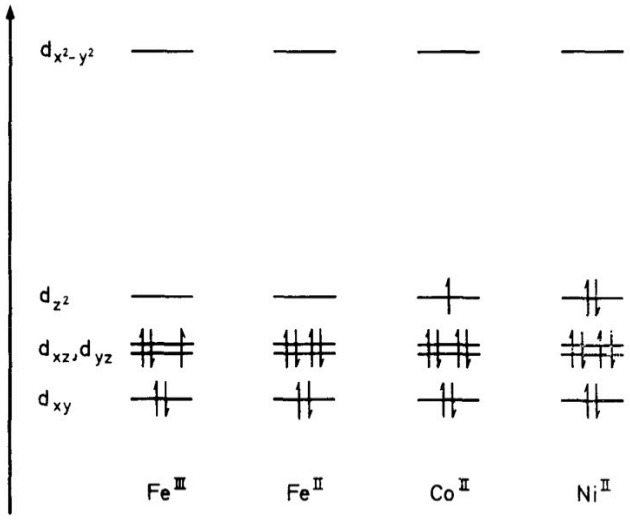


Figure 1.3 d electron configuration of the central metal of porphyrin chelates[26] (copied from reference 26.)

From the perspective of orbital symmetry, they believed there are two possible binding patterns between oxygen and central metals (Fig. 1.4): electron donation bonding of vacant d_{z2} orbitals of central metals with π electrons in oxygen and back bonding interaction of filled metal orbitals d_{xz} or d_{yz} with antibonding orbital π^* in oxygen.

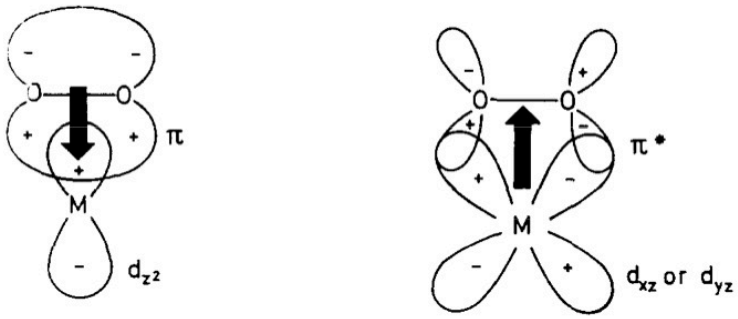


Figure 1.4 electron donation and back donation in oxygen-transition metal bonding[26] (copied from reference 26.)

The latter is preferred with consideration of filled d_{xz} and d_{yz} orbitals in central metals.[26] d_{xz} and d_{yz} orbitals in the metal have similar electron configurations to that of antibonding

orbital π^* in oxygen, which the d_{z2} orbital in metal and π electrons in oxygen do not. This also favors the back bonding mode.

Recently, Zhu calculated the oxygen binding energies of a series of metal porphyrins and DATZ compounds using the DFT method.[28] This work proposed that the bonding between the empty d_{z2} of the metal and the antibonding π^* are preferred considering the energy gaps of all the possible binding orbitals. Shi and Zhang also conducted DFT calculations on the dioxygen binding abilities of both cobalt and iron complexes with both porphyrin and phthalocyanine.[29] Both of these works agree with Alt's suggestion that metals act as electron donors while oxygen is an acceptor in the process of oxygen binding. Shi and Zhang concluded that a partial electron is transferred from central metal to the dioxygen antibonding π^* orbitals, leading to elongated O-O bond length in complex Fe(II)-O_2.

One point worth mentioning is the binding modes between metal and oxygen. In all above work both calculation and experimental evidence suggests edge-on (Fig. 1.5) binding mode, where the O interacting with metal center tilts away from the metal and ligand coordination plane, is preferred.[25,26,30,31]

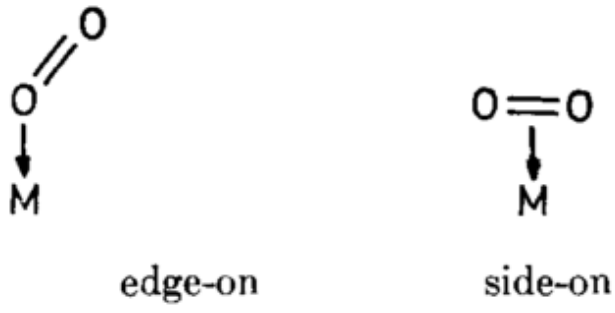


Figure 1.5 Two binding modes between metal (M) and O_2 (O=O)[26] (copied from reference 26.)

The appearance of a 5th ligand at the axial position of square planar complex could affect the energy level of d_{z2} in metal and further change the electron bonding at this orbital. The surface groups of the carbon act as a strong 5th ligand in Me-Pc/Porphyrin complexes. Some experimental findings show that certain types of carbon substrate considerably enhance the activity of FePc. This could be due to these surface groups exerting a particularly favorable effect on raising the energy level of the d_{z2} orbital.[8]

Besides comparing the energy level of possible bonding orbitals, which requires the knowledge of coordination geometry of metal chelates, O_2 binding energy has been considered as another important factor affecting ORR activities of different metal chelates. Zhu calculated that Cu(II)-DATZ complex has no binding energy toward O_2 but recent findings by Thorum *et al.* contradict this assertion.[28,32] The proposed structures of Cu-DATZ complexes by Zhu and Thorum *et al.* are shown in Fig. 1.6a and b respectively.[28,32] The Cu(II)-DATZ complexes supported on carbon were found to exhibit a 0.73V onset potential at pH 7.[32]

(a) (b)

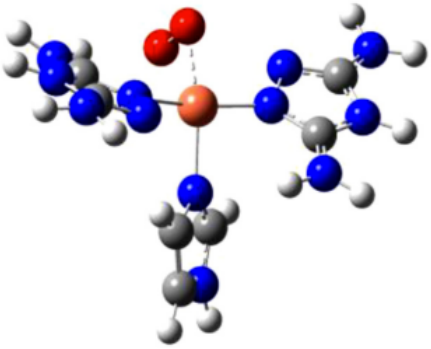




Figure 1.6 Cu-DATZ structures proposed by Zhu (a) and Thorum *et al.* (b) (copied from reference 28 and 32)

In our work, an onset potential of 0.5V was observed for a Cu(II)-DATZ complex-based catalyst in 0.1M H_2SO_4. Cu(II) has 9 electrons in the *d* orbital and the one unpaired electron occupies either a d_{x2-y2} or d_{z2} orbital. All other d orbitals are filled from the point of view of MO theory. Zhu proposed that the bonding between HOMO of Cu(II) and LUMO of oxygen is primarily between the metal d_{z2} (Fig. 1.7b) and the antibonding π*(Fig. 1.7a) orbital on the O_2 . Their electron configurations are shown in Fig. 1.7c.[28] If this is the case, two Cu(II) centers are needed to break one O-O bond and form Cu(III), assuming that two electrons are transferred in this step. Since Cu(III) is highly oxidized and not stable, the two initial Cu centers are suggested to be Cu(I). Additionally, Cu(I) is easily oxidized into Cu(II) and O_2 is an oxidant.

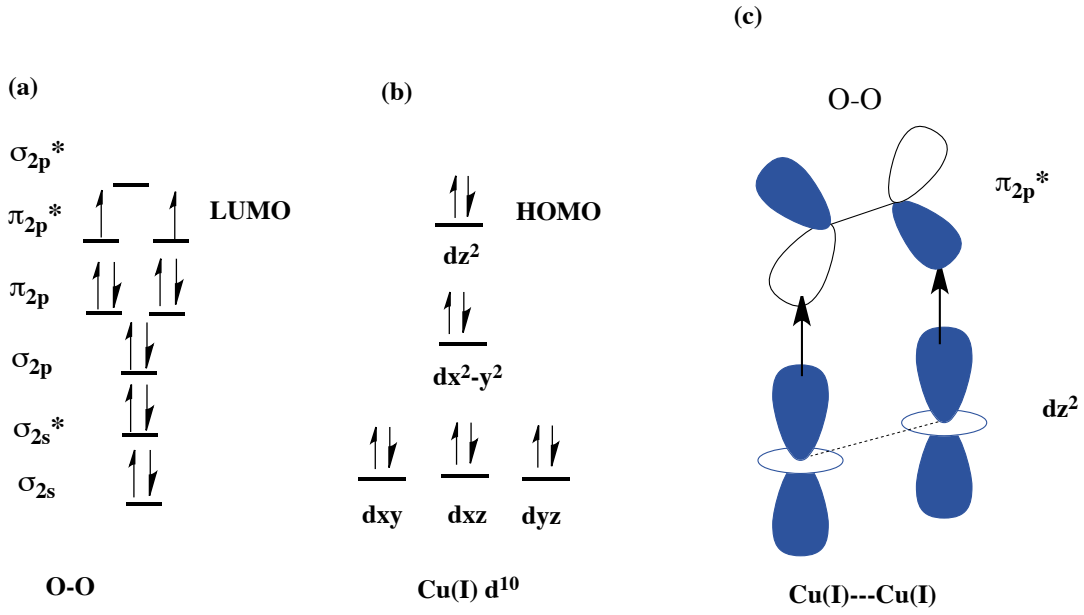


Figure 1.7 (a) Electron configuration of $2s^2p^4$ of oxygen (b) electron configuration of d^9 of Cu(II) (c) Bonding between Cu(II) d_{z2} and the antibonding π* orbital on the O_2, dashed line between two Cu(II) indicates that two Cu(II) centers might be weakly coupled in order to break O-O bond. It does not mean a chemical bond.

1.2.2 Effect of magnetic properties of complexes on ORR activity

Besides MO considerations, another possible explanation for describing ORR activity is the magnetic properties of central metals. Triplet oxygen is the ground state of an oxygen molecule and has an intrinsic magnetic moment due to spins of unpaired electrons (total spin S=1), which prevents direct reaction of O_2 with many molecules with typical singlet ground state.[1] Zhu pointed out that metals with spin states S=1 and S=1/2 tend to overcome the spin prohibition more readily and react with O_2 with less difference in spin states from O_2 molecule.[28] Higher ORR electrocatalytic activities of phthalocyanines were observed with increasing magnetic moment by Randin.[33] Based on the complicated behavior of magnetic susceptibility with temperature, Thorum *et al.* claimed that triplet state Cu(II) centers were populated in their Cu-DATZ-based ORR catalysts.[32] More work should be devoted to relating the magnetic properties of transition metal chelate-based electrocatalysts to ORR activity before a consensus can be reached.

1.2.3 Effect of redox potential of complexes on ORR activity

Based on the mechanism that O_2 obtains the first electron from the metal center, Randin has suggested that redox potentials of central metals are important, as seen from most proposed mechanisms for ORR catalyzed by metal chelates.[34,35] This mechanism describes the first oxidation potential based on the ease of extracting an electron, electrochemically from the metal chelate electrodes.[33] Beck described the electroreduction of oxygen catalyzed by metal chelates of the N_4 type as a modified 'redox catalysis' in which the rate determining step is determined by potential.[6] Savy *et al.* measured electrochemical oxidation potentials of a series of different metal chelates and their corresponding ORR activities.[36] They observed that the higher the oxidation

potentials of the metals, the higher overpotentials of ORR and the worse the performance, as shown in Fig.1.8. Shi and Zhang investigated the ionization potentials of a series of Co(II)/Fe(II)-porphyrin/ phthalocyanine complexes and correlated them with dioxygen binding abilities. In their study, for porphyrin systems, the Co(II) compound shows better performance than its Fe(II) counterpart.[29] For phthalocyanine the opposite trend is observed. They observed that higher ionization potentials of the central metal and larger dioxygen binding energies are associated with better catalytic activities. Shi and Zhang also correlated the ORR catalytic activities with Mulliken charges on the central metals but no conclusion was made.[29] McCrory *et al.* observed higher redox potentials and lower ORR performance in different, substituted Cu-1,10-phenanthroline complexes.[35] Electronic properties of ionization potential, the first electrochemical oxidation potential and the redox potential of central metals can be affected greatly by the surroundings, i.e. coordinated ligands and support substrates. In the next section, the ligand effect on ORR electrocatalytic activites will be reviewed.

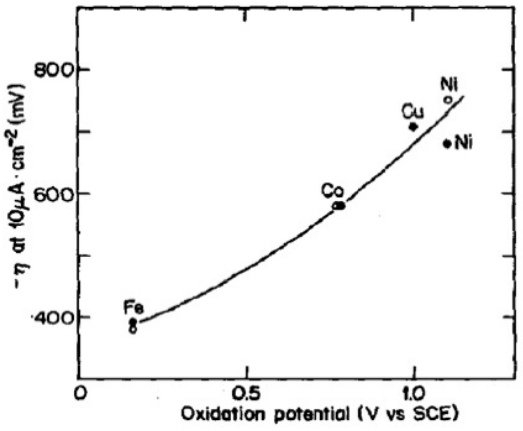


Figure 1.8 Electrochemical activities for the oxygen reduction by Fe-, Co-, Ni- and Cu-Pc plotted against the first electrochemical oxidation potentials of Me-Pc. η is the overpotential of ORR. (copied from reference 36.)

1.2.4 Effect of ligands and supported substrates on ORR

Porphyrin derivatives are widely used ligands since they are found as part of cytochromes and serve as oxygen activators in redox systems at medium pH values.[12,14,21] Different porphyrin derivatives have been used as active and stable precursors for catalyzing the ORR. Me-Phenanthroline (Me-Pc) as ORR electrocatalyst has attracted the most attention since Jasinski's discovery of ORR activity of Co(II)-phthlocyanine in 1964. Porphyrin and phthalocyanine have in common square planar arrangement of the four nitrogens and large π conjugated system emcompassing the nitrogens. Later ligands of similar structures have been tried including anthraquinone, dihydrodibenzotetraazaannulene, phenylenediamine derivatives and Pfeiffer complexes. The corresponding complex structures are depicted in Fig. 1.9. Me-N_4 proved to be much more stable and active compared to other complexes with non-nitrogen donors included in the ring, namely N_2O_2, N_2S_2, O_4 and S_4 from electrochemical test of a series of Fe complexes in $KHCO_3$ and K_2CO_3 solution. [25]

Substitutions on the ligands could change the electronic properties of the ligand and hence the electronic properties of complexes. Alt *et al.* studied the p-position substituents on the phenyl ring in Co(II) tetraarylporphyrin complexes.[26] They concluded that electron donating groups raise the activity in the following order: methoxyl > benzyl > methylmercapto > no substituent. Methylmercapto was believed to be oxidized to methylsulfinyl or methylsulfonyl, which have electron withdrawing properties.[26] Zagal *et al.* drew an opposite conclusion from the study of different substituted phthalocyanines with cobalt(II) based on their experimental and theoretical study.[37] The five substituted complexes investigated are Co(II) phthalocyanine(CoPc), Co(II)

tetraneopentoxyphthalocyanine (CoTNPPc), Co(II) octamethoxyphthalocyanine (CoMeOPc), Co(II) tetrasulfophthalocyanine (CoTSPc) and Co(II) hexadecafluorophthalocyanine ($CoF_{16}Pc$). The corresponding ligands are depicted in Fig. 1.10.

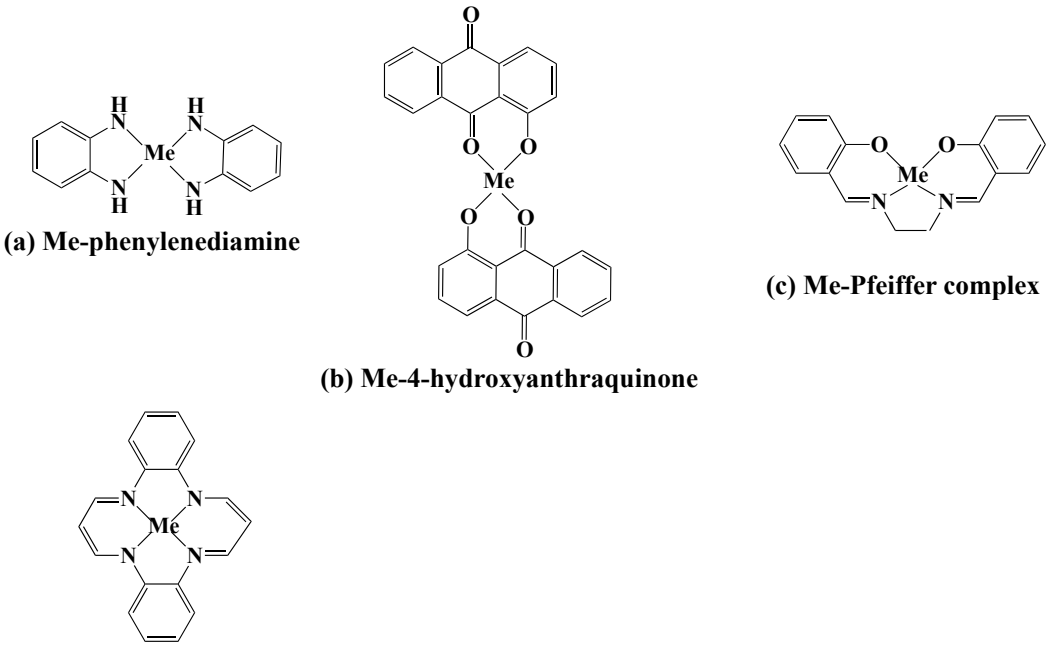
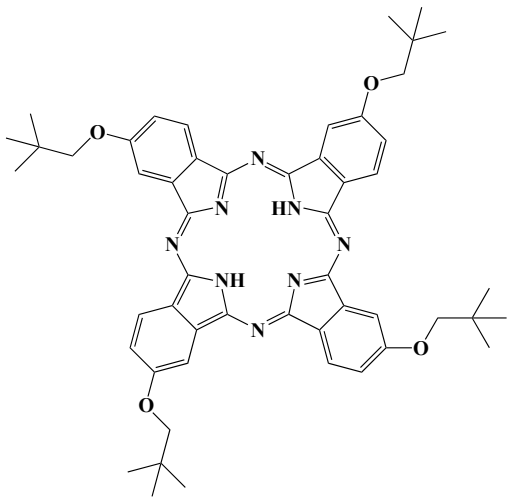


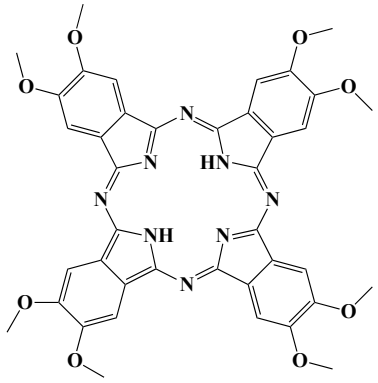
Figure 1.9 Structures of (a) Me-phenylenediamine, (b) Me-4-hydroxyanthraquinone, (c) Me-Pfeiffer complex, (d) Me-dihydrobenzotetraazaannulene

In their work, parameters including ORR activity, redox potential, energy gap of HOMO-LUMO and the molecule hardness were examined. They concluded that the ORR activity decreases as the electron donating capacity of substituted functional groups increases. They also related the ORR activities to the redox potentials of metal complexes and proposed a comprehensive concept of molecular hardness for evaluating the energy gap

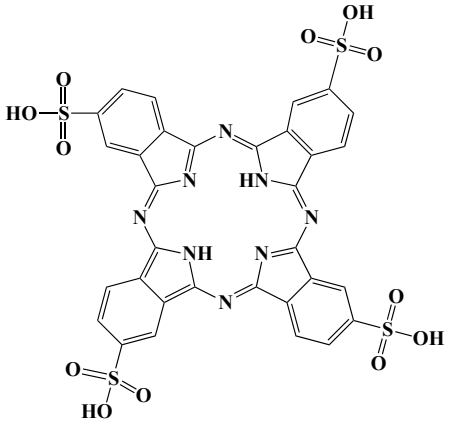
between HOMO of metal complexes and LUMO of dioxygen molecule. Larger gaps correspond to larger hardness.



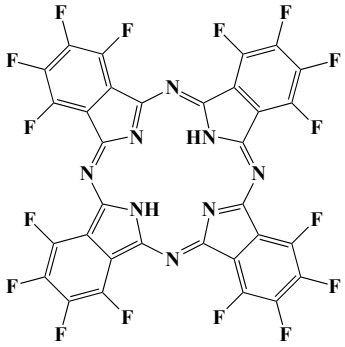
(a) tetraneopentoxyphthalocyanine(TNPPc)



(b) octmethoxyphthalocyanine (MeOPc)



(c) tetrasulfophthalocyanine (TSPc)



(d) hexadecafluorophthalocyanine (F_{16}Pc)

Figure 1.10 Structures of different substituted Pc used in Co-Pc derivatives complexes

The increasing intermolecular hardness in the system of Co-Pc/O_2 results in decreasing ORR activity of the system. McCrory *et al.* investigated a series of substituted Cu(II) phenanthrolines and concluded that electron withdrawing groups/steric demands near Cu centers increase redox potentials of the catalysts but decrease the rate of ORR without

mentioning about the effect of electron donating groups.[35] They concluded that further increase in the ORR activities of monocular Cu-phenanthroline complexes is unlikely and proposed future studies on multinuclear catalytic centers.

Inspired by the cross linked Cu-imidazole structure in Cytochrome c oxidase, a Cu(II)-3,5-diamino-1,2,4-triazoles(Cu-DATZ) complex-based ORR electrocatalyst with onset potentials 0.86V and 0.73V at pH 13 and pH 7 respectively was prepared, by Thorum *et al*.[32] Compared to porphyrin and phthalocyanine derivatives, 1,2,4-triazole and its derivatives bear the merits of smaller size and π-conjugated system, indicating it is more tunable by different substituents. Aznar *et al.* synthesized two types of Cu(II)-DATZ complexes. Both of them are multinuclear complexes. A central Cu(II) has octahedral coordination geometry, resulting in different energy levels of the d orbitals.[39] This differs from the Cu(II)-porphyrin/phenanthroline complexes with a square planar geometry exhibiting low catalytic activity toward ORR. On the other hand, Cu(II)-DATZ complexes have demonstrated great diversity from the point of view synthesis procedure.[40–42] This could offer more choices of complexes with multinuclear catalytic centers as well as complicated complex systems.

1.3 Pyrolyzed metal chelate-based catalysts

A significant breakthrough in the ORR activity as well as durability of metal chelate-based catalysts was achieved by introducing the process of thermal treatment.[9–11] Compared to other alternatives of replacing Pt-based catalysts, these pyrolyzed metal chelate-based electrocatalysts are the most promising candidates due to their decent ORR performance though they are still inferior to Pt-based catalysts. Other pyrolyzed alternatives explored include conductive polymer-based complexes,[43–45] transition metal

chalcogenides,[46–48] metal oxides/carbides/nitrides[49–53] and enzyme-based materials[12,15,17,54]. This section will focus on the pyrolyzed metal chelate-based electrocatalysts due to their advantages in ORR performance. Research of this class of catalysts has been reviewed extensively in previous reports.[55–59] From the synthesis procedure, the major factors affecting the ORR performance including the center metal types, carbon supports, acid leaching and the conditions of heat treatment, as discussed below.

1.3.1 Central metal and ORR active sites

Multiple transition metals have been explored to obtain optimal ORR performance for pyrolyzed metal chelate-based catalysts, including Mn, Fe, Co, Ni, Cu, Zn. The most promising metals are Fe and Co.[60] The metal-N_4 center bound to the carbon support is believed to act as the active site for these catalysts.[61–66] However, some work has claimed that the presence of metal in the precursor during heat treatment primarily served to catalyze the formation of the active sites, which might be the stable incorporation of N into the graphitic carbon.[67,68] Dodelet *et al.* detected the two different catalytic sites FeN_4/C and FeN_2/C using Time-of-Flight Secondary Ion Mass Spectrometry (ToF-SIMS). FeN_4/C stands for an Fe ion coordinated to 4 nitrogen atoms of the pyrrole type while FeN2 are Fe ions coordinated to two nitrogen atoms of the pyridinic type.[69] The structures are shown in Fig. 1.11.

Scherson *et al*. investigated a number of cobalt and iron porphyrins after heat treatment temperatures as low as 400 ^{o}C using themogravimetric analysis and found that the fraction of volatile nitrogen remaining in the catalysts was much lower for pyrolyzed iron and cobalt porphyrins than for pyrolyzed metal-free macrocyclic compounds.

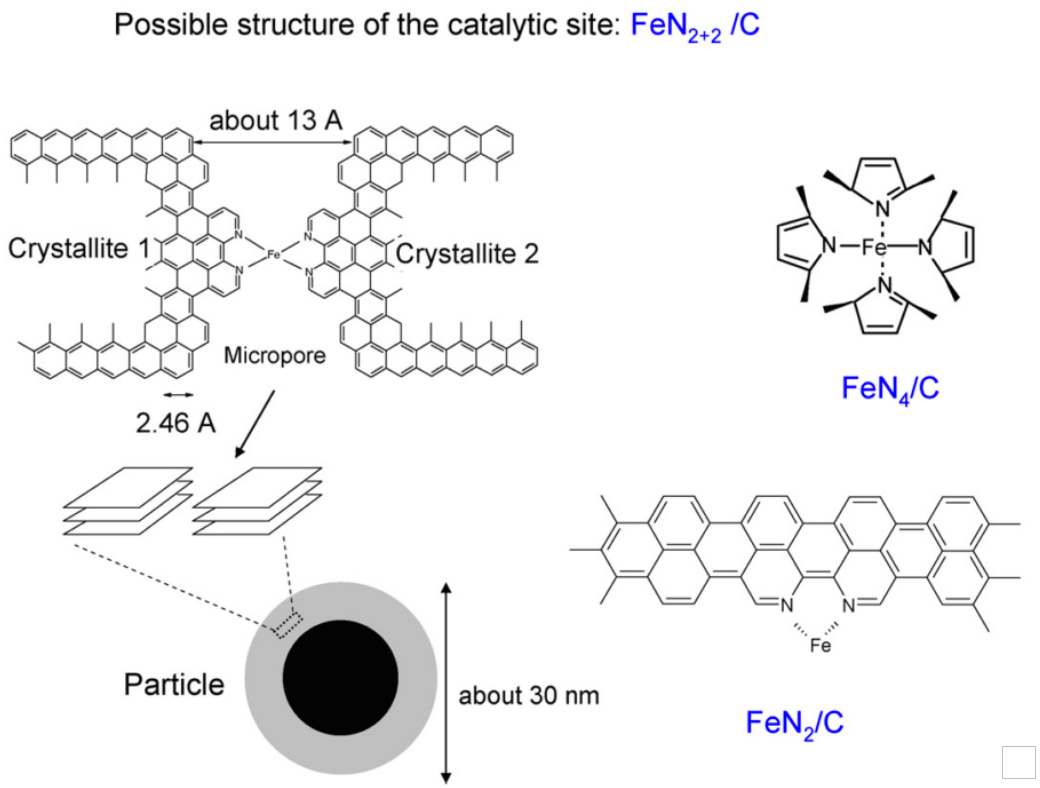


Figure 1.11 Possible structures of FeN_4/C and FeN_2/C[63] (copied from reference 63)

They also observed the decomposition of metal free macrocyclic compounds started at around 400-500 ^oC.[60] The differing and controversial conclusions from different research groups are possibly caused by the different synthesis procedures employed.

Introduction of binary metals in the pyrolyzed catalysts is an active research direction. The heat treated Fe/Co macrocycles showed significantly higher ORR activity than other combinations.[60] The structures of these binary metal catalysts might have the advantages of both catalysts, such as the high ORR activity of Fe and the prominent stability of Co based electrocatalysts.[10,70] Another finding showed that an increase in electron density on the iron centers enables an improvement in the turnover frequency during ORR using X-ray induced photoelectron spectroscopy and Mossbauer spectroscopy by studying the pyrolyzed Fe-based ORR electrocatalysts.[71]

1.3.2 Carbon supports

The surface nitrogen content and porosity of carbon support have a significant impact on the ORR activity of pyrolzyed metal chelate-based electrocatalysts. Nitrogen is introduced from N-containing macrocycle complexes (pyrrole, phenanthroline for example) and the use of an ammonia atmosphere during pyrolysis. Multiple research groups have reported that increasing N content from zero to a certain level was associated with higher ORR performance for pyrolyzed Fe/Co based-catalysts. ORR activity of the catalysts would not vary significantly after a threshold N content is reached to meet the need for the formation of active sites.[72–74] As mentioned above regarding the suggested active sites, nitrogen is an important part in the FeN_x/C active sites. The introduction of NH_3 during pyrolysis not only adds N-bearing functionalities on the surface of carbon, but also contributes to the formation of micropores through chemical etching, which are indicated by the following reaction mechanism:[75]

$$C + NH_3 \rightarrow HCN + H_2 \quad (1.4)$$

$$C + 2H_2 \rightarrow CH_4 \quad (1.5)$$

Another process involved in the formation of micropores is the gasification of the disordered phase present in carbon supports. Microporosity (pore width 7-22 Å) was regarded as a major host for active sites and maximization of the surface area of micropores is an important factor in increasing the ORR catalytic activity.[76] A joint work reported by multiple laboratories stated that active sites seems to be mainly hosted in pore size 5-15 Å from investigation of nine non-noble-metal-metal catalysts.[72]

Besides N functionalities and microporosity of the carbon support, the introduction of oxygen functional group was shown to improve the ORR activity and selectivity towards

4e- reduction for pyrolyzed Fe based-catalysts.[73,77,78] This was explained that oxygen can act as a co-ligand to bind Fe-Pc complex particles and increase the polarity of the carbon support to improve the dispersion of particles on carbon supports.[79] Gouercec *et al*. concluded that the presence of oxygen groups increases the sintering resistance of Co complex particles by comparing pyrolyzed Co complexes on two carbon supports with varying concentration of O groups on the surface.[80] Oxygen groups play a role in forming active sites for oxygen reduction. However, reports proposing that oxygen is part of the active site are not found in the literature.

1.3.3 Heat treatment conditions

Heat treatment (500-1000 ^{o}C) was first introduced by Jahnke *et al.* in 1974. This leads to a significant activation of the ORR activity as well as improved stability of Co-based electrocatalysts in an acidic environment.[25] This discovery opened a new direction of synthesizing promising ORR electrocatalysts to replace Pt-based ORR catalysts. However, the active sites formed at elevated temperature are not completely understood. Generally it is believed that active sites are related to the coordination between the central metal and nitrogen atoms on the carbon support for metal chelate-based electrocatalysts. The optimal conditions for heat treatment process are determined by trial and error and vary from lab to lab. Dodelet *et al.* have done systematic work on Fe based catalysts to understand the evolution of catalysts during pyrolysis by varying the time and temperatures of heat treatment. They found that there are three stages in forming the ORR active sites: 1) incorporation of nitrogen atoms in carbon; 2) micropore formation through reaction between carbon and ammonia; 3) completion of active sites in micropores by reaction of iron and ammonia. Step 2) is the slowest step. The density of

active sites is maximized when Fe and NH_3 are present, leading to maximized surface area of micropores.[76] Later, secondary pyrolysis was found to further improve the ORR performance of pyrolyzed Fe and Co based-catalysts after acid leaching. Nabae *et al*. obtained high initial cell performance and good durability compared to other precious-metal-free cathode catalysts to date via multi-step pyrolysis of Fe-based catalysts.[81] Wu *et al.* achieved exemplary activity of Fe/Co based electrocatalysts using two pyrolysis steps with acid leaching in between for synthesis. The performance of catalysts thus prepared is shown in Fig. 1.12.[43] The possible explanation for the performance improvement was related to removing contaminants and impurities by acid leaching and secondary pyrolysis, especially metallic species produced during the first pyrolysis, which was regarded as blocking the active sites and favoring 2e- O_2 reduction.[82,83]

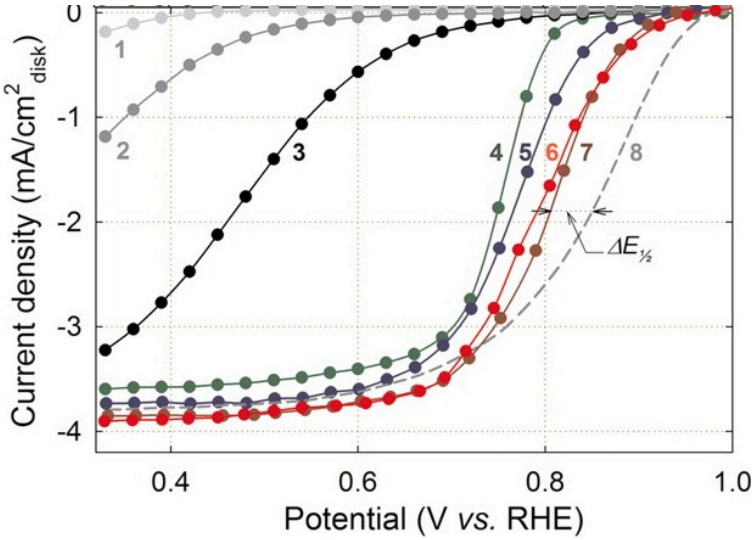


Figure 1.12 ORR cathodic curves measured by RRDE of different materials: 1, as-received carbon black (Ketjen Black EC-300); 2, heat-treated carbon black; 3, heat-treated PANI-C; 4, PANI-Co-C; 5, PANI-FeCo-C(1); 6, PANI-FeCo-C(2); 7, PANI-Fe-C; 8, E-TEK Pt/C(20 μg Pt cm^{-2}). Electrolyte: O_2 saturated 0.5 M H_2SO_4. Sample 6 was obtained by twice pyrolysis with acid leaching in between.[43] (copied from reference 43)

In summary, pyrolyzed metal chelate-based electrocatalysts are promising alternatives to replace Pt based electrocatalysts to possibly realize the commercialization of PEMFCs due to their relatively high ORR activity achieved recently. However, the durability is still insufficient compared to Pt based catalysts.[84] Additionally, the ORR mechanism catalyzed by these catalysts is not completely understood and the nature of the active sites is still a subject of extensive debate. These hinder effective further improvement of the performance of these catalysts. Future work should focus on deciphering the nature of the ORR catalytic active sites of these catalysts to improve the ORR performance accordingly.

1.4 Conclusions

Pyrolyzed metal chelates are promising candidates to replace platinum based ORR catalysts at the cathode of PEMFCs based on their comparable activity to platinum so far.[9,11] However, to fundamentally understand the ORR mechanism of this class of catalysts, non-pyrolyzed metal chelates are of interest due to their well-preserved structures and controllable active sites, though their activities are poor.

In the complex systems with porphyrin/phenanthroline/phthalocyanine, Co and Fe are the two most active transition metals compared to Cu, the metal used in nature. Many studies came to a consensus that central metals act as electron donors with *d* orbital electrons and O_2 as electron acceptor into its antibonding π^* during ORR catalysis.[26,28,29,33] Two major concerns during bonding are the matched symmetry and energy gap with the O_2 antibonding π^* orbital. MO theory is classic and popular in explaining the observation of Me-Pc/porphyrin compound-based ORR catalysts. However, it requires a good knowledge of the structure of the compounds to provide

information about energy levels of d orbitals. For instance, the structure of Cu(II)-DATZ complexes vary significantly from synthesis procedure. It is difficult to apply MO theory rigorously without knowing the coordination geometries.

Magnetic properties have not often been examined for metal chelates-based non-precious metal catalysts so far. The relationship between the ORR performance and magnetic properties remains unknown. The trend between the performance and redox potential varies with metals, ligands from different research groups.

To elucidate the mechanism of ORR catalyzed by metal chelate-based catalysts, it would be helpful to capture the reaction intermediates by introducing spectroscopic techniques in catalytic process. With more knowledge of the ORR mechanisms, metal chelate systems can be tailored to gain improved ORR catalytic activities.

Although Cu-containing enzymes remain the best ORR catalyst in nature, mimicking its activity by synthetic compounds is still elusive. Understanding the nature of enzymes will offer more guidance when conducting the compound synthesis. However, new types of copper compounds are required to achieve the full potential of Cu(II) in ORR catalysis.

1.5 Overview

The intellectual contribution of this work is to add to the fundamental understanding of ORR by metal chelates based electrocatalysts and provide guidance in synthesizing better non-precious metal catalysts for ORR. Unlike traditional ligands porphyrin/phenanthroline/phthalocyanines, 1,2,4-triazole possesses small heterogeneous and cyclic and aromatic structure and can contribute to highly diverse complexes with metals. Metal-triazole complexes are important due to their significance to multinuclear catalysis and biomimetic study.

In chapter 2, starting from scratch, synthesis conditions including carbon supports, carbon pretreatment, Cu/DATZ ratio, Nafion ionomer/catalyst ratio and copper salts are explored. The ORR activity and stability of Cu(II)-DATZ-based catalysts are improved in acidic conditions.

In chapter 3, RRDE is employed to characterize this catalyst electrochemically. A strategy for probing the mechanistic aspects of ORR by Cu(II)-DATZ-based catalysts in acidic medium is developed. Kinetic parameters including Tafel slopes and reaction orders of possible intermediates were calculated. An ORR mechanism for this catalyst is proposed and discussed.

In chapter 4, the electronic properties of catalysts are varied by introducing functional groups on the ligand. Mulliken charges of the ligands are calculated and correlated to the ORR performance of substituted catalysts for the first time. Electron donating groups are found favorable for ORR catalysis.

In chapter 5, to investigate the complex structures in the five substituted catalysts, ATR (attenuated total reflectance)-FTIR, elemental analysis and EPR spectroscopy were adopted to provide information related to the Cu/ligand ratio and the coordination geometry of Cu(II) centers.

In chapter 6, since *ex situ* techniques can only provide limited information about the structures of Cu complexes, an *in situ* electrochemical cell was designed for use in the EPR spectrometer. Direct observation of the spectroscopic features and electrochemical behavior of the catalyst was realized with this cell.

In chapter 7, the sensitivity of EPR provides for quantitative study. This work started from validating the electrochemical performance with the conventional RDE cell. A semi-quantitative analysis based on the *in situ* technique was developed.

In chapter 8, to realize the initial idea of designing this *in situ* electrochemical cell, which is probing the ORR mechanism of non precious metal catalyst of high performance, the *in situ* technique was employed to study a catalyst as prepared and its pyrolyzed sample which demonstrates the best ORR activity in acid media among the Cu catalysts synthesized so far.

2 Electrochemical characterization of ORR by copper complex-based electrocatalysts

2.1 Introduction

Copper containing enzymes have demonstrated the highest ORR activity in neutral conditions in nature.[12] Multiple Cu centers surrounded by imidazole and side chains of histidine in these enzymes were identified as catalytic centers for ORR.[16,23,24] Some might suggest using imidazole as a ligand rather than DATZ to mimic the catalytic centers in the copper containing enzymes. However, in our preliminary work, synthesis simply by mixing carbon support, and copper and imidazole solutions did not result in catalysts demonstrating significant ORR activity. Cu-DATZ complex-based catalysts exhibited an ORR onset potential of 0.73V at pH=7.[32] Later this Cu-DATZ complex-based catalyst was applied as a cathode catalyst for alkaline fuel cells and showed activity comparable to a Pt/C catalyst.[85] Porphyrins, phthalocyanine and phenanthrolines are typical ligands for complexing $Fe^{2+/3+}$ and Co^{2+}. However, their Cu counterparts with these ligands did not exhibit significant ORR activity compared to Fe and Co complexes.[1,35,36,86–91]

In this study, Cu-triazole based complexes will be the focus, with a goal of understanding the ORR mechanism more fundamentally. DATZ opens more possibilities of structures of carbon-supported complexes as a ligand due to the great diversity of Cu-DATZ complexes.[40–42,92] With an optimized synthesis procedure and electrode preparation, the activity of this complex could potentially be improved. This study also offers a better chance to construct model complexes similar to those in the natural enzymes.

In this part, we describe optimization of synthesis conditions including carbon supports and pretreatment, ligand/metal ratio, reaction time and temperature, and copper salts. Electrode preparation conditions were explored including Nafion/catalyst ratio, ink stirring time and electrolyte concentrations to obtain optimal ORR performance of the RRDE test of the catalysts. Nafion acts as a binder between Pt based catalysts and membrane electrolyte and a proton conductor in the membrane electrolyte in PEMFCs.[93–95] The stirring time of ink (catalyst, Nafion and methanol solution) is related to the homogeneity and dispersion of the catalyst layer after depositing the ink on glassy carbon disk electrode. Proper concentration of electrolyte provides acidic environment similar to that in PEMFCs and avoids use of unnecessarily high concentration of electrolyte to reduce the test cost of using highly pure concentrated sulfuric acid. Among these factors, the impact of carbon supports, carbon support pretreatment, Cu/DATZ ratio, Nafion/catalyst ratio and different copper salts will be discussed.

2.2 Experimental procedures

2.2.1 Chemicals

Aqueous solutions were prepared using distilled water purified through a Millipore water system. 1H-1,2,4-triazole-3,5-diamine (DATZ) was purchased from Acros Organics. Black Pearls 2000 (BP2K) and Vulcan XC72R (VX72) were provided by Cabot Corporation. KetjenBlack EC300J (KB) was from AkzoNoble. Copper salts ($Cu(OAc)_2 \cdot H_2O$, $CuSO_4 \cdot 5H_2O$, $Cu(OTf)_2$ [OTf=$CF_3SO_3^-$], $Cu(ClO_4)_2 \cdot 6H_2O$, $CuCl_2 \cdot 2H_2O$, $Cu(NO_3)_2 \cdot 3H_2O$, $Cu(BF_4)_2$) were purchased from Aldrich, and used as received. All the gases (pure N_2, O_2 and H_2) used in this study were ultra-pure grade and provided by

Airgas. Nafion ionomer solution (5 wt. %) and methanol for ink preparation were from Aldrich. H_2SO_4 (99.9999%) is from Alfa Aesar and used only for electrolyte preparation.

2.2.2 Complexation

Catalysts were prepared by soaking modified carbon support substrates (50 mg) in the solution of ligands (1 mmol) and Cu(II) salts (0.5 mmol) at 80 ^{o}C and stirred for 2 hours. The total volume of reaction system was 5 ml. Then the reaction mixture was centrifuged. The supernatant was saved for ICP. The Cu(II) loading in the catalyst was determined by ICP by calculating the difference between the total amount of Cu(II) added into the reaction system and the amount left in the supernatant obtained from centrifugation. This difference can estimate the maximum possible Cu(II) adsorbed by carbon support. One example of calculation based on the experiment of Cu(II)-DATZ-based catalyst is shown below.

$$\frac{\text{Adsorbed Cu(II) amount (mmol)}}{\text{carbon support (g)}} = \frac{\text{Total Cu(II) amount added(mmol)} - \text{Cu(II)amount left in the supernatant (mmol)}}{50\ mg\ carbon\ support} \quad (2.1)$$

$$Total\ Cu(II) amount\ added(mmol) = 0.167\ M \times 3.28\ ml = 0.551\ mmol$$

The concentration of Cu(II) stock solution determined by ICP was 0.167 M. The concentration of stock solution was measured before and after complexation experiment. The value after complexation experiment was used to estimate the total amount of Cu(II) added into the reaction system. The volume of Cu stock solution added to the reaction system was 3.28 ml and measured using a pipette.

$$\text{Cu(II)amount left in the supernatant (mmol)} = 0.0359\ M \times 5\ ml = 0.176\ mmol$$

The concentration of Cu(II) in the supernatant determined by ICP was 0.0352 M. The volume of the supernatant was 5 ml and measured by the volume of total solution.

According to equation 2.1,

$$Adsorbed\ Cu(II) amount\ \left(\frac{mmol}{g}\right) = \frac{(0.551 - 0.176)/0.551 \times 0.5}{50/1000}\ \frac{mmol}{g}$$

$$= 6.81\ mmol/g$$

The solid residue was washed sequentially with 5 ml each of water, methanol and acetone and then dried in a vacuum oven at 75 °C for 3 hours. All the washing and drying conditions are as above unless specified. The supernatants from water wash step were taken for ICP measurement. These wash steps were intended to clean the catalyst surface by reducing the amount of the weakly adsorbed Cu(II) on the carbon support. Methanol and acetone wash makes the water in the catalyst to dry faster.

2.2.3 Carbon surface diazotization (diazonium coupling)

The surface of the carbon support was modified by reacting BP2K with acetic acid and isoamyl nitrite in acetonitrile at room temperature for 2 hours.[96,97] Then the suspension was centrifuged and the residue was washed and dried in the vacuum oven for use in the complexation reaction.

2.2.4 Carbon surface oxidation

Carbon supports (BP2K) were soaked in a solution of oxidant H_2O_2 (30 wt. %) or ammonium peroxydisulfate (APS) and H_2SO_4 or HNO_3 at conditions indicated specifically in Fig. 2.3b. The mixture was then centrifuged and washed and dried in a vacuum oven before complexation. These oxidized carbon supports were used for complexation reaction to synthesize catalysts. The scheme of diazotization, oxidation and

complexation is depicted in Fig. 2.1. The oxidation methods applied will be explained in the results and discussion part.

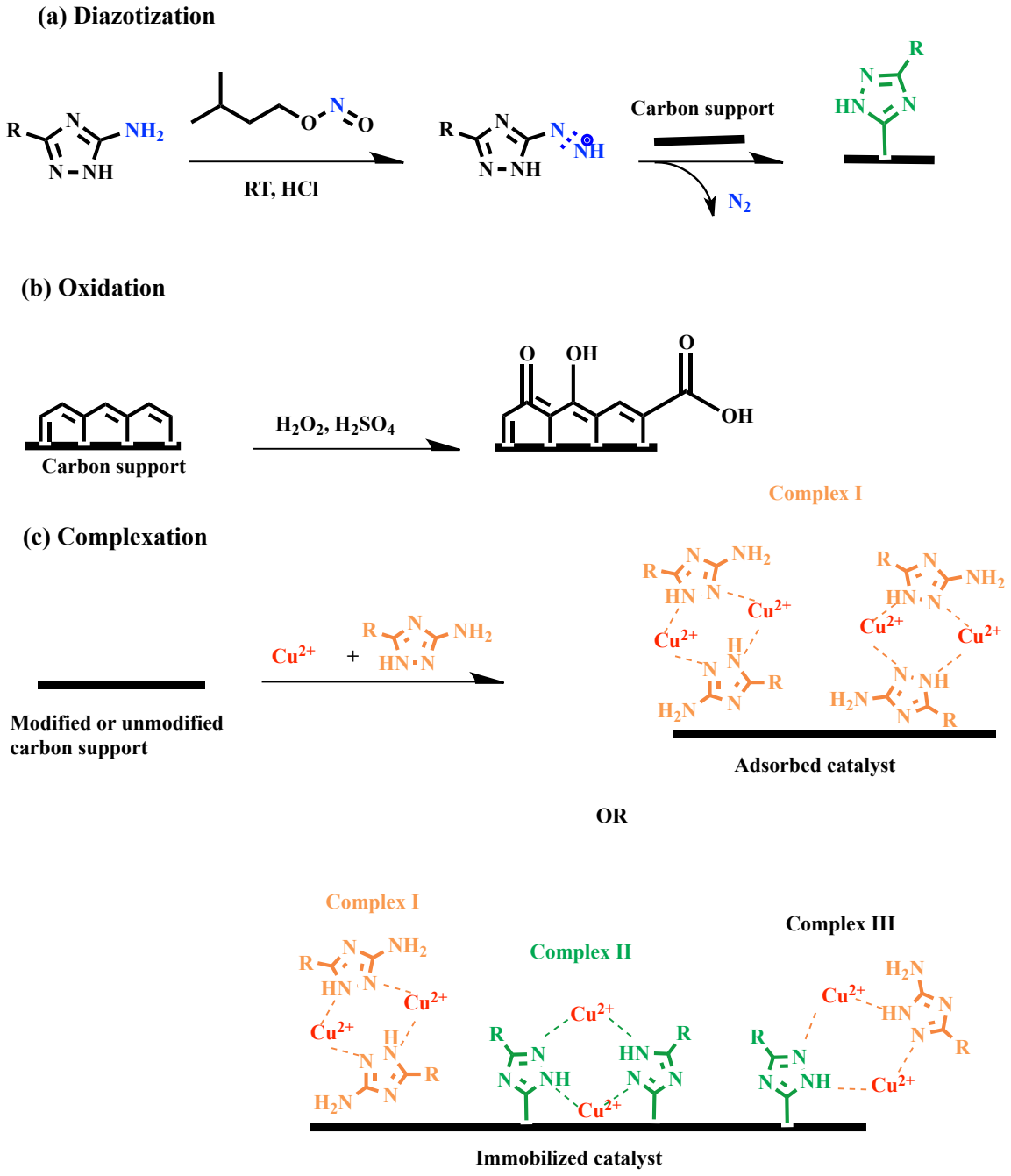


Figure 2.1 Synthesis approaches: (a) Diazotization (b) Oxidation and (c) Complexation

2.2.5 Electrode preparation from synthesized catalysts

All synthesized catalysts were ground in a silica mortar before ink preparation. Inks were prepared using 5 wt% Nafion solution in a 40/60 ionomer-to-catalyst ratio, with methanol as the solvent unless specified. Catalyst inks were stirred at 400 rpm for about 5 days on a stir plate before electrochemical testing.

2.2.6 Rotating ring-disk electrode technique (RRDE) and Cyclic Voltammetry (CV).

A three-electrode cell, consisting of the working electrode, a Hg/Hg_2SO_4 reference electrode and a gold wire as the counter electrode, was used. The working electrode was purchased from Pine Instrument Company and consists of a glassy carbon (GC) disk with surface area 0.2472 cm^2 and supported a thin film of synthesized catalysts and a platinum ring electrode. The standard electrochemical test conditions are described below. A catalyst loading of 600 ± 100 $\mu g/cm^2$ was deposited on the disk electrode for each sample. Unless specified, the electrochemical test conditions are at 10 mV/s and 1600 rpm for RRDE experiment and 0 rpm for CV experiment in 0.1 M H_2SO_4. All the potentials are reported versus reversible hydrogen electrode (RHE).

Fig. 2.2 shows a typical cathodic curve from RRDE experiment in 0.1 M H_2SO_4 saturated with O_2 at 1600 rpm. Onset potential is the potential where the current density deviates from 0. In our study, onset potentials were taken when the current densities are -5$\mu A/cm^2$ for all the samples. The diffusion-limited regime on cathodic RDE curve is the current plateau part independent of potential applied. At kinetic-controlled regime, the effect of mass transport could be negligible. The limiting current is observed when the rate of reaction is much greater than the rate of mass transport. The limiting current for a rotating disk electrode is described by Levich equation, as shown in equation 2.2.

$$J_L = 0.62nFD_O^{2/3}\upsilon^{-1/6}C_O^*\omega^{1/2} \qquad (2.2)$$

Where n is the number of electrons transferred, F is the Faraday's constant, *Do* is the diffusion coefficient of O_2 ($1.4x10^{-5}$ cm^2 s^{-1}) in 0.1M H_2SO_4, ν is the kinematic viscosity, C_O^* is the bulk concentration of oxygen ($1.1x10^{-6}$ mol cm^{-3}) and ω is the angular velocity of the disk electrode (1600 rpm).

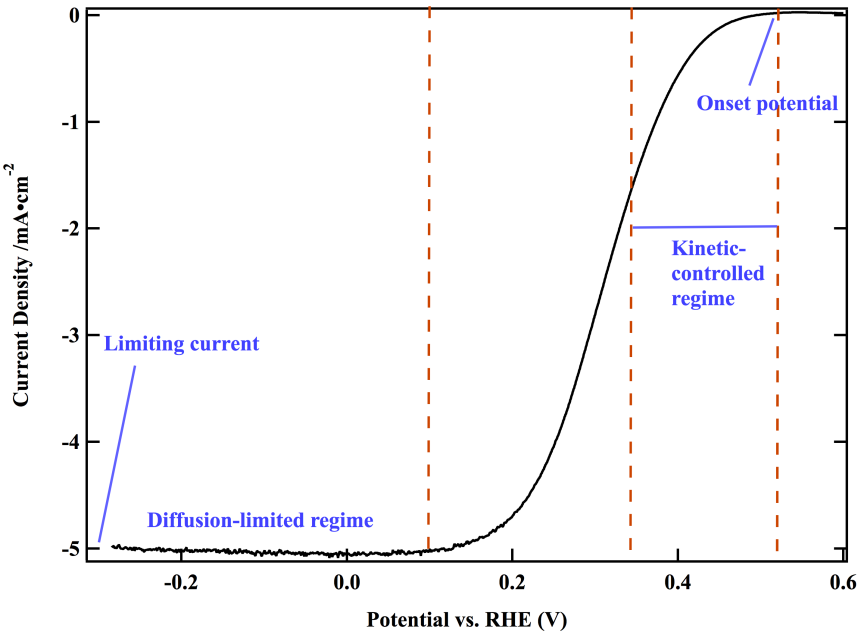


Figure 2.2 Typical cathodic curve from RRDE experiment in O_2 saturated electrolyte at 1600 rpm.

2.2.7 Inductively coupled plasma (ICP)-optical emission spectrometry (OES)

ICP was used to monitor the Cu(II) solution concentrations obtained before and after the complexation reaction and catalyst synthesis. The characteristic wavelengths 324.752nm and 327.393nm were chosen based on their good linearity of standard solutions (with relative coefficient 0.99 or above) and triplicate experiments were conducted for each wavelength. The concentration of solution was determined by the

mean data taken from the values produced according to the two wavelengths. Standard solutions used are 1, 10, 25, 50, 100 mg/L Cu(II) in 2% nitric acid to calibrate the standard curve. Dilutions of solution ensure that the detected concentrations fall around 0.2mM or ca. 13 mg/L.

2.3 Dependence of ORR performance for adsorbed catalysts on different carbon supports and oxidation pretreatment

The properties of the carbon support, including surface functionalities, degree of disordered phase, N content and microporosity, surface area have been extensively investigated among pyrolyzed catalysts.[56,74,77,79,80,84,98] These features of carbon supports also play important roles in affecting the ORR activity of carbon-supported complexes but have not yet been studied extensively for non-pyrolyzed catalysts. In the context of DATZ and $Cu(NO_3)_2$ complexes formed in the presence of carbon supports, the chemical moieties on the carbon surfaces may function as co-ligands either by participation in metal coordination or by pre-organizing a network of ligands for metal binding.[99] Three carbon supports, BP2K, KB and VX72, were used to synthesize adsorbed catalysts, as shown in Fig. 2.3a.

Table 2.1 Properties of different carbon supports[100] (data from reference 102)

Carbon	Surface area (m^2/g^{-1})	Mesopore area (m^2/g^{-1})	Micropore area (m^2/g^{-1})	Pariticle size (nm)
Vulcan XC-72R	235	76	118	30
Ketjenblack EC 300J	829	680	55	30
Black Pearls 2000	1487	475	720	12

The catalysts based on BP2K and KB show better ORR performance (Fig. 2.3a) than the one based on VX72, evidenced by comparing limiting current and onset potentials of ORR. Similar ORR performance was observed when using BP2K and KB as carbon supports. The possible reason for the lower performance of VX72 is the considerably lower surface area and micropore volume compared to BP2K.[101] From Table 2.1, VX72 has higher area of micropores than KB but significantly lower area of mesopores than KB.[100] This suggests that the area of mesopores is one of the important factors affecting ORR activity of the catalysts. Their particle sizes are similar but both are much larger than the particle size of BP2K. Due to the highest surface area, area of micropores and the smallest particle size of BP2K among these three carbon supports, in later sections, BP2K will be chosen as the only carbon support for catalyst synthesis.

The functionalized carbon support is important in the catalytic application of carbon-supported materials. The chemical oxidation of carbon supports is a proven method for generating oxygen-containing functional groups and these types of surface modifications have shown promise in heterogeneous catalysts for ORR.[73] As mentioned in the literature review, the oxygen functional groups associated with the edge carbon atoms act as anchoring sites for the FePc particles and ensure a higher state of dispersion of the complexes.[79] This dispersion effect of oxygen functionality has also been reported in multiple reports and also explained as increasing the polarity of carbon supports.[75,77,102–104] A common approach for introducing oxygen functionalities is pretreating the carbon support with a solution of HNO_3. Pretreatment of carbon support in peroxide solutions might increase the tolerance to peroxide that is considered an important side product during ORR.

Four oxidation pretreatments on BP2K are shown in the legend of Fig. 2.3b. APS (ammonium persulfate) is an oxidant and has been used in synthesizing high performance electrocatalysts derived from Fe, Co, and polyaniline.[43] Pre-leaching the carbon support in H_2SO_4 removes the unstable and inactive species from the carbon that could possibly strip off in the acidic electrolyte and actually cleans the carbon support.[43] Another explanation for improved performance after introducing oxygen functionalities is that oxygen could appear as a 5th ligand at the axial position of metal square planar geometry and affect the energy levels of dz^2 in metal.[8] This explanation is better applied to non-pyrolyzed metal chelate-based catalysts since the coordination geometries of pyrolyzed catalysts are less certain. Among these four oxidation pretreatments on BP2K, the sample treated with the $H_2O_2/H_2SO_4/25\ ^oC$/14 hours protocol gives the best performance, with an onset potential of 0.46 V vs. RHE. Results are shown in Fig. 2.3b. The best performance was possibly attributed to the long pretreatment time, 14 hours, resulting in a higher concentration of oxygen functionalities on the carbon surface. The samples treated with all other three pretreatment methods demonstrate similar ORR performance. The one treated with $APS/H_2SO_4/25^oC$/3hours shows a slightly lower onset potential than the samples treated with $APS/H_2SO_4/80^oC$/3hours and $APS/HNO_3/80^oC$/30min. This suggests that higher temperature is favorable for the ORR performance when the oxidant is APS. In the treatment $APS/H_2SO_4/80^oC$/3hours and $APS/HNO_3/80^oC$/30min, the ORR performance of catalysts are very similar, indicating longer pretreatment time, either H_2SO_4 or HNO_3 in the solution do not lead to a significant change in the ORR performance of the catalysts. However, compared to the treatment $H_2O_2/H_2SO_4/25^oC$/14hours, H_2O_2 and longer hours improves the ORR performance of

the catalyst significantly. The number of electrons transferred was calculated by equation 2.3 and was larger than 3.9 in the limiting current region from Fig 2.3c. This suggests that higher concentration of oxygen functionalities facilitates the ORR more towards 4e- reaction. Based on these findings, this method is employed whenever an oxidized carbon support is mentioned in the future experiments. The number of electrons, n, transferred at any potential is determined by the rotating ring-disk electrode experiment via the following equation:

$$n = \frac{4I_d}{I_d + \frac{I_r}{N}} \qquad (2.3)$$

Where n is the number of electrons transferred for O_2 reduction, I_d is the current measured from the disk electrode, I_r is the current measured from the ring electrode while holding the ring electrode potential at 1.2 V, N is the collection efficiency, theoretically 37% based on the geometry of the disk and ring electrode. This value has been experimentally checked periodically by $Fe(CN)_6^{3-}/Fe(CN)_6^{4-}$ redox couple. The production of hydrogen peroxide of the catalyst is less when n value is closer to 4.

2.4 Dependence of ORR performance for covalently bonded catalysts obtained via carbon diazotization

Cu and DATZ solutions were observed to form insoluble compounds when mixed at an elevated temperature. Unlike Cu-porphyrin/phenanthroline complex-based catalysts, which require adsorption of complexes from the solution phase, insoluble Cu-DATZ complexes could potentially demonstrate improved stability.[38,105] However, in the strong acidic environment of PEMFCs, the stability of Cu-DATZ complexes still needs to be improved.[32]

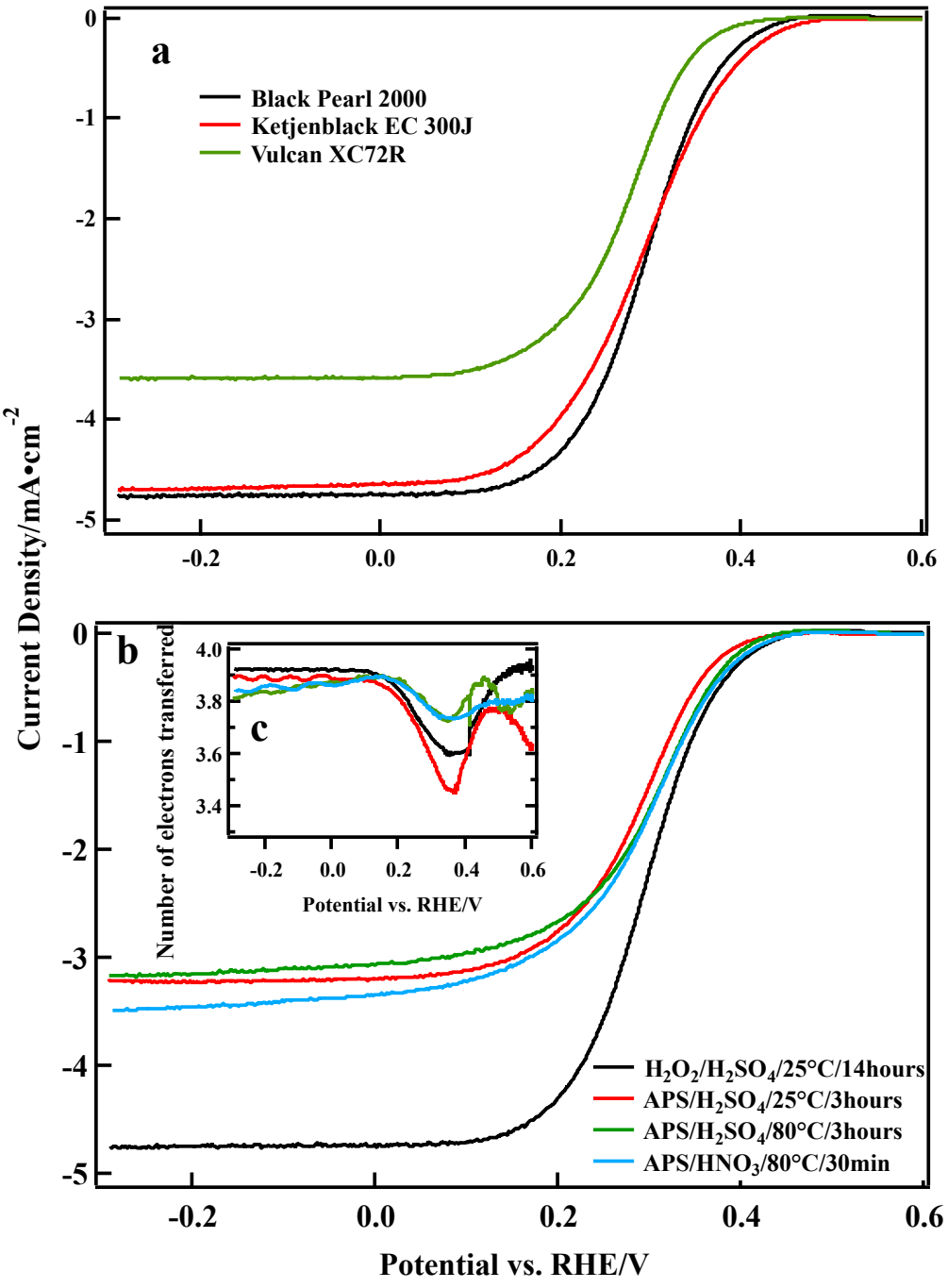


Figure 2.3 a. RDE cathodic curves in O_2 saturated electrolyte of adsorbed $Cu(OAc)_2$-DATZ catalysts synthesized based on a. three carbon support BP2K, KB and Vulcan X72 oxidized by soaking them in 30% H_2O_2, 0.5M H_2SO_4 for 14 hours at RT. b. BP2K oxidized by four different conditions: 30% H_2O_2, 0.5M H_2SO_4 at 25°C for 14 hours; APS (ammonium persulfate), 0.5M H_2SO_4 at 25°C for 3 hours; APS, H_2SO_4 at 80°C for 3 hours; APS, HNO_3 at 80°C for 30min. c. Number of electrons transferred for catalysts based on four oxidized carbon.

One possible means to bring this about is by linking the Cu-DATZ complexes on the carbon surface by a chemical bond so that Cu-DATZ complexes could not be removed unless the chemical bond is broken. This hypothesis is based on the assumption that Cu-DATZ complexes contribute to or are the catalytic centers of this catalyst.

In diazotization pretreatment, the carbon surface was covalently bonded to the 3-amine on amino-triazole through diazotization chemistry.[96] The scheme of diazotization is shown in Fig. 2.1a. Subsequently, copper acetate and extra ligands were added to form complexes on the modified carbon surface. Catalysts synthesized according to this scheme are referred to hereafter as immobilized catalysts. Catalysts prepared without diazotization modification are referred as 'adsorbed catalysts'. The ORR stability of adsorbed and immobilized catalysts was compared through a stability test. Fig. 2.4 shows the ORR cathodic curves of immobilized and adsorbed catalysts based on Cu(II)-DATZ complexes before and after cycling in O_2 saturated 0.1M H_2SO_4 electrolyte for 2000 times at 0.2-0.7V. The activities of immobilized and adsorbed catalysts are very similar before cycling. However, after 2000 cycles in O_2 saturated electrolyte, the adsorbed catalyst exhibits a larger activity decrease from its initial activity in the half-wave potential, though the limiting current actually is slightly higher. The amount of Cu(II) in immobilized catalyst, as determined by ICP, is about 7% higher than that in adsorbed catalysts initially. This suggests that ligands covalently bonded on the carbon surface might facilitate the binding of Cu(II) to the surface to form complexes II and III, as shown in Fig. 2.1c.

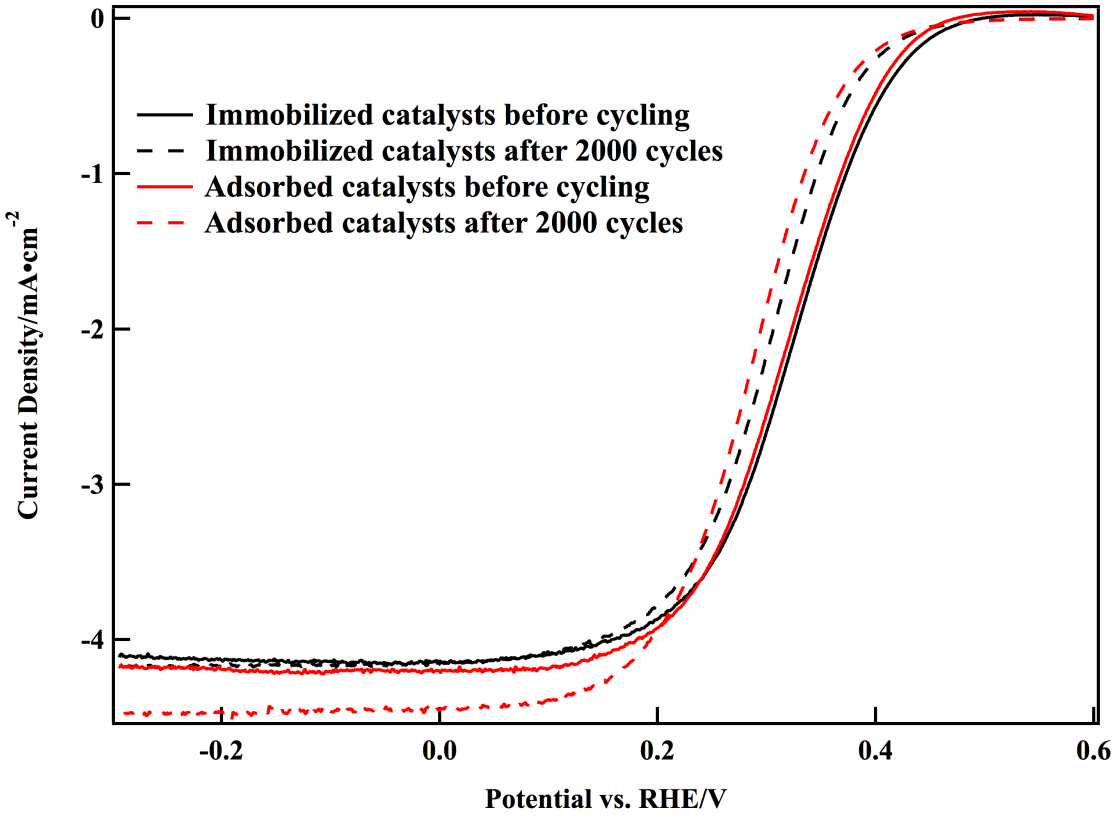


Figure 2.4 RDE cathodic curves of adsorbed and immobilized catalysts synthesized based on Cu(II)/DATZ complexes before and after 2000 cycles in O_2 saturated 0.1M H_2SO_4 electrolyte at potential 0.2-0.7V.

To investigate complex adsorption on diazotization-modified carbon, RDE and CV experiments were conducted on three materials: diazotization-modified carbon with either Cu(II) or DATZ in the solution, and immobilized catalyst with both Cu(II) and DATZ in the solution. The results are shown in Fig. 2.5. The three samples demonstrate different ORR activities. Comparison of the various CVs indicates that the redox peaks are due to Cu(II) in the materials rather than DATZ on BP2K or BP2K itself. Two anodic peaks (a small one around 0.32V, a major one around 0.56V) are observed from the CVs of diazotization-modified carbon with Cu(II), and with Cu(II) and DATZ, indicating there might be two redox couples. The anodic peak around 0.32 V disappears after

multiple scans in the electrolyte. The major redox peaks are attributed to Cu(II)/Cu(I) in the complex. To make sure that the small anodic peak is not due to another redox couple, such as Cu(I)/Cu(0), a CV, as indicated in the inset of Fig. 2.5b, was scanned at a slow scan rate, 1 mV/s, with the purpose of distinguishing the peak of possible redox couple Cu(I)/Cu(0) from the peak of Cu(II)/Cu(I). It showed similar shape as the one in Fig. 2.5b with a scan rate of 10 mV/s. Therefore the possibility of redox couple Cu(I)/Cu(0) was excluded. This double voltammetric peaks might be some geometric rearrangement of the complexes on carbon surface.[106] According to the reaction scheme shown in Fig. 2.1c, complex II will be the proposed form in diazotization-modified carbon with only Cu(II). complex I, II, III are all possible in diazotization-modified carbon with Cu(II) and DATZ. The redox potentials are calculated from the major peaks in CVs as 0.47V and 0.48V for diazotization modified carbon with only Cu(II) and diazotization modified carbon with Cu(II) and DATZ respectively. This suggests that complex I, II and III have similar redox potentials and covalently bonded DATZs coordinate Cu(II) in a similar way as free DATZs in solution. The ORR performance of the three samples decreases in the order of (i) catalyst > (ii) modified carbon with only Cu(II) > (iii) modified carbon with only DATZ. This indicates that the presence of Cu(II)-DATZ complexes contributes to more active ORR catalytic centers.

The redox charge q associated with the Cu(II)/Cu(I) is a direct measure of the amount of complex that is electroactive. It can be calculated from the integral of reduction current over time. The redox charges q were calculated as 0.1379 and 2.697 mC for diazotization modified BP2K reacting with Cu(II) and catalyst, respectively, after subtracting current due to capacitance. However the Cu(II) loadings from ICP measurement for diazotization

modified BP2K reacting with Cu(II) and catalyst are 2.74 and 6.16 mmol/g respectively. The Cu(II) loadings measured by ICP are about double while the ratio of redox charges is about 20 times. This inconsistency probably arises because without the presence of DATZ, the Cu(II) ions adsorbed on modified carbon surface are weakly bound and could be removed easily in the wash steps or in the electrolyte during electrochemical test.

2.5 Decomposition mechanism of immobilized catalysts based on Cu-DATZ

To understand the decomposition mechanism of the Cu-DATZ based immobilized catalyst, the ring electrode of an RRDE was held at 1.2 V to detect possible decomposed Cu(I) and at -0.2 V for possible Cu(II) from the disk electrode respectively during a voltammetric scan with rotation in N_2 saturated electrolyte. However, no ring current was detected while holding ring electrode at 1.2 V. This is an indication no Cu(I) escaped from the disk electrode during the CV. However, when the ring electrode is held at -0.2V, the ring current deviates from the baseline when the potential is more positive than 0.35 V. The data is shown in Fig. 2.6. For both cathodic and anodic scan, the deviation occurs at potentials larger than 0.35V. For the anodic scan, the deviation of ring current from baseline occurs at a more negative potential 0.2 V. This suggests that Cu(II) in the catalyst starts to come off the disk electrode when the Cu(II)/Cu(I) ratio is beyond a certain value. When the ratio is lower than this value, Cu(II) is not observed. The fact that Cu(I) did not come off the disk electrode while Cu(II) did suggests different coordination environments of Cu(II) and Cu(I) in the catalyst. The coordination equilibrium between Cu species and ligand on carbon surface builds up quicker for Cu(I) species than for Cu(II) species, leading to a loss of Cu(II) when there is more Cu(II) present at more positive potential region.

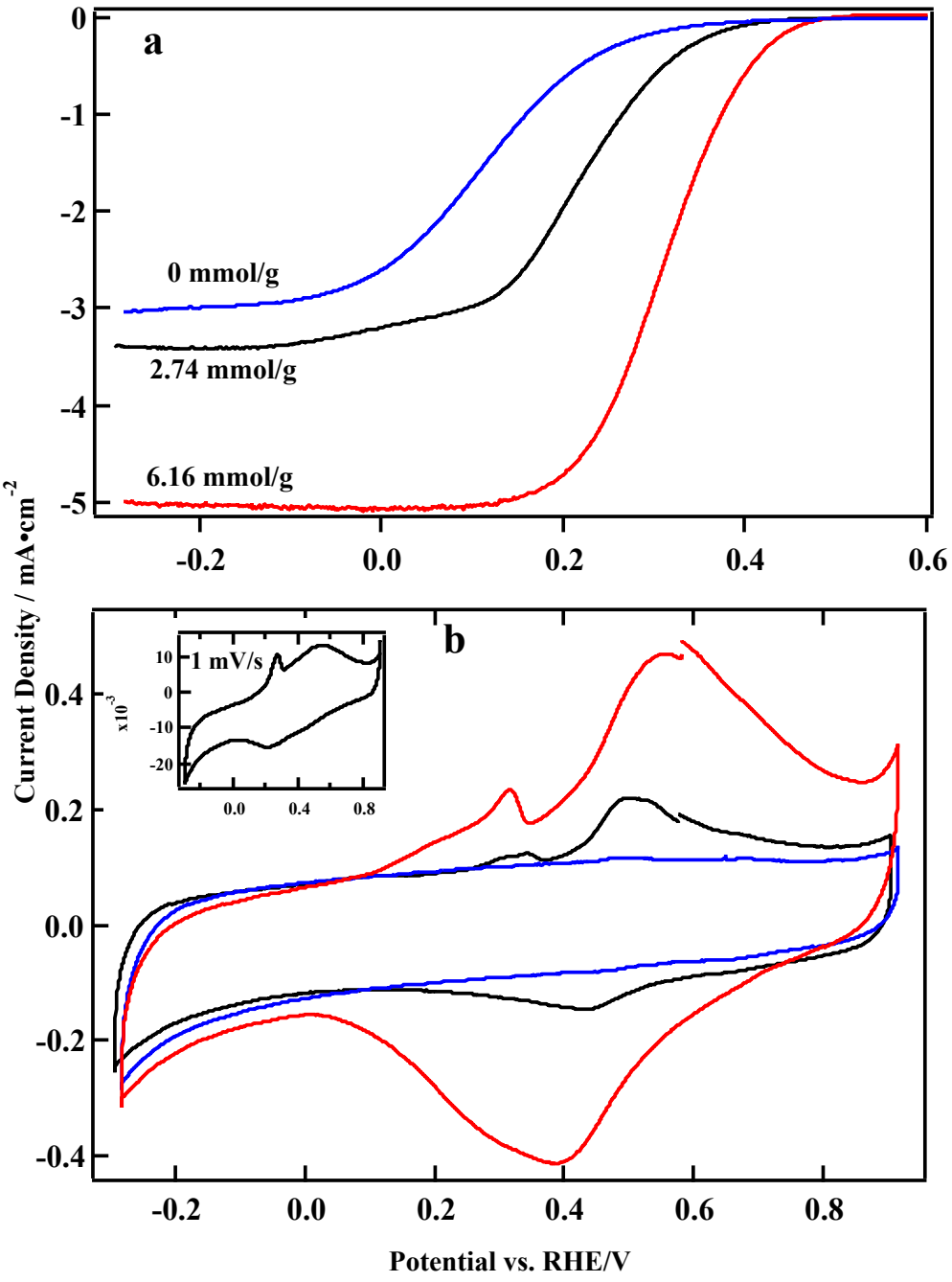


Figure 2.5 a. RDE cathodic curves in O_2 saturated electrolyte and b. CVs in N_2 saturated electrolyte of (iii) diazotization-modified BP2K reacting with extra DATZ(Blue), (ii) diazotization modified BP2K reacting with extra $Cu(OAc)_2$(red), (i) catalyst: diazotization modified BP2K reacting with both extra $Cu(OAc)_2$ and DATZ(black) in the solution. The Cu(II) loadings in the samples are shown in (a) as mmol/g and determined by ICP from synthesis. inset of b: CV in N_2 saturated electrolyte at scan rate of 1 mV/s.

No experiment has been done to use the ring electrode to detect the decomposed Cu(I) or Cu(II) coming off the disk electrode. Similar conclusions about the surface equilibrium of Cu(II) and Cu(I) were made by Lei and Anson from the double peaks present in the CVs of Cu-phenanthroline complexes on graphite electrode.[107] The baseline current of the ring electrode starts from -0.16 mA while holding the ring electrode potential at -0.2 V. This is caused by the reduction of H^+ in the electrolyte at this potential on the platinum ring.

2.6 Dependence of ORR activity on different Cu/DATZ ratio in the synthesis

Unlike ligands with large π conjugated systems (Pc, phthalocyanine, phenanthroline), the triazole ring has a relatively small aromatic ring with multiple non-equivalent N donors. This results in the possibility of much higher diversity of metal-DATZ complexes during synthesis.[39–41] Aznar *et al*. obtained two Cu-DATZ complexes by variation of synthesis conditions. Crystal structure studies show that a Cu/DATZ ratio of one complex is 2:2 and the other one is 3:4 and all Cu complexes have a square planar structure with different degree of distortion at the axial position.[39] In these complexes, N1 and N2 coordination is the major coordination mode and this could potentially bridge metal ions to afford polynuclear compounds with anions as additional bridge or co-ligand.

To explore the optimal ratio of Cu/DATZ in synthesis, the amount of DATZ were adjusted to 0.5, 1, 2, 3, 4, 5 equivalents of Cu amount added based on dizotization modified carbon support. Their performance is shown in Fig. 2.7. The best performance of ORR was achieved when Cu/DATZ ratio is 1:3. When the Cu/DATZ ratio decreases from 2:1 to 1:3, the ORR performance is improved dramatically. However, when the Cu/DATZ ratio is lower than 1:3, the performance decreases gradually and slightly more as the ratio decreases.

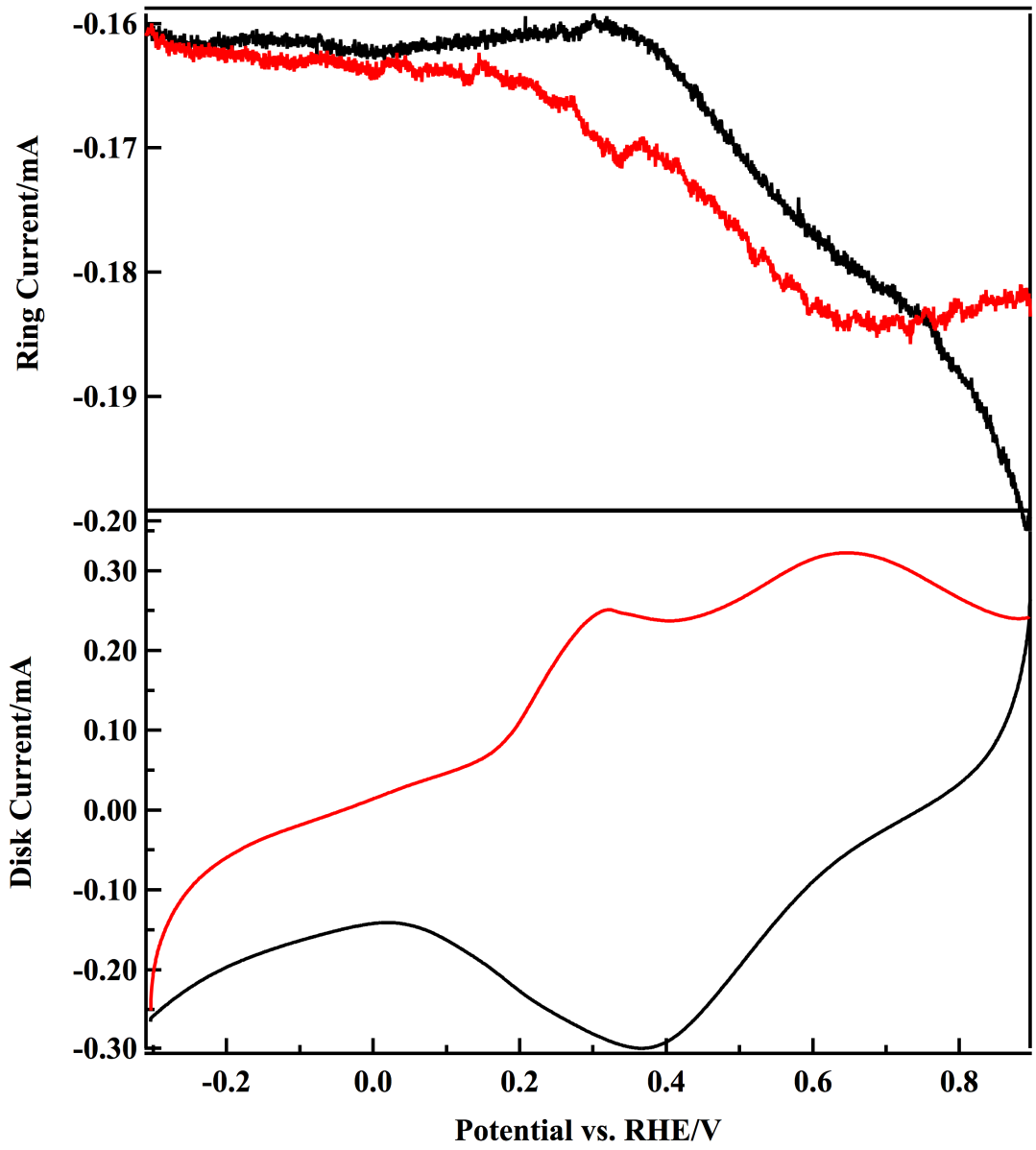


Figure 2.6 Disk (lower panel) and ring (upper panel) currents in a CV of immobilized catalyst based on Cu-DATZ complexes in the N_2 saturated electrolyte while holding the ring electrode potential at -0.2 V vs. RHE, the rotation rate is 1600 rpm. The curve in red indicates anodic scan. The curve in black cathodic scan.

The redox peaks of Cu(II)/Cu(I) appear at the similar potentials for all samples. The cathodic peak of CVs in the presence of N_2 shows that the electroactive species are the lowest when the ratio is 1:4 and 1:5. This could be explained that when there is more DATZ present, more Cu-DATZ precipitates, supported by the higher recovered mass

after synthesis in Table 2.2 for samples with Cu/DATZ ratios lower than 1:3. This results in smaller amounts of complexes available for being adsorbed on carbon surface.The recovered mass are listed in Table 2.2.

Table 2.2 Recovered mass for samples with different Cu:DATZ ratios added after synthesis

Cu:DATZ added	1:0.5	1:1	1:2	1:3	1:4	1:5
Recovered mass (mg)	82.72	108.48	112.90	116.60	114.66	115.0

Additionally, these precipitated Cu-DATZ complexes are not as catalytically active as those adsorbed on carbon surface, shown by the decreasing ORR performance when the ratios are lower than 1:3. The function of the ligand could be to act as a connector between the metal and carbon support for the catalyst to be catalytically active, which is analogous to the N donors in the enzymes linking the metal sites and protein.[19,108] The number of electrons transferred are all larger than 3.9 except the case of ratio 2:1, indicating 95% of O_2 reacted at the electrode is reduced through a 4e- process. This indicates that Cu-DATZ complexes formed at ratio Cu/DATZ higher than 2:1 are highly selective towards 4e- reaction. The redox potentials of Cu-DATZ complexes are measured by taking the average potentials where the major redox peaks occur, which are marked in Fig. 2.7b. As the ratio decreases from 2:1 to 1:2, the redox potentials slightly increases with a smaller peak separation and so do the ORR half-wave and onset potentials. The redox potentials are similar when the ratios are 1:3 and 1:2. As the ratio of Cu/DATZ decreases from 1:3 to 1:4, the redox potentials shift towards more negative values with larger peak separation. The ORR onset potentials and half-wave potentials

reach at the highest values when the Cu/DATZ ratio is 1:3. It seems that higher redox potentials of Cu-DATZ are related to higher ORR performance with the observation above. Optimization of metal:ligand ratio in other complexes such as metal-phenanthroline/phthalocyanine/porphrin was barely seen in the literature. One possible reason is that these ligands have specific binding sites nitrogen in the ring with metal, as shown in Fig. 1.1. The structural diversity of these complexes is low due to this reason. This also implies that the great diversity of complexes based on Cu-1,2,4-triazole and its derivatives.

2.7 Dependence of ORR performance on catalyst/Nafion ionomer ratio

The dependence of catalyst layer performance on Nafion ionomer/catalyst ratio (I/C) has been extensively studied to understand the role of Nafion ionomer in the catalyst layer and its effect on the performance of PEMFCs.[93–95,109,110] A picture of membrane-electrode assembly (MEA) is depicted in Fig. 2.8. MEA consists of three parts: membrane electrolyte, catalyst layer and gas diffusion electrode. Catalyst is normally mixed with ionomer in achonol and then coated on the membrane made from ionomer. This catalyst coated membrane assembled with gas diffusion electrode composes the cathode of PEMFCs. The catalyst layer consists of catalyst and Nafion ionomer. Two functions of Nafion ionomer were identified: media for proton transfer and catalyst binder to maintain the shape of electrode.[93] For different catalyst materials, different optimal I/C values were obtained in multiple research groups for Pt based catalysts.[95,109,110] This is probably caused by the different carbon materials used and the MEA preparation conditions.

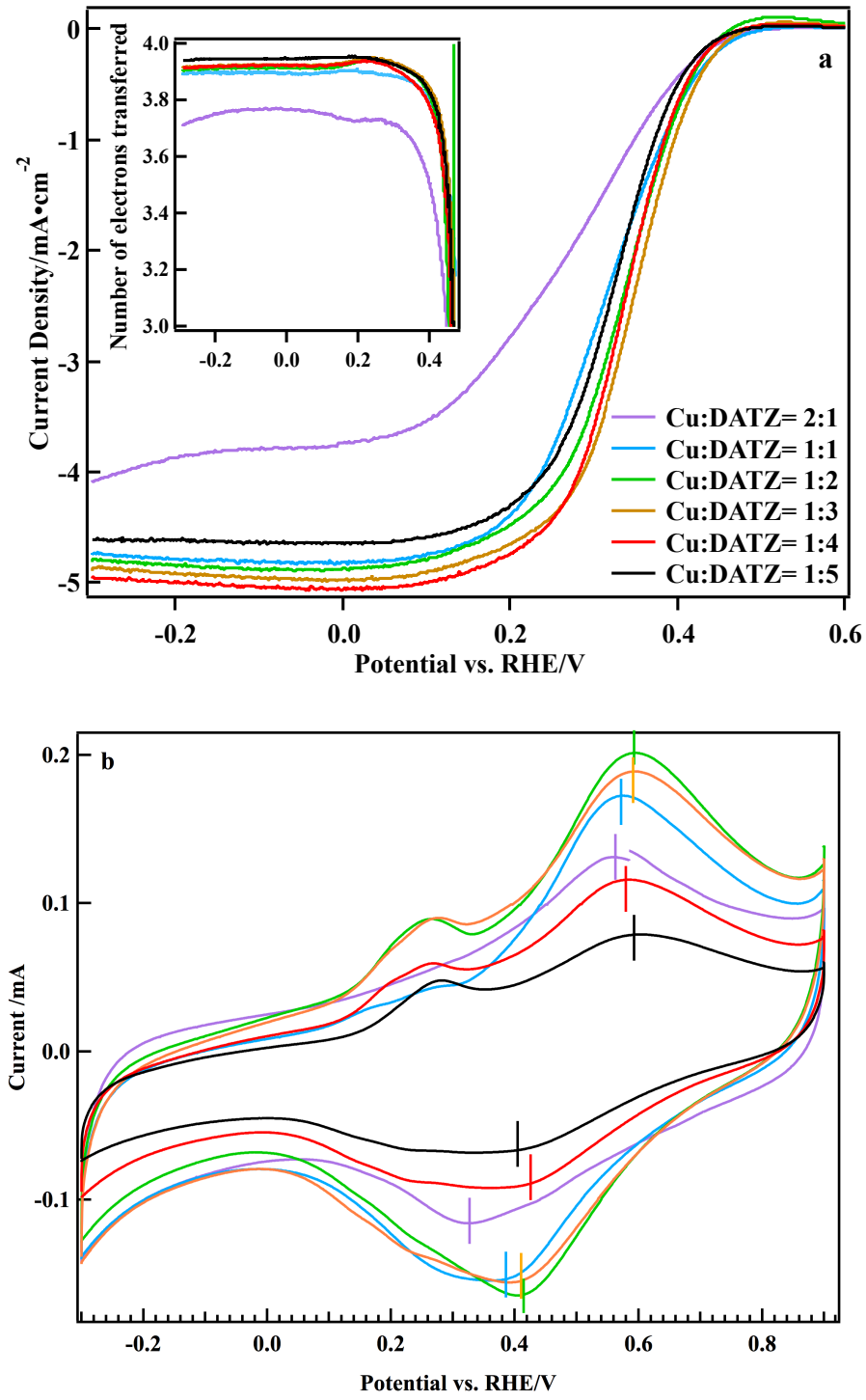


Figure 2.7 ORR cathodic curves, inset: number of electrons transferred, b. CVs of immobilized catalysts synthesized using Cu/DATZ ratio 2:1, 1:1, 1:2, 1:3, 1:4 and 1:5.

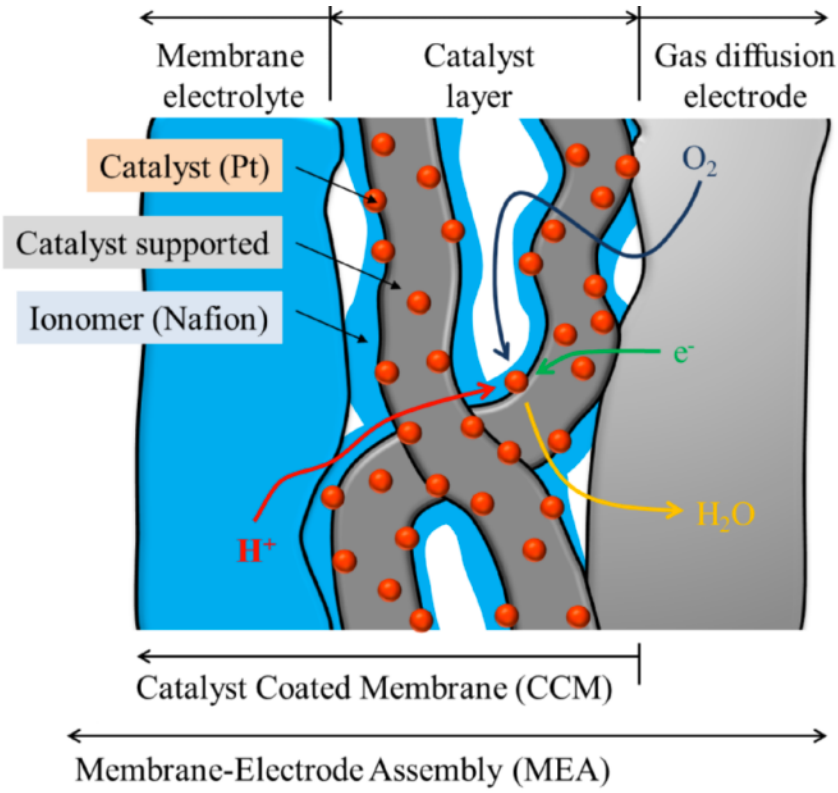


Figure 2.8 Schematic diagram of membrane –electrode assembly (MEA)[93] (copied from reference 93)

In order to obtain the optimal I/C ratio for electrochemical tests, the Nafion ionomer content in the mixture of ionomer and catalyst was varied from 20 to 40 %. The data is shown in Fig. 2.9. The mass transport in the catalyst layer deposited glassy carbon disk electrode is different from the situation in PEMFCs due to the lack of membrane electrolyte and gas diffusion electrode on both sides. The catalyst used is the immobilized Cu-DATZ complex with Cu/DATZ equal to 1:2. The ORR performance of the catalyst layer on the disk electrode is enhanced when the content of Nafion increases from 20 to 40%. This is probably more related to maintaining the shape of the catalyst layer on disk electrode rather than the increased proton conductivity of the ionomer since the disk electrode is immersed in an acid solution. Excessive Nafion in the catalyst layer impairs

the performance as shown in the RDE cathodic curve when Nafion content reaches 50%. After the optimal ratio is reached, excessive Nafion could block the active sites in the catalyst layer. The numbers of electrons transferred are lower when there is not enough (20%) or excessive Nafion (50%) in the catalyst layer. The increased production of H_2O_2 for both situations could be explained below. The scenario for not enough Nafion ionomer could be that part of the catalyst layer comes off the disk electrode, resulting in not having enough active sites to completely reduce O_2 into H_2O. Excessive Nafion ionomer could block the active sites and also leads to incomplete reduction of O_2, which is H_2O_2 production.

2.8 Dependence of ORR performance on different anions of Cu salts

Changing the counterions has been demonstrated to change the framework and molecular architecture of Cu(II) triazoles complexes.[92,111] This possibly results from changing the manner in which multiple copper ions are bridged within the complexes.[92] Anions, which can form an additional bridge between metal centers, have to be small enough to avoid a strong steric effect. Fig. 2.10 a and b shows ORR cathodic curves and CVs of a series of catalysts prepared with different copper salts, including $Cu(OAc)_2$, $CuSO_4$ $Cu(OTf)_2$, $Cu(ClO_4)_2$, $CuCl_2$, $Cu(NO_3)_2$ and $Cu(BF_4)_2$ to probe the effect of different anions on the catalyst performance.

All above anions except OTf^- have been observed in literature as bridges or co-ligands for metal centers.[42] H_2O is another molecule that is very likely to bridge or co-bind metal center in the solution. One example of bridging or co-ligand of anions and H_2O is shown in Fig. 2.11.

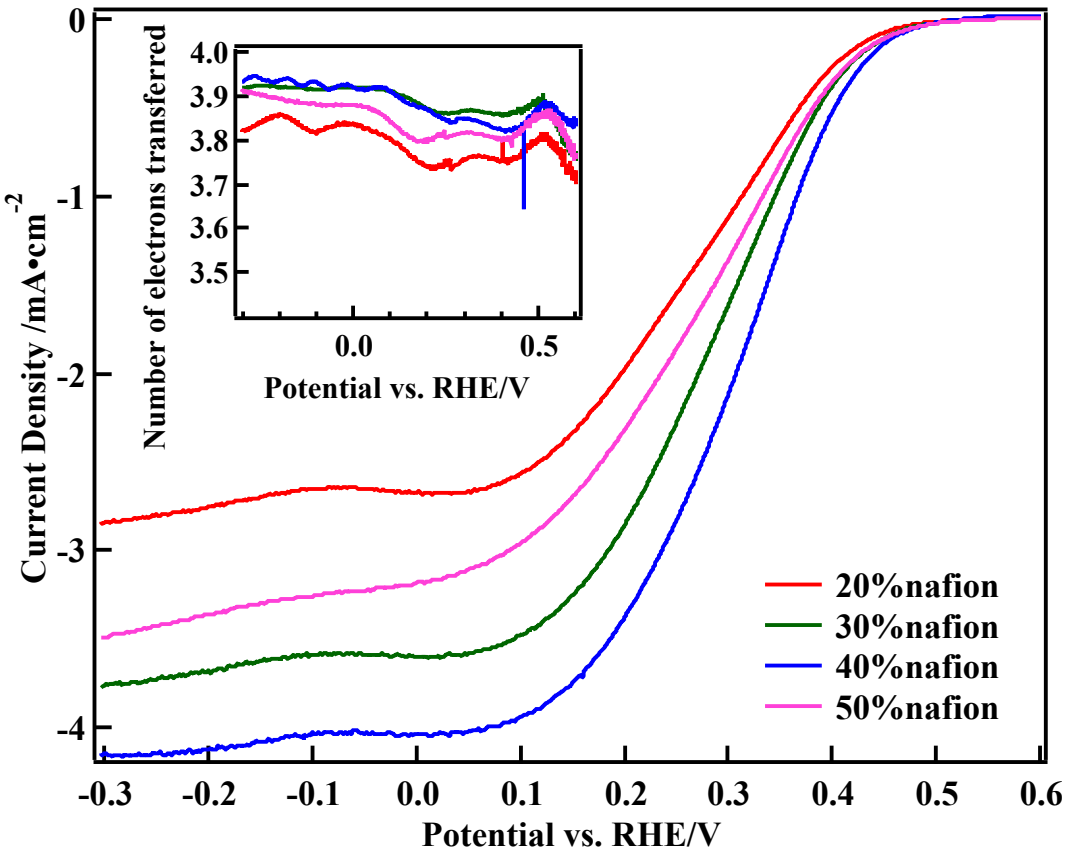


Figure 2.9 Variation of Nation ionomer content in the preparation of working electrode. The catalyst amount on the disk electrode was constant for each test in O_2 saturated electrolyte while the amounts of Nafion ionomer are 20, 30, 40 and 50, wt% of the catalyst and Nafion ionomer. inset: number of electrons transferred.

The catalyst with $Cu(OAc)_2$ exhibits the highest onset potential of this series, 0.522 V. The next highest activity is obtained with $CuSO_4$ (0.465V). Samples with $Cu(OTf)_2$ (0.473V), $Cu(ClO_4)_2$ (0.485V), $CuCl_2$ (0.487V) and $Cu(NO_3)_2$ (0.462V) show a similar activity but they are poorer activity than $CuSO_4$ when taking both half-wave potential and limiting current into consideration. The catalyst prepared with $Cu(BF_4)_2$ (0.438V) exhibits the lowest performance.

Figure 2.10 a. RDE cathodic curves of Cu(II)-DATZ-based catalysts synthesized using copper salts $Cu(OAc)_2$, $CuSO_4$ $Cu(OTf)_2$, $Cu(ClO_4)_2$, $CuCl_2$, $Cu(NO_3)_2$ and $Cu(BF_4)_2$ and oxidized BP2K, OTf = $CF_3SO_3^-$. b. CVs for these catalysts. c. Plot of logarithm of normalized kinetic current i_k/q vs. potential 0.4, 0.3, 0.2, 0.1V.

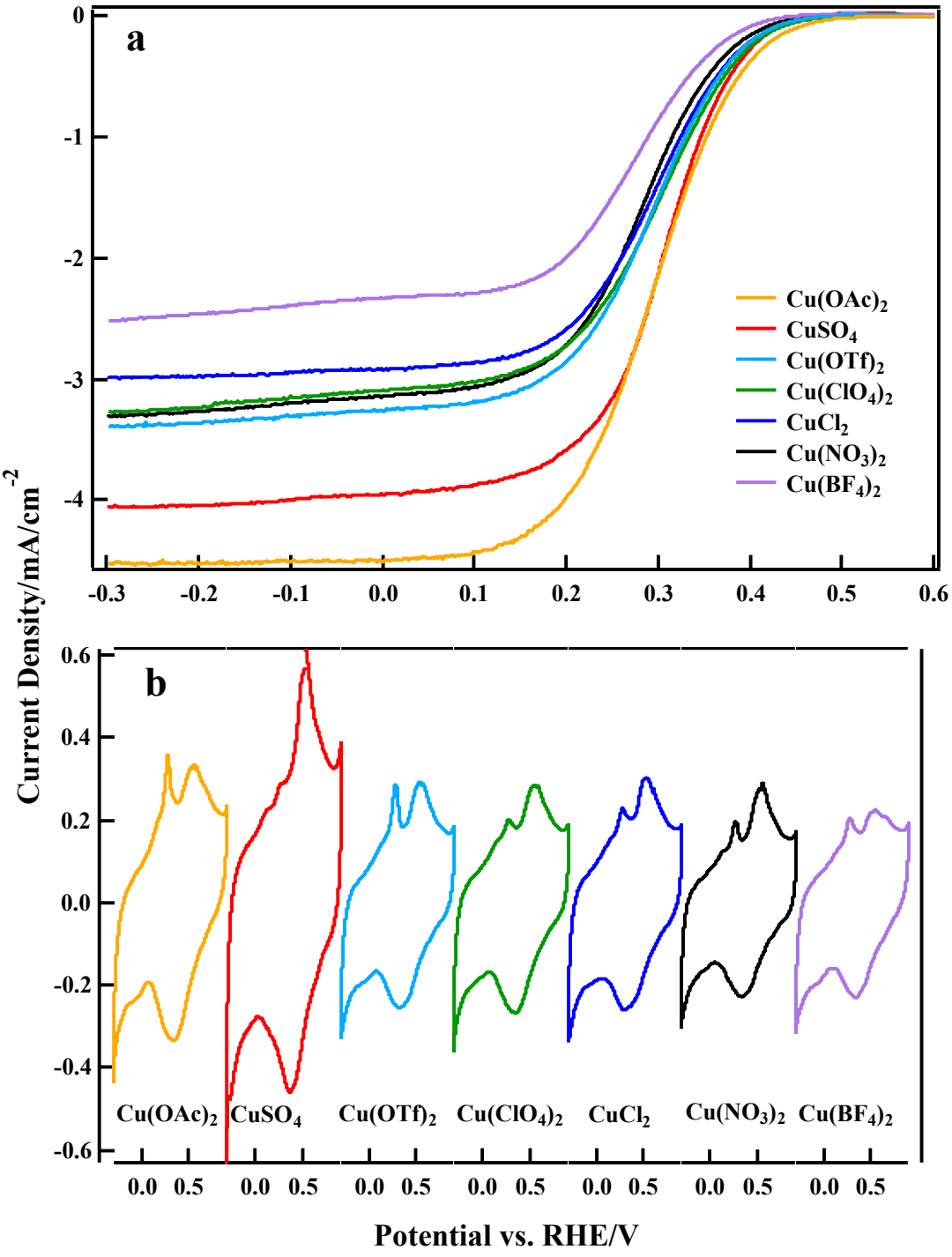


Figure 2.10 continued

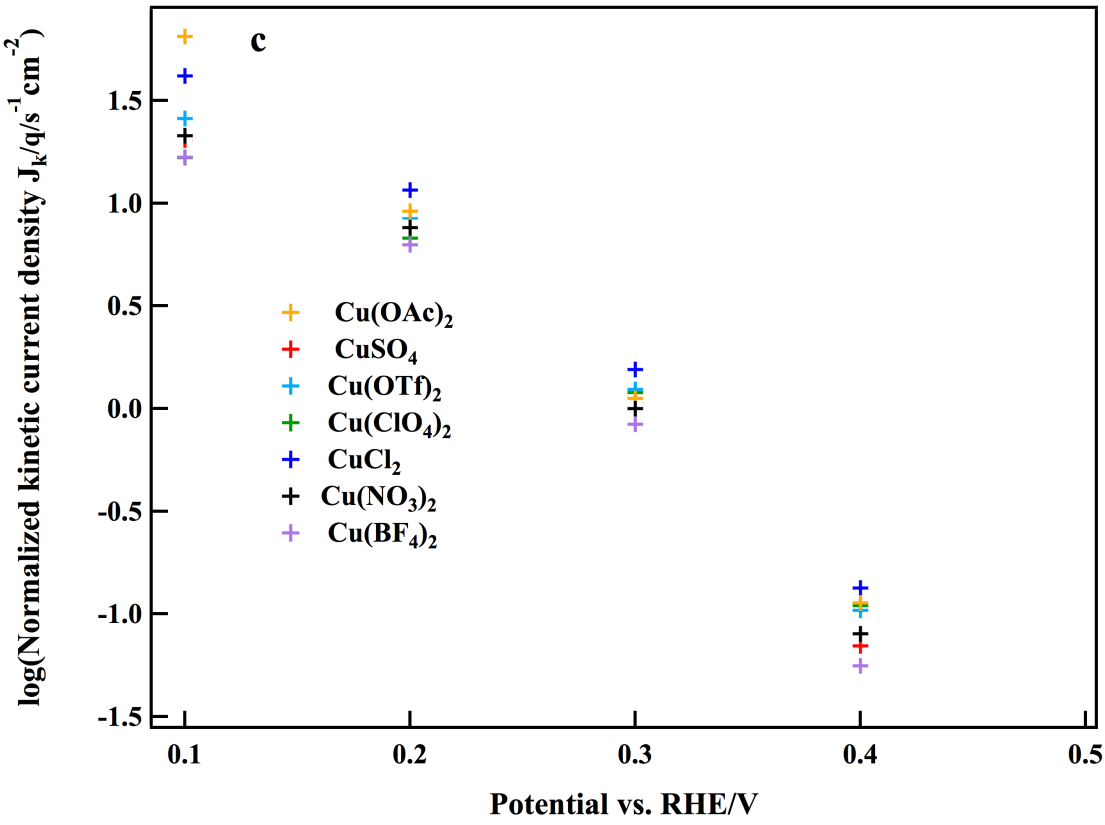


Figure 2.10 continued

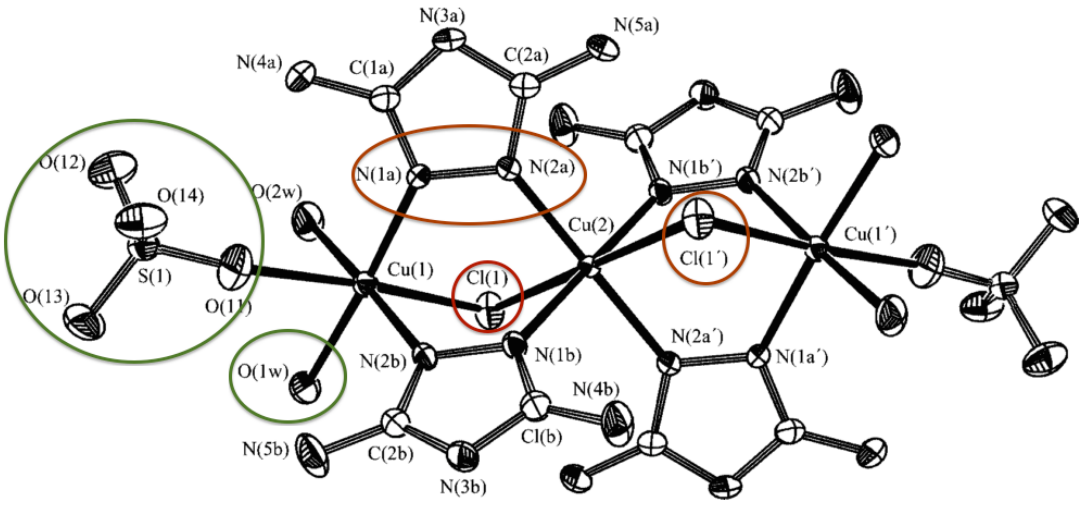


Figure 2.11 ORTEP (Oak Ridge Thermal-Ellipsoid Plot Program) of a Cu(II)-DATZ complex. H atoms have been omitted for clarity.[39] (copied from reference 39) Circles in red point out the bridge atoms between Cu centers. Circles in green indicate the co-ligand anion or molecule of the Cu centers.

Average potentials of the cathodic (0.38V) and anodic peak (0.52V) can be taken as a measure of redox potential of a redox couple. In Fig. 2.10b, the redox potentials of complexes in different catalysts are all around 0.4 V. The shapes of the CVs are identical. This suggests that anions behave as co-binder in the Cu-DATZ complexes. Their binding with Cu, possibly in the axial position such as SO_4^{2-} in Fig. 2.11, could cause steric effect to O_2 binding with Cu.

Fig. 2.10c plots the logarithm of normalized kinetic currents at potentials 0.4, 0.3, 0.2 and 0.1 V. Kinetic current density is calculated by Koutecky-Levich equation, which is equation (2.4):

$$\frac{1}{J} = \frac{1}{J_L} + \frac{1}{J_k} \qquad (2.4)$$

Where J is the measured current density, in mA/cm^2 and J_L is the limiting current density calculated from Levich equation, as shown in equation (2.2), in mA/cm^2. It can also be

approximately estimated from the current density at plateau region of RDE cathodic curves. J_K is the kinetic current density, in mA/cm^2

Normalized kinetic current density is obtained by dividing kinetic current density by the charge of reduction peak in the CV in the presence of N_2. It can be regarded as an indication of the electron transfer rate of the catalysts.[35] It is also called the turnover frequency for heterogeneous catalysts from the unit of Jk/q ($cm^{-2}s^{-1}$).[112,113] The sample with $CuCl_2$ shows the highest turnover frequency at potentials studied. The one with $Cu(BF_4)_2$ shows the lowest turnover frequency. Others fall in between. Tafel slope can be calculated from the slope of plot of logarithm of turnover frequency vs. potential. The Tafel slope for all copper salts at potential investigated is about 120 mV/decade, which is very close to the slope of a one electron transfer process derived from Butler Volmer equation with a transfer coefficient equal to 0.5. It strongly suggests that rate-determining step (RDS) in this potential range involves one electron transfer. The anions in copper salts could change the turnover frequency to some extent but not very much of the Tafel slope.

The fact that the catalyst with $Cu(OAc)_2$ shows a higher activity than $CuSO_4$ might indicate that complexes with OAc^- contribute more effective active sites for O_2 reduction than complexes with other anions explored. Solid state $Cu(OAc)_2 \bullet H_2O$ normally exists in dimer form due to bridged Cu(II) centers by OAc-. H_2O acts as co-ligand binding metal at the axial position.[114–116] This molecule exhibits a strong coupling interaction between the two unpaired electrons on each Cu from their EPR spectra.[114] The structure of this molecule in solid state is shown in Fig. 2.12.

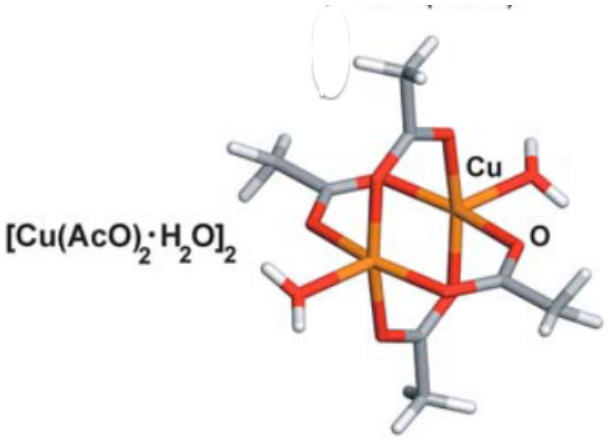


Figure 2.12 Dimer form of Cu(II) acetate monohydrate[116](copied from reference 116)

However, after dissolving in water, the $Cu(OAc)_2$ dimer breaks into two free Cu(II) due to the hydration of Cu^{2+} and OAc-.[115] The high performance of catalysts synthesized with OAc- might be related to strong bridging ability of OAc-. McCrory *et al.* have also confirmed the facilitation effect of OAc^- on ORR by adding NaOAc into the electrolyte to obtain an improvement of ORR activity based on their Cu(II)-phenanthroline complex-based electrocatalysts.[35] Clearly, further studies are necessary to know the structure of the complexes with OAc^-.

2.9 Summary

In this chapter, the synthesis conditions are optimized for Cu-DATZ complex-based electrocatalyst. The ORR performance of this catalyst was improved through functionalizing the carbon surface, varying the anions in copper salts and the Cu/DATZ ratio in the solution.

Optimal Nafion ionomer/catalyst ratio was also explored as 4/6 for Cu-DATZ immobilized catalyst. Introduction of oxidized functional groups could potentially change the polarity of the carbon surface and hence has an impact on the distribution or binding

mode of the complexes on the carbon surface since carbon surface could possibly act as a co-ligand in the axial position of a complex. Linking DATZ ligand on the carbon surface through chemical bond was an effective approach to enhance the stability of this catalyst. The reason for the decomposition of catalyst based on Cu-DATZ was briefly investigated by holding ring electrode at positive potential for Cu(I) and at negative potential for Cu(II) coming off the disk electrode. The unstable Cu(II) complex at potentials larger than 0.35 V is a possible reason for the decomposition of the catalyst while Cu(I) complex was stable during the CV scan in the presence of only N_2. The presence of the ligand DATZ dramatically enhances the binding of Cu(II) on the carbon surface. The optimal Cu/DATZ was found to be 1:2 and will be used for all the following catalyst synthesis. $Cu(OAc)_2$ was found to be the copper salt yielding the highest ORR performance among the copper salts investigated. Other researchers also observed the facilitation effect of OAc-. This might be related to the strong bridging ability of OAc- of Cu centers.

3 Mechanistic study of ORR by Cu(II)-DATZ based electrocatalysts

3.1 Introduction

The mechanistic aspects of the ORR have been extensively studied due to its application in PEMFCs. Mechanistic study of the ORR involves elucidating elementary steps comprising the ORR and determining reaction kinetics and intermediates involved in those steps. Among these elementary steps, the rate-determining step (RDS) is the most important step to understand the mechanism. Platinum-based electrocatalysts have been well studied since they are still the most utilized catalysts in the commercialization of PEMFCs so far. Both theoretical and experimental approaches developed for investigating ORR mechanism of platinum-based catalysts and non-pyrolyzed NPMC in acidic media will be briefly covered in this introduction. Discussion of mechanistic aspects of ORR includes exchange currents, Tafel slope, reaction orders of species involved in RDS and possible reaction intermediates. RRDE is the major experimental technique to provide experimental data to fit the model.

Damjanovic *et al.* carried out continuous work on the mechanistic aspects of ORR in acid and alkaline conditions from 1960s to 1990s.[3] In acid conditions, they obtained the following relationships from platinum-based electrocatalysts at low current densities:

$$\frac{\partial V}{\partial pH} = -\frac{3}{2} \times \frac{2.3RT}{F} \qquad (3.1)$$

$$\frac{\partial V}{\partial log P_{O_2}} = \frac{2.3RT}{F} \qquad (3.2)$$

$$\frac{\partial V}{\partial log i} = \frac{2.3RT}{F} \qquad (3.3)$$

V is the potential applied on the electrode. pH is the pH of the electrolyte, varying from 0 to 4 for the acid conditions investigated. R is the gas constant. T is the temperature of electrochemical measurements. P_{O2} is the partial pressure of O_2 above electrolyte. F is the faraday constant. i is the kinetic current. 2.3RT/F is a constant, 59.5 mV/decade. $\frac{\partial V}{\partial logi}$ is called the Tafel slope. From the above relationships, the kinetic current i was derived to have a dependence on O_2 and H^+ with reaction orders 1 and 1.5 respectively and described as equation below:

$$i = AP_{O_2}[C_{H^+}]^{3/2} \exp\left[-\frac{FV}{RT}\right] \qquad (3.4)$$

The exponents of P_{O2} and C_{H+} are calculated by dividing equation (3.2) and equation (3.1) over equation (3.3) respectively. Relationships $\frac{\partial logi}{\partial logP_{O_2}} = 1 \; and \; \frac{\partial logi}{\partial pH} = -1$ are obtained to derive the exponents of P_{O2} and C_{H+}.

At high current densities, with the following relationships:

$$\frac{\partial V}{\partial pH} = -2 \times \frac{2.3RT}{F} \qquad (3.5)$$

$$\frac{\partial V}{\partial logP_{O_2}} = 2 \times \frac{2.3RT}{F} \qquad (3.6)$$

$$\frac{\partial V}{\partial logi} = 2 \times \frac{2.3RT}{F} \qquad (3.7)$$

kinetic current i was described as equation (3.8):

$$i = AP_{O_2}[C_{H^+}] \exp\left[-\frac{FV}{2RT}\right] \qquad (3.8)$$

The exponents for P_{O2} and C_{H+} are calculated by taking equation (3.6) and (3.5) over equation (3.7) respectively. Then relationships $\frac{\partial logi}{\partial logP_{O_2}} = 1 \; and \; \frac{\partial logi}{\partial pH} = -1$ are obtained to derive the exponents of P_{O2} and C_{H+} are both 1.

The RDS was proposed as follows:

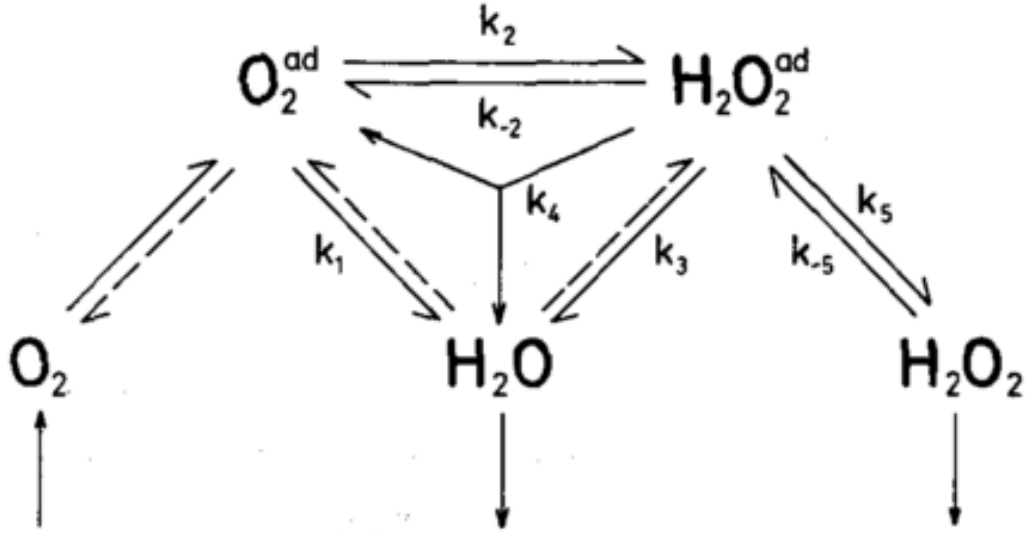
$$S \ldots O_2 + H^+ + e^- \rightarrow product(s) \qquad (3.9)$$

S is the available active sites on an electrode surface. S…O_2 indicates O_2 molecule is adsorbed at the active site.

There is a transition of Tafel slope from 60 mV/decade to 120 mV/decade when the potential goes from low overpotential to high overpotential region. The reaction order of H^+ changes from 1.5 to 1 over this potential regime. This were explained by different oxide coverage on the electrode in different potential regions.[117] To explain the Tafel slope transition and fractional H^+ reaction order, surface coverage was proposed to have a dependence on the pH of the electrolyte and the potential. An expression of surface coverage dependent on pH and potential was successfully developed. This dependence was suggested to be caused by the domination of Temkin or Langmuir adsorption of reaction intermediates or oxygen species adsorbed on platinum at different potential range.[118] Their work is internally consistent and established compared to other researchers' work. The approach is useful to derive the RDS. However, It is limited in its suitability to provide information about other fast elementary steps.

Another approach to probe the ORR mechanism is giving the scheme of the ORR, developing kinetic equations with the knowledge of chemical kinetics, and then calculating kinetic parameters by comparing the derived expression with experimental measurements. RRDE has been the major technique to probe the mechanism and has been applied to distinguish the series mechanism or/and parallel mechanism. Different models have been explored from simplified to more general ones elsewhere for platinum

based catalysts.[119–122] This approach was also employed on metal chelates by Behret *et al.*[123,124] In their work, the O_2 reduction scheme by metal chelates in acid was given:



Scheme 3.1 Reaction scheme for electrochemical oxygen reduction. (copied from reference 49)

The following equations were developed from above scheme.

$$\frac{I_{disk}}{I_{ring}}N_0 = 1 + 2\frac{k_1}{k_2} + \left[\left(1 + 2\frac{k_1}{k_2}\right)(k_{-2} + k_3 + k_4) + k_3 - k_{-2}\right]\frac{1}{\gamma_{H_2O_2}\sqrt{\omega}} \qquad (3.10)$$

$$\frac{I_{lim} - I_{disk}}{I_{ring}}N_0 = 1 + 2\frac{k_{-2} + k_3 + k_4}{k_2} + \frac{2\gamma_{O_2}\sqrt{\omega}}{k_2} \qquad (3.11)$$

I_{disk} and I_{ring} are the currents measured from disk and ring electrode respectively. k_ns' are the reaction constants for reactions in scheme 3.1. γ_{O_2} is a constant related to diffusion coefficient and kinematic viscosity of O_2 and H_2O_2 in the electrolyte. N_0 is the collection coefficient of the ring electrode. ω is the rotation rate of the disk electrode.

By plotting $\frac{I_{disk}}{I_{ring}}N_0$ vs. $\omega^{-1/2}$ from equation (3.10), the intercepts of the straight lines give information about the ratio $\frac{k_1}{k_2}$. The rate constant k_2 can be evaluated by plotting

$\frac{I_{lim}-I_{disk}}{I_{ring}}N_0$ vs. $\omega^{1/2}$. Still it is not possible to calculate each of other parameters.[123] This methodology is similar to those developed for platinum based catalysts. It does not consider the possible metal redox behavior during ORR catalysis. However, the latter could be possible for transition metal-based electrocatalysts, such as Fe, Co.

Based on the above discussion about the advantages and disadvantages of the two major methods, the first method will be employed to develop the expression of RDS in our case. The Tafel slope and reaction orders of possible species involved in RDS were evaluated from RRDE results. A possible mechanism for ORR catalyzed by Cu(II)-DATZ-based catalyst is proposed and discussed.

3.2 Experimental Procedures

3.2.1 Chemicals

Chemicals are the same as those in section 2.2. The electrolyte is 0.1 M $NaClO_4$. Britton-Robinson buffer is used to control the pH of the electrolyte. Different pHs were obtained by using solid NaOH and a pH meter. The composition of Britton-Robinson buffer is CH_3COOH, H_3PO_3 and H_3BO_3, each at 0.04 M. H_2O_2 (30%) was purchased from Fisher Scientific.

3.2.2 Different Oxygen concentration experiment

Different Oxygen concentrations in the electrolyte were achieved by mixing pure N_2 and O_2 gas stream at different volume flow rate using two gas flow controllers. The volume percentages are 0%, 20%, 40%, 60%, 80%, and 100% for O_2. The experiments were conducted in an order of increasing O_2 concentrations in the purging gas. CVs and RRDE experiment were run for each concentration. Catalyst on the disk electrode was

renewed by adding the same volume of catalyst for each O_2 concentration experiment. This avoids the effect of possible catalyst decomposition.

3.2.3 Different catalyst loadings on the disk electrode

Catalyst ink was prepared as described in section 2.2.5. Different volumes of ink were deposited on the disk electrode to achieve different loadings. Each mass loading was measured by weighing the difference of a piece of dry filter paper before and after adding the same volume of catalyst ink. The catalyst loadings examined are 240, 530, 800 and 1070 μg/cm^2.

3.2.4 Addition of H_2O_2 in the electrolyte

The added H_2O_2 in the electrolyte is about 1.5 mM. This concentration is comparable to the concentration of O_2 in the electrolyte. Regular CV and RDE experiments were run without and with H_2O_2 in the electrolyte.

3.2.5 Dependence of ORR on the pH of the electrolyte

Different pH values of the electrolytes were adjusted by adding NaOH solid into Britton-Robinson buffer and monitored by a pH meter. The reference electrode is Ag/AgCl electrode with a double junction. The potential of the reference electrode is independent of the pH of the electrolyte. pH values investigated are 2, 4, 7, 10, 13.

3.3 Dependence of ORR activity on O_2 concentrations in the electrolyte

To determine the reaction order of O_2, an experiment is designed to measure RDE cathodic curves for the ORR at different oxygen concentrations (20, 40, 60, 80 and 100%, volume percentage; the other gas is pure nitrogen) for Cu(II)-DATZ immobilized catalyst. Results of this experiment is shown in Fig. 3.1. Equation (3.12) enables determination of

the reaction order of O_2. The value of the kinetic current density J_k is calculated from equation (2.1). J_L is known from the Levich equation. The n values have been varied from 3 to 4 to calculate the limiting current, the difference in the results of reaction order of O_2 is negligible. Therefore the n value is assumed to be 3.5 at all potentials to calculate limiting current. J values are read from the cathodic curves for each potential. We choose potentials in the kinetic current region from 0.20 V to 0.40 V. J_k can be written as a function of the concentration and reaction order as following based on the knowledge of chemical kinetics:

$$J_k = nFkc_{O2}^m c_{Cu(I)}^p c_{H^+}^q \qquad (3.12)$$

Where n is the number of electrons, F is the Faraday constant, k is the reaction rate constant, c_{O2} and c_{H+} are the bulk concentration of O_2 species and H^+ in the electrolyte respectively. $c_{Cu(I)}$ is the Cu(I) amount in the catalyst. *m, p and q* are the reaction order of O_2, Cu(I) and H^+ respectively. By taking the logarithm on both sides of equation (3.12):

$$logJ_k = \log(nFk) + mlogc_{O2} + plogc_{Cu(I)} + qlogc_{H^+} \qquad (3.13)$$

Plots of logJ_k vs. logc_{O2} are shown in the inset of Fig. 3.1b. The slope of each of these plots corresponds to the reaction order m. In this case, m is about 1 for each of the measured potentials, indicating that O_2 is involved in the RDS in its molecular form in the potential region investigated.

Fig. 3.1c shows the Tafel plots at different O_2 concentrations over the potential region 0.4~0.15V, which is about 130 mV/decade, indicating a single electron transfer mechanism at the potential investigated for this catalyst. This Tafel slope also suggests that Cu-DATZ based electrocatalyst has slow kinetics in catalyzing ORR.

Figure 3.1 a. RDE cathodic curves of Cu(II)-DATZ-based catalyst at O_2 partial pressure 20, 40, 60, 80 and 100% in the purging gas. Inset: number of electrons transferred n. b. Zoom-in picture of kinetic region between 0.2V to 0.4 V. inset: plot of $\log J_k$ vs. $\log c_{O2}$ at potentials 0.20, 0.25, 0.30, 0.35 and 0.40 V and values of reaction order m at these potentials. c. Tafel slope plot at potential region 0.4~0.15 V at different O_2 concentrations.

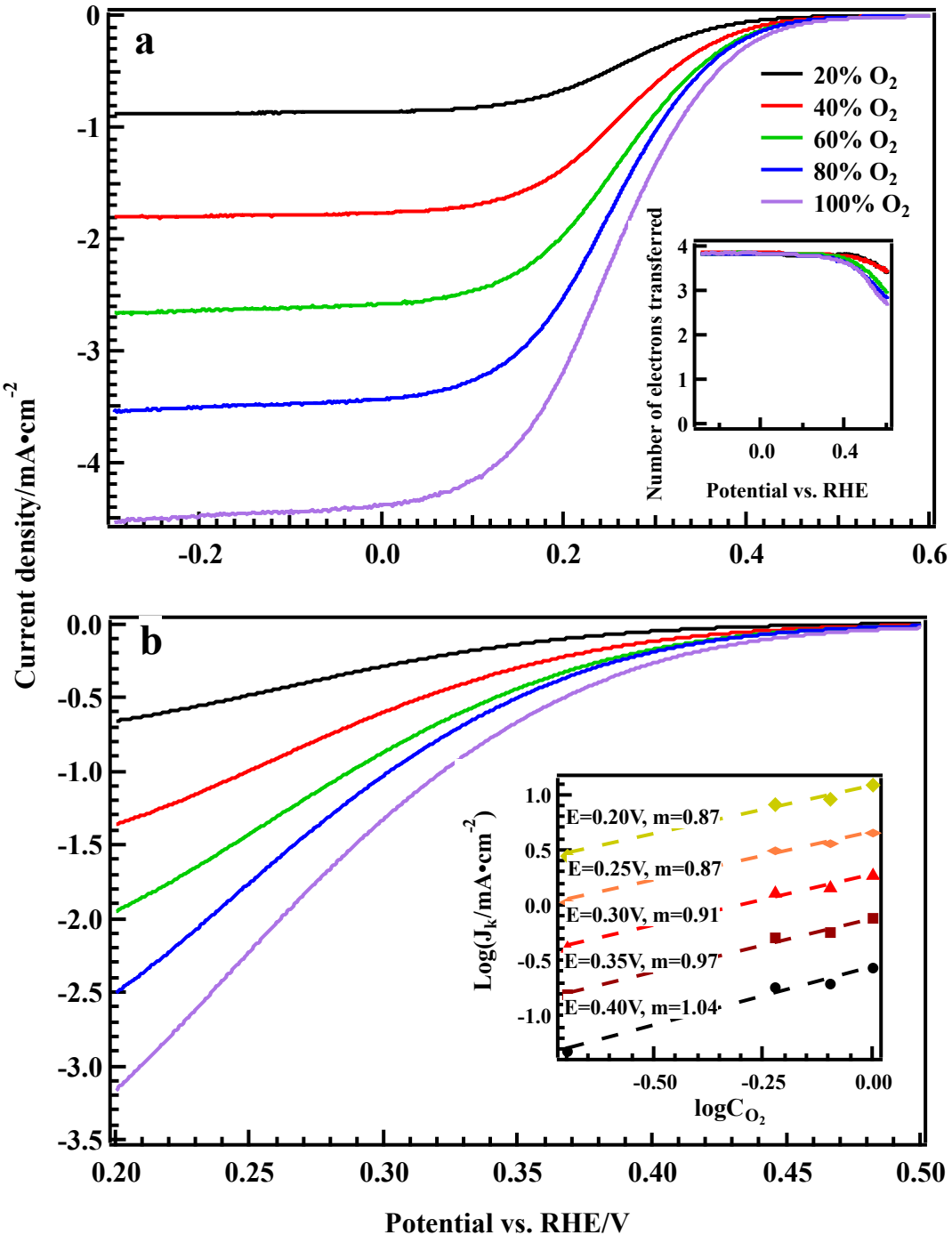


Figure 3.1 continued

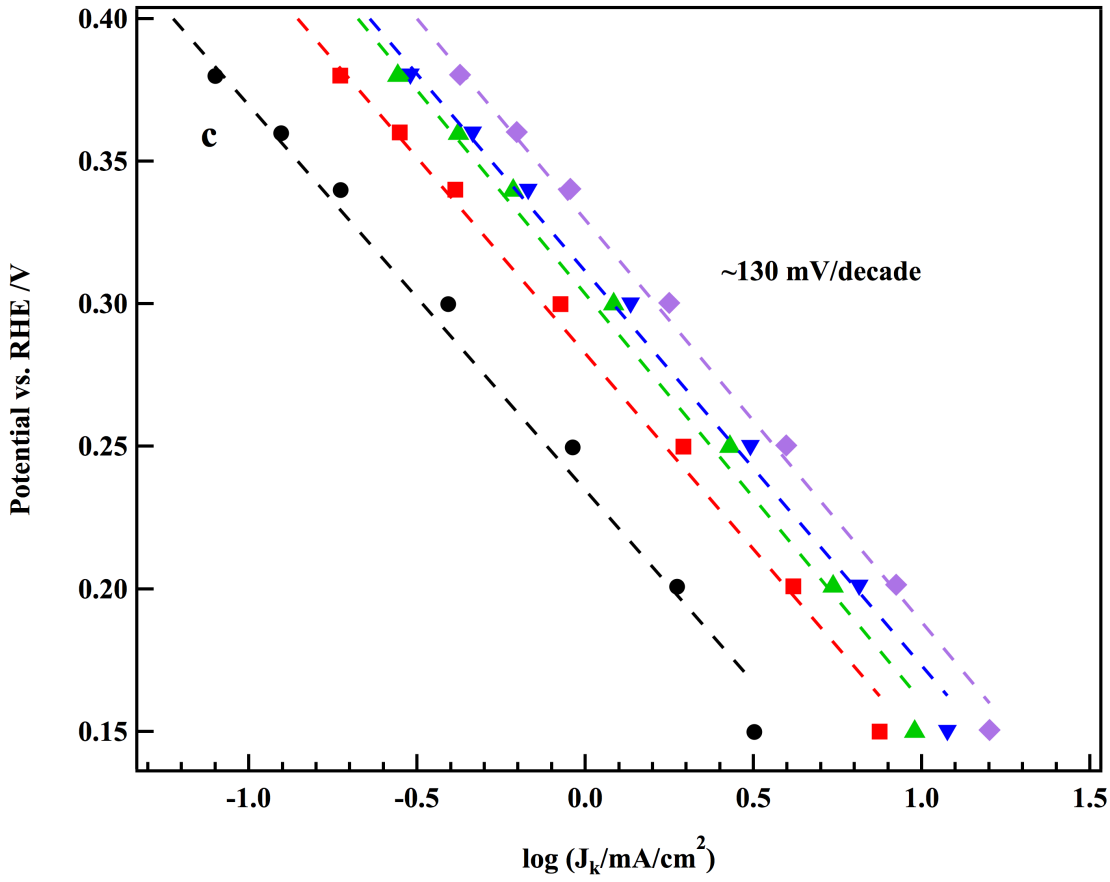


Figure 3.1 continued

Platinum based catalysts demonstrated around 60 mV at low current density region and about 120 mV at high current density region in both acid and alkine solutions.[117,118,125,126] Some high performance pyrolyzed Fe based catalysts showed a single Tafel slope of 60 mV at the kinetic potential region in acid.[127] The n values are shown in the inset of Fig. 3.1a and all are above 3.7 at potentials lower than 0.4 V. This suggests that more than 85% of the O_2 is reduced to H_2O by the Cu-DATZ-based catalyst in this potential region. The potential region lower than 0.15 V cannot be used to conduct kinetic analysis due to the effect of mass transport.

3.4 Dependence of ORR performance on catalyst loadings

The experiment of varying catalyst loading on disk electrode has been done to differentiate the direct 4e- and 2 × 2e reaction mechanism of ORR for non precious metal catalysts.[127–129] As shown in Fig. 3.2, the catalyst loading on the disk electrode increases, the capacitance of the catalyst, ORR onset potential and half wave potential. The larger capacitance and redox peaks indicate more active sites are present in the catalyst as loading increases. The number of electrons transferred n increases from 3.4 to 3.9 as the loading increases from 240 to 1070 μg/cm^2, indicating continuously less production of H_2O_2 with higher loadings. This scenario can be explained that H_2O_2 formed on the electrode surface can either experience a following reduction or be desorbed from the electrode. As catalyst loading increases, tortuosity reduces the possibility that H_2O_2 travels outside of the catalyst layer. This observation provides support for the 2 × 2e- ORR mechanism, in which O_2 is reduced to H_2O with H_2O_2 as an intermediate, in a modest percent of reaction. This agrees with other results from the loading dependence studies of iron based catalysts.[127,128]

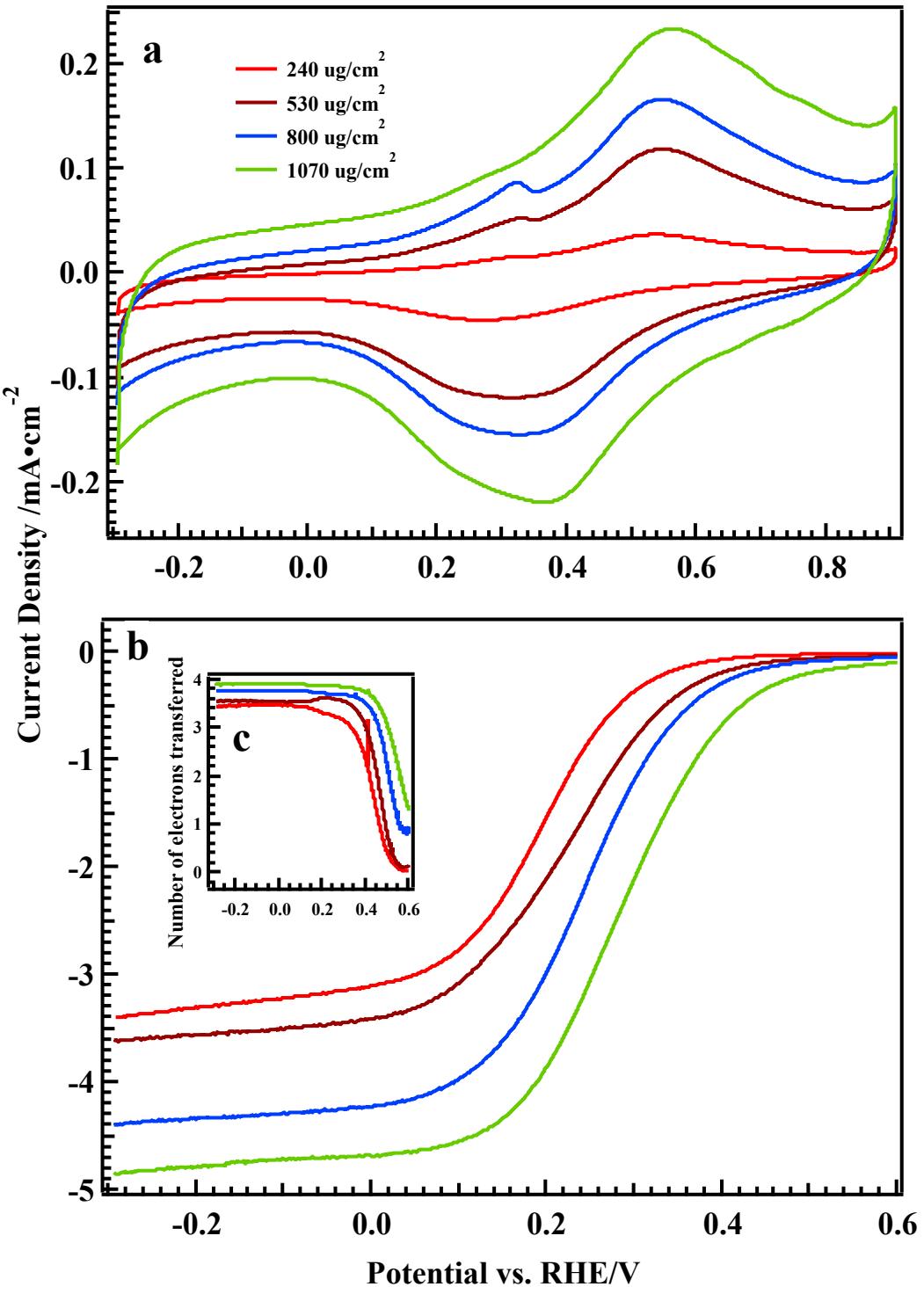


Figure 3.2 a. CVs in N_2 saturated electrolyte. b. RDE cathodic curves in O_2 saturated electrolyte. c. number of electrons transferred at different catalyst loadings, 240, 530, 800 and 1070 μg/cm^2 on the disk electrode. The scan rate is 10 mV/s.

3.5 Reaction order of Cu species of Cu(II)-DATZ-based catalyst in ORR

To calculate the reaction order of Cu(I), the amount of Cu(I) during ORR was estimated by integrating the charge of the reduction peak of Cu(II)/Cu(I) redox couple in pure N_2 saturated electrolyte after subtracting charge from capacitance current. As the potential scan goes toward negative values, more Cu(I) is produced. The integral was calculated over the range from the onset potential of Cu(II) reduction to the potential investigated. In our case, it is from 0.4~0.26 V. McCrory *et al.* have integrated the whole reduction peak as a measure of Cu(I) in the catalyst but only chose kinetic current at one potential to calculate the reaction order of Cu(I) in ORR.[130] This method ignores the fact that the actual amount of Cu(I) catalyzing O_2 changes with potentials. The inset of Fig. 3.3 shows that the Tafel slopes at all loading at potential region 0.4~0.2 V are about 120 mV/decade. This value is very close to the value 118 mV/decade derived from Bulter-Volmer model for one electron transfer process with transfer coefficient equal to 0.5. The Cu(I) reaction order is calculated to be 2 for all loadings in the potential region 0.4~0.26 V, as shown in Fig. 3.3, indicating a di-nuclear catalytic center for O_2 binding for this catalyst. Binuclear Cu(I) acting as active sites catalyzing O_2 has also been proposed and confirmed through both experimental and theoretical investigation by McCrory *et al*.[130]

3.6 Addition of H_2O_2 in the electrolyte

Zhang *et al*. investigated the electroreduction of O_2 and H_2O_2 of Cu(II)-4,7-diphenyl-1,10-phenthrolinedisulfonate adsorbed on graphite electrodes and concluded that H_2O_2 cannot be an intermediate in the reduction of O_2 based on the observation that the catalyst catalyzes O_2 at a significantly greater rate than it catalyzes H_2O_2.[106]

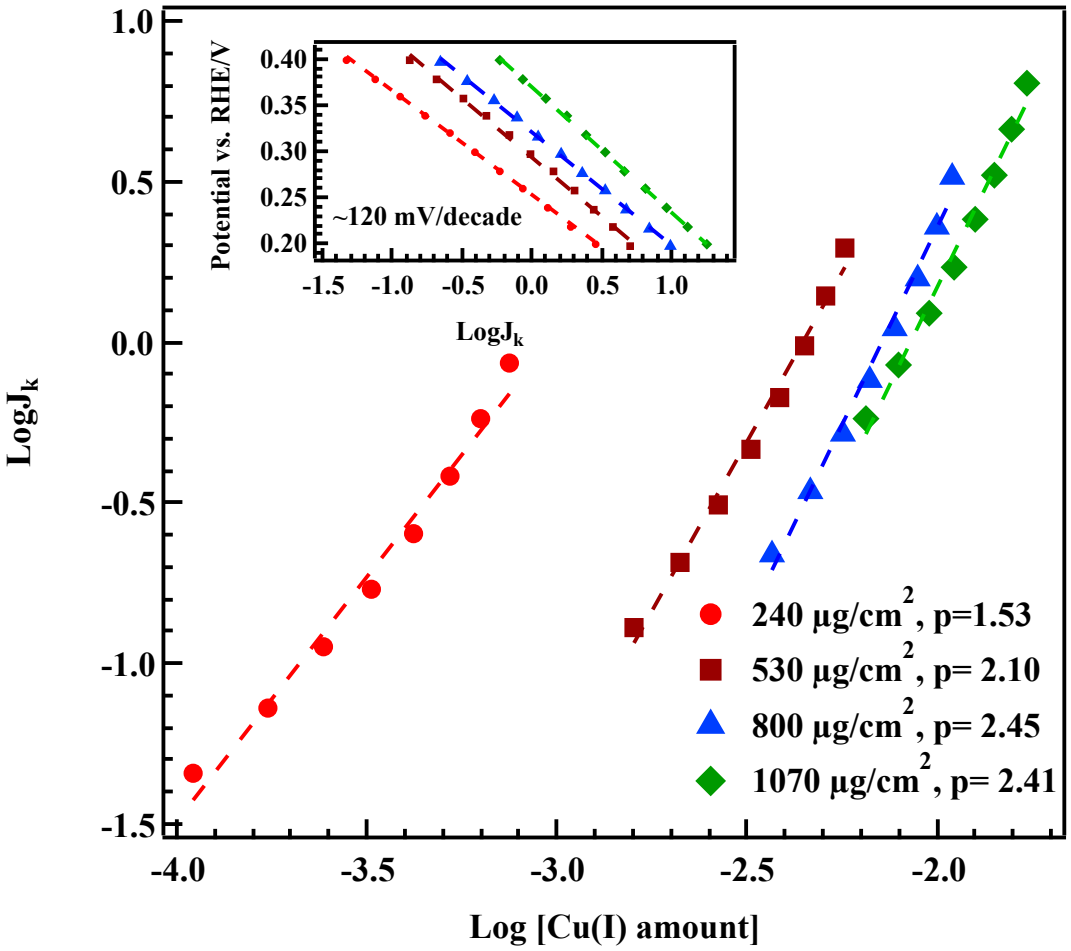


Figure 3.3 Plot of logrithm of kinetic current vs. logrithm of Cu(I) amount at potential region 0.4~0.26 V for each catalyst loading on the disk electrode. The potential inteval between points is 0.02V. Cu(I) amount is calculated by integrating the charge from the onset potential of Cu(I) to the potential where data poinits are taken. Inset: Tafel slopes for each catalyst loading at potential region 0.4~0.2 V.

Our catalyst loading studies reported above concluded that Cu-DATZ based catalyst catalyzes ORR through a 2 × 2e- mechanism. To ascertain that H_2O_2 is an intermediate during ORR by a Cu-DATZ-based catalyst, H_2O_2 was added to the electrolyte to see its effect on ORR. The estimated concentration of H_2O_2 is about 1.5mM in the electrolyte. Fig. 3.4 shows that the onset potential of reduction decreases in an order: $H_2O_2 > O_2 > H_2O_2$ with O_2 in 0.1 M H_2SO_4. Addition of H_2O_2 not only improves the onset potential of

O_2 reduction but also increases the limiting current of ORR. In the CVs, as shown in Fig. 3.4a, the onset potential of O_2 with H_2O_2 falls between the onset potential of O_2 with H_2O_2 and O_2, rather than showing two peaks in the scan. A similar result was observed even using a scan rate 1 mV/s: two separate peaks for H_2O_2 and O_2 were not observed during the cathodic scan. This indicates that H_2O_2 is an intermediate during ORR and its presence has an impact on the progress of ORR by shifting the onset potential of O_2 to more positive potential.

3.7 Dependence of ORR performance on pH values of electrolytes

The formal potential of Fe(III)/Fe(II) has been observed to have a dependence on pH of about 47 mV per pH for iron fluoroporphyrin adsorbed on a graphite electrode. A half reaction involving one electron and one proton was proposed to explain this slope.[105] To analyze the behavior of our catalyst at different pH values, a Robinson-Britton buffer (pH 2 to 13) was prepared to measure the ORR performance for the adsorbed catalyst based on Cu-DATZ complexes. The onset potentials for ORR at different pHs were fit by a linear line with a slope of 30mV/pH of the electrolyte (Fig. 3.5 inset). This suggests that at the beginning of ORR, the half reaction might involve two electrons and one proton. At pH lower than 13, the RDE cathodic curve shifts in parallel toward positive potential with similar limiting current. At pH 13, the limiting current decreases dramatically. This indicates that at pH lower than 13, the mechanism of catalyzing ORR might be the same, while at pH 13 or higher, the catalyst was partially broken down due to the strong base in the electrolyte.

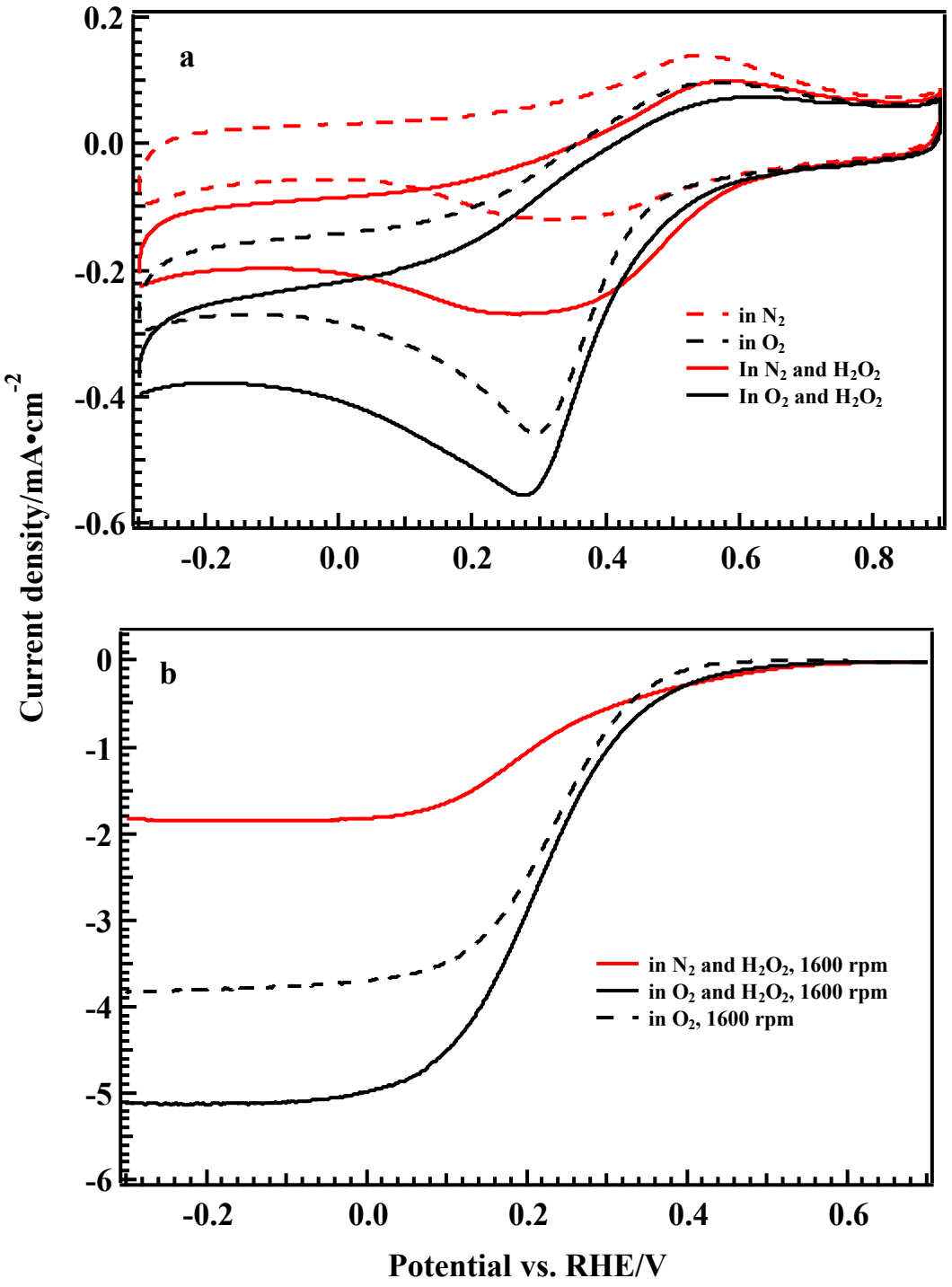


Figure 3.4 a. CVs of Cu-DATZ based catalyst in the presence of N_2, O_2, N_2 and H_2O_2, O_2 and H_2O_2 in the electrolyte. b. RDE cathodic curves of Cu-DATZ based catalyst in the presence of N_2 and H_2O_2, O_2 and H_2O_2, O_2 in the electrolyte.

Thorum *et al.* did similar experiments and suggested that the RDS involves two electrons transfer per H^+. The two electrons transferred could possibly be the reduction of two Cu(II) centers or the reduction of O_2 to a hydroperoxo (HOO-) intermediate.[32] In the following proposed ORR mechanism, this two electron transfer is attributed to the reduction of two Cu(II) centers.

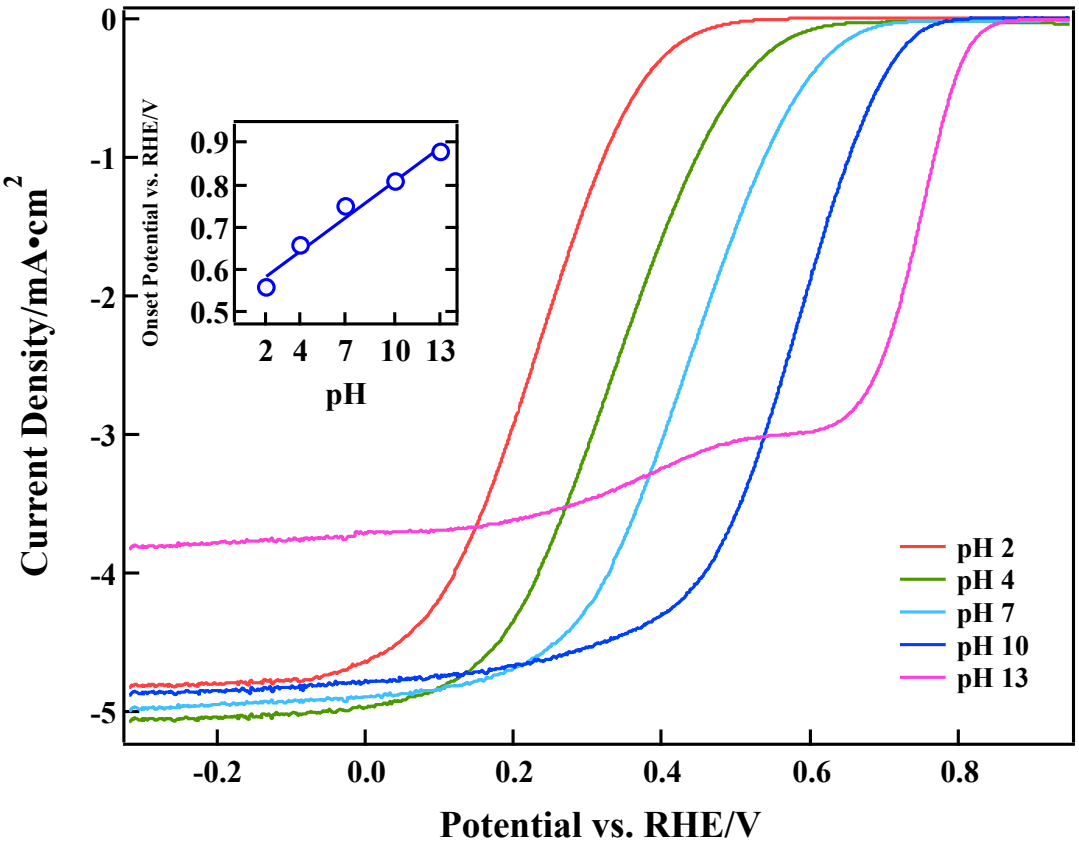


Figure 3.5 ORR cathodic curves at different pH values. The inset shows a linear fit with a slope of 30mV per pH.

3.8 Proposed ORR mechanism for Cu-DATZ-based catalyst

Here we summarize the previous kinetic results:

$$\frac{\partial V}{\partial pH} = \frac{1}{2} \times \frac{2.3RT}{F} \qquad (3.14)$$

$$\frac{\partial V}{\partial logi} = -2 \times \frac{2.3RT}{F} \qquad (3.15)$$

$$\frac{\partial logi}{\partial log c_{O_2}} = 1 \qquad (3.16)$$

$$\frac{\partial logi}{\partial log c_{Cu(I)}} = 2 \qquad (3.17)$$

The relationship of kinetic current i and c_{H^+} can be derived from equation (3.14) and (3.15):

$$\frac{\partial logi}{\partial log c_{H^+}} = \frac{1}{4} \qquad (3.18)$$

One assumption of equation (3.18) is that the concentrations of other species (O_2, Cu(I)) involved in the RDS are constant with changing pH. For Cu(I) species in the catalyst, this assumption is difficult to accept under pH range investigated because precipitation of Cu(II) and Cu(I) occurs at higher pHs. This is possibly why the reaction order of H^+ is fractional. A narrow pH range could be focused on to make sure there is no significant change in the Cu(I) species in the catalyst.

The ORR mechanism for Cu-DATZ-based catalyst in acidic medium was proposed from reaction (3.19-3.22) based on above evidence.

$$2Cu(II) + 2e^- \rightarrow 2Cu(I) \qquad (3.19)$$

$$2Cu(I) + O_2 + H^+ \rightarrow Cu(I)_2O_2H \qquad (3.20)$$

$$Cu(I)_2O_2H + H^+ + 2e^- \rightarrow H_2O_2 + 2Cu(I) \qquad (3.21)$$

$$H_2O_2 + 2H^+ + 2e^- \rightarrow 2H_2O \qquad (3.22)$$

During the cathodic scan of ORR, there are actually two reactions going on at the same time: Cu(II) reduction and ORR. The net reactions from proposed mechanism include these two processes. In the anodic scan of ORR, reaction (3.19) should be that Cu(I) is oxidized to Cu(II). The RDS is described in reaction (3.20). The other three reactions are fast steps. The reaction (3.19) occurs before O_2 reduction since the onset potential of Cu(II) reduction is more positive than that of ORR, strongly suggesting that the Cu(II) reduction is a step before ORR. Previous studies ignored that fact the oxidized and reduced forms coexist during ORR catalysis and mostly focused on the metal of the oxidized form binding oxygen.[34,35] The RDS includes two Cu(I) and one O_2 based on the measurement of reaction order of Cu(I) and O_2, and Tafel slope which are 2 and 1 respectively. The two Cu(I) could exist as a dinuclear complex or be located in close proximity. The measurement of distance between Cu(I) could be realized by *in situ* EPR, or XAS techniques. In the study of dioxygen reduction by cytochrome oxidase (CcO), the binding of dioxygen always requires a substantial transfer of electron density on to the bound O_2.[131] Consequently, only the Fe(II) and Cu(I) bind O_2. The oxidized form existing in the enzyme does not bind O_2. This agrees with the conclusion obtained from Cu-DATZ-based catalyst. The bonding mode of 2Cu(I)—O_2 was depicted in Fig. 1.6 with the d_{z2} orbitals of two Cu(I) as electron donor and antibonding π^* orbital on the O_2 as electron acceptor. Their orbital symmetry matches well to form chemical bonds. The number of H^+ involved in RDS can not be calculated based on the pH dependence experiment since pH change also has an impact on the form of Cu(II) and Cu(I) in the catalyst. Though we try to calculate it, the result (1/4) is fractional and this agrees with

the explanation above. The intermediate $Cu(I)_2O_2^-$ involved in reaction (3.20) is a superoxide with the electron in Cu(I) partially transferred to O_2 molecule. This species tends to be protonated in strong acid condition. Reaction (3.21) is proposed since electrons in Cu(I) in the last step were transferred to O_2 while at this potential Cu(II) should be easily reduced to Cu(I). The electron transfer is from Cu(I) to O_2 molecule and then Cu(II) is getting another electron to form Cu(I). In this way, the amount of Cu(I) is maintained at a steady state for certain potentials. The reactions after the RDS are fast steps and show the reduction of H_2O_2 because the catalyst shows better activity in reducing peroxide.

4 ORR catalysis by Cu with different substituted triazole-based electrocatalysts

4.1 Introduction

Changing the substituents in the ligand composing the metal chelates is an effective approach to vary the electronic properties of the complexes and hence the electronic properties of the catalysts. The electronic properties of the complex are reflected in the redox potential, energy gap of the bonding orbitals and electron densities in metal.[35,132] As summarized in section 1.5, different research groups obtained different conclusions on the facilitation/inhibition impact of electron donating/withdrawing capacity. Baker *et al.* investigated the ORR reactivity and stability of iron phthalocyanines with substituents ranging from electron withdrawing to electron donating groups. However, they found unexpectedly that the non-substituted complex demonstrated the highest ORR performance.[133] One possible reason for that is the increased diversity of complexes after introduction of functional groups. This could change the coordination geometry of the complexes resulting in fundamentally altering the catalysts, making the complexes incomparable to each other. This is especially true for Cu-substituted-triazole complexes.[42] Another possible reason is the steric effect of the substituents. It has been reported that the presence of methyl groups on the TPA (tris(2-pyridylmethyl)amine) ligand as well as mesityl substituents of porphyrin ring-forming synthetic heme (Cu-Fe-ligand) could adjust the Fe-Cu distance in the heme and hence the reactivity of the synthetic heme.[38] Functional groups of similar size could tune the electronic properties of the catalysts without introducing steric effects. Here a series of Cu(II)-3-amino-5-substituent-1,2,4-triazole complexes was studied as electrocatalysts. Due to the diverse structures of 3-amino-5-substituent-1,2,4-triazole, the lowest energy tautomer is

evaluated. The electron densities of the binding sites, namely N1 and N2 and in the triazole ring, are correlated with the ORR performance of these catalysts. Other items such as redox potentials and copper binding amount of catalysts were also listed to correlate with ORR performance.

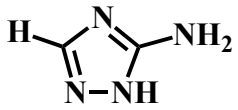
4.2 Experimental procedures

Chemicals, if used, are the same as those described in section 2.2.1. Three triazoles (1H-1,2,4-triazole-3,5-diamine(DATZ), 5-(methylthio)-1H-1,2,4-triazole-3-amine (SATZ), 3-amino-1H-1,2,4-triazole-5-thiol (HSATZ) were purchased from Acros Organics. 1H-1,2,4-triazol-3-amine (ATZ) was provided by AK Scientific. Inc. and methyl 3-amino-1H-1,2,4-triazole-5-carboxylate hydrochloride (CATZ) was synthesized by Dr. Shane Foister. The structures of these five ligands are shown in Fig. 4.1. Catalysts used are immobilized catalysts.

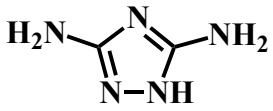
Electrode preparation and electrochemical characterization are the same as described in section 2.2.5 and 2.2.6 respectively.

4.3 Computational method

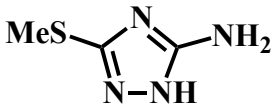
Geometry optimization was conducted on different substituted 1,2,4-triazoles using density functional theory (DFT) method equipped with Becke-style-3-parameter, the Lee, Yang and Parr correlation functional methods (B3LYP) and the standard 6-31G basis set. The predicted energies in Table 4.1 and Mulliken atomic charges in Table 4.2 were obtained from the single point energy calculation and partitions of the total charge among the atoms in the molecule respectively. All the calculations were performed in Gaussian 09 programming environment.



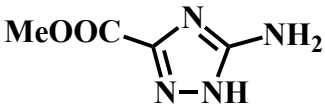
1*H*-1,2,4-triazol-5-amine (ATZ)



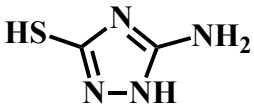
1*H*-1,2,4-triazole-3,5-diamine (DATZ)



3-(methylthio)-1*H*-1,2,4-triazol-5-amine (SATZ)



methyl 5-amino-1*H*-1,2,4-triazole-3-carboxylate (CATZ)



5-amino-1*H*-1,2,4-triazole-3-thiol (HSATZ)

Figure 4.1 Structures of ligands used in this study.

4.4 Catalysis based on Cu(II)-3-amino-5-substituent-1,2,4-triazoles complexes.

The electron withdrawing and donating properties of substituents could change the electron density of the central metal, which results in adjustment of the ORR activity of different complexes. Among these five substituted complexes, the most extensively studied one is Cu-DATZ in the literature due to the similarity of DATZ to the imidazole which occurs in the enzyme and its bridging capability which could lead to formation of polynuclear compound.[40,42] Others are barely reported so far. Fig. 4.2 and 4.3 show the O_2 reduction cathodic curves and number of electrons transferred obtained from RRDE for Cu(II)-3-amino-5-substituent-1,2,4-triazoles-based catalysts and the CVs for each

catalyst, respectively. The onset potentials E^{O2}_{onset} and half-wave potentials $E^{O2}_{1/2}$ are listed in Table 1. The onset potentials were evaluated as the potential where the ORR reduction current density is -5 $\mu A/cm^2$.

The best ORR performance was obtained with the $-NH_2$ substituent with an onset potential ca. 0.498 V, then followed by -H, $-SCH_3$, $-COOCH_3$ and -SH in an order of decreasing activity. The ORR activity decreases with decreasing electron donating character of the substituents. $-NH_2$ is a typical electron-donating group and the donating effect decreases as substituents vary from $-SCH_3$, -H, $-COOCH_3$ and -SH. While $-SCH_3$ has better electron-donating capability but less performance than –H, this could possibly be explained by the larger size of $-SCH_3$ resulting in steric effects when the ligand forms complexes with Cu. It is also possible that the $–SCH_3$ is oxidized to methylsulfinyl or methylsulfonyl group, which rather have electron withdrawing properties.

The number of electrons transferred was calculated by equation 2.1. The amount of hydrogen peroxide production in the limiting current region increases in the order of $-NH_2$, -SH, $-SCH_3$, $-COOCH_3$ and -H. Though the -SH substituted catalyst shows the lowest ORR onset potential and half-wave potential, its hydrogen peroxide production is second least in the series. It is important to note that ligand with –SH binds 100% of theCu(II) added in the solution. Though not all of the Cu(II) complexes are catalytically active, it still may have a higher chance of forming higher density of active sites than other complexes. Additionally, depending on the type of substituents, the adsorption mode of O_2 with the central metal could be altered and form edge-on, flat and end-on adduct, as mentioned in the review above. This could potentially change the reaction

pathway for different Cu-substituted complex-based catalysts and hence the number of electrons transferred.

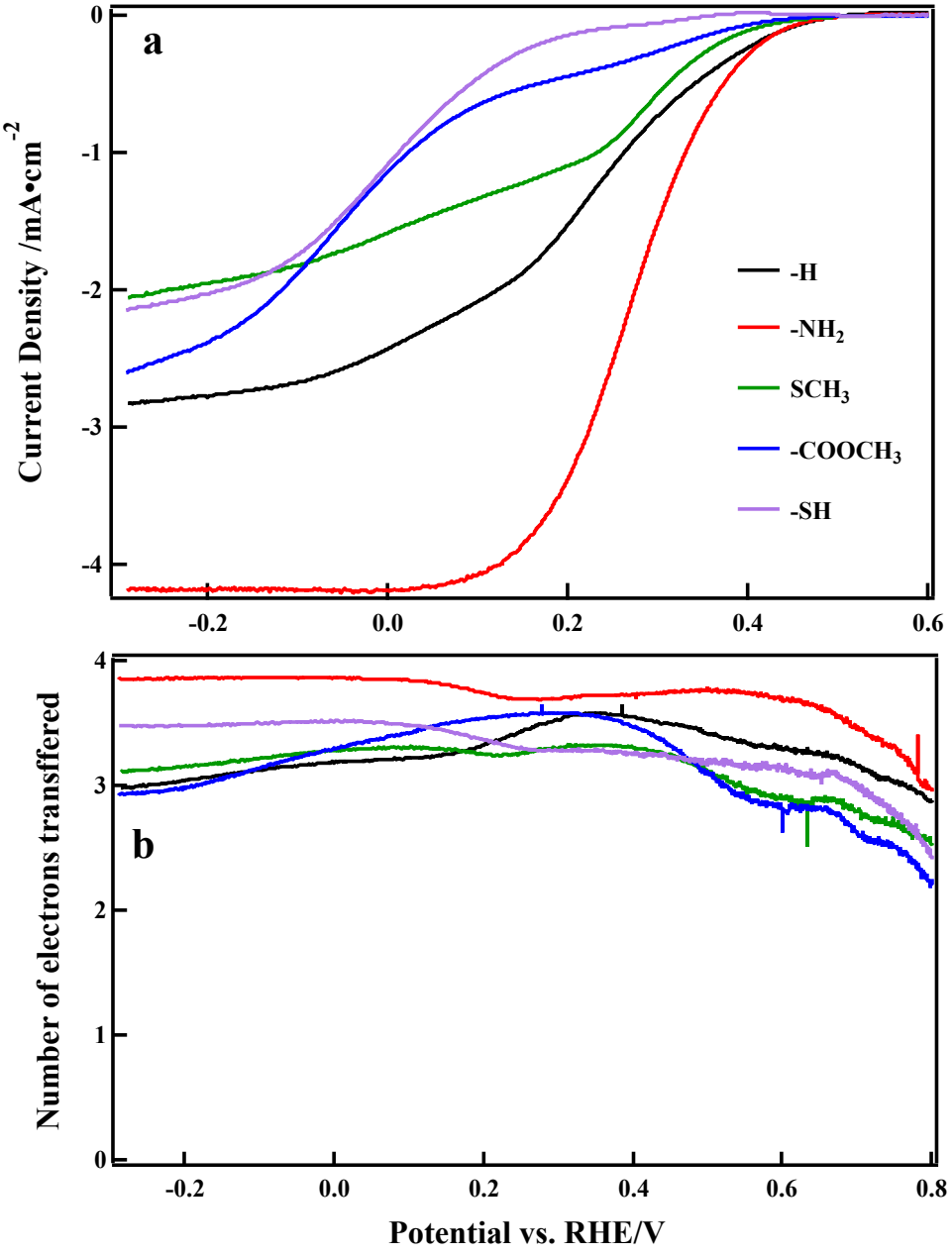


Figure 4.2 a. RDE cathodic curves of Cu(II)-3-amino-5-substituent-1,2,4-triazoles complex-based catalysts. b. Number of electrons transferred.

The redox potential is an important aspect in the catalyst behavior. Fig. 4.3 shows the CVs of the five substituted catalysts in N_2 saturated electrolyte. As we can see, the redox peaks are not symmetric and the peak separations, which are indicated by the distance between the dark red lines on each CV, are generally higher than 59 mV. This suggests that the redox couples in our catalysts are not all reversible. There is one major pair of redox peaks for each complex under potential range investigated. This is different from previously studied Fe-phthalocyanine complexes, which demonstrate multiple redox couples. However, most of them are reversible.[133]

If the potential of the middle point between the dark red lines is taken as a measurement of redox potential of Cu species in our catalysts, the values of which are listed as $E^{0'}$ in Table 4.1, it is still difficult to relate the redox potentials of these complexes to their ORR catalytic activities, as opposed to the case for Cu-substituted phenanthroline complexes, in which the more positive the redox potential, the worse the ORR performance.[35] This could possibly be caused by the higher diversity of Cu-substituted 1,2,4-triazole complexes than Cu-substituted phenanthroline complexes. However, in their study the highest ORR onset potential obtained from Cu-substituted phenanthroline at pH 4.8 is 305 mV vs. NHE and this value is much lower than the onset potentials from Cu-substituted 1,2,4-triazole based catalysts in 0.1 M H_2SO_4 in our study.

The onset potential for Cu(II) reduction is measured from the right end of dashed lines on each CV on Fig. 4.3. In this way, the capacitance currents can be deducted while determining where Cu(II) reduction starts. All onset potentials of Cu(II) reduction are higher than ORR onset potentials except the one with $-COOCH_3$. It is obvious that the formation of reduced Cu form Cu(I) is the driven force for ORR.

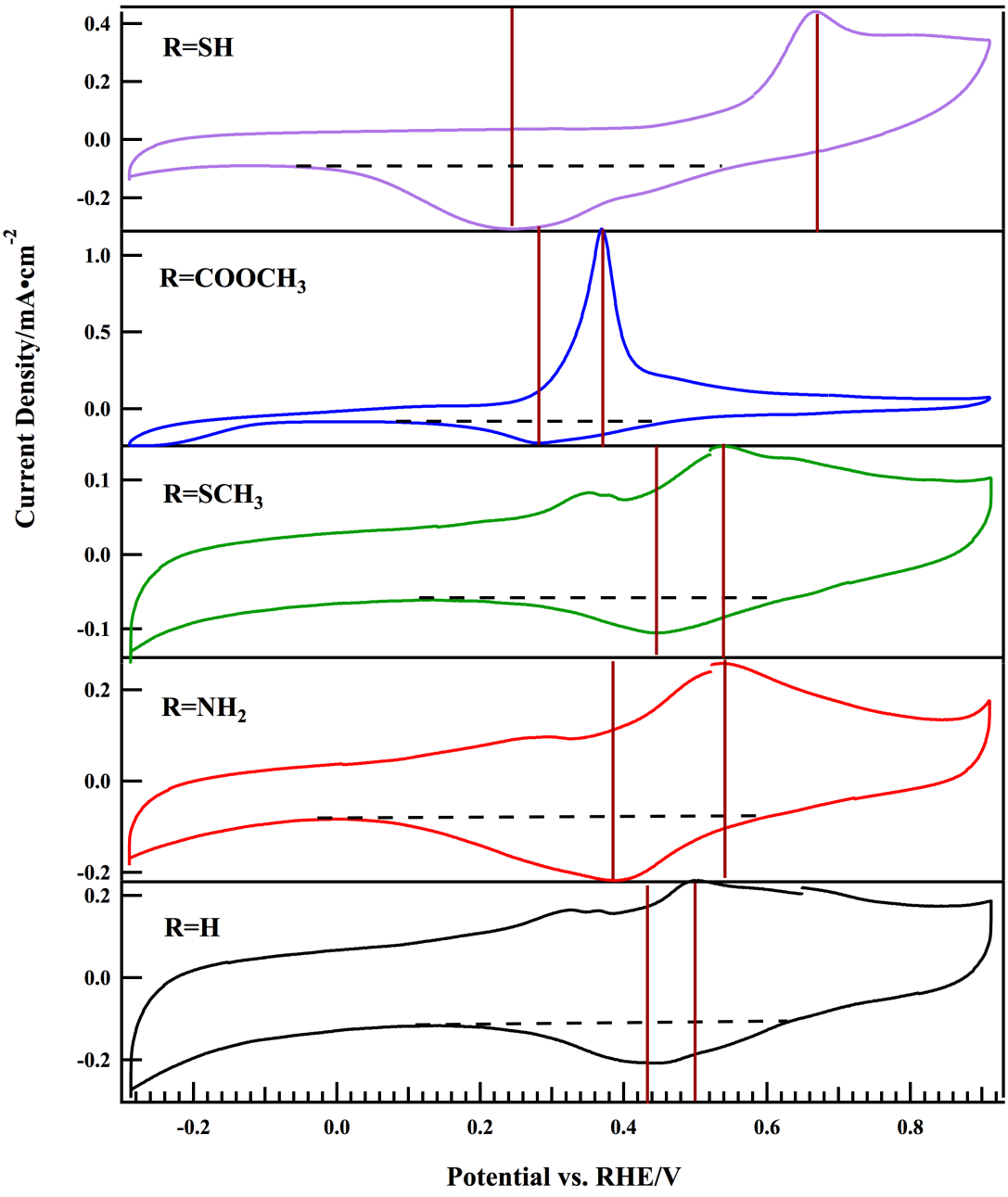


Figure 4.3 CVs of five Cu(II)-3-amino-5-substituent-1,2,4-triazoles complex-based-catalysts in N_2 saturated 0.1M H_2SO_4. Redox potentials of $Cu(II)L_n/Cu(I)L_m$ in the catalysts are calculated by taking the middle points of the two dark red lines which might be an indication of oxidation and reduction peaks of redox couple.

Table 4.1 lists the amount of Cu binding by ligands with and without the presence of diazotization modified BP2K. The one with -H substitution did not form solid precipitate

without the presence of carbon. The higher copper binding in the presence of modified BP2K suggests that the ligand immobilized on the carbon surface can also form complexes (complexes II and III in Fig. 2.1c) in addition to the complexes formed in the solution phase and adsorbed on carbon surface (complex I in Fig. 2.1c).

Table 4.1 Experimental data of E^{O2}_{onset} , $E^{O2}_{1/2}$, $E^{Cu(II)}_{onset}$ and $E^{0'}$ of five Cu(II)-triazole complex-based catalysts and Mulliken atomic charges on N1, N2 and N4 in triazole ring calculated from electrostatic potential analysis by Gaussian 09 program

Substituents R	E^{O2}_{onset} (mV)	$E^{O2}_{1/2}$ (mV)	$E^{Cu(II)}_{onset}$ (mV)	$E^{0'}$ (mV)	Cu(II) loading w/ carbon (mmol/g)	Cu(II) loading w/o carbon (mmol/g)	Mulliken atomic charges		
							N1	N2	N4
H	494	213	600	480	2.88	0.462	-0.401	-0.340	-0.483
NH_2	498	270	610	470	6.76	5.46	-0.350	-0.476	-0.545
SCH_3	493	224	620	493	6.18	4.88	-0.439	-0.345	-0.513
$COOCH_3$	468	24	460	326	5.9	5.04	-0.443	-0.322	-0.574
SH	346	2	570	460	10	9.94	-0.424	-0.339	-0.495

Except for the catalyst with –SH, the one with $–NH_2$ shows the highest Cu(II) binding amount in both the presence and absence of carbon support. However, the second highest ORR performance of the catalyst with –H does not come with the second highest amount of Cu binding. The catalysts with $–COOCH_3$ and $–SCH_3$, which have lower performance than the one with –H, exhibit higher Cu binding amounts. This inconsistency in performance and Cu binding amount excludes the possibility of Cu binding amount as playing a significant role in dominating the ORR performance of the catalysts and leads us to look into Cu binding contributing to effective catalytic sites.

4.5 Dependence of ORR performance on Mulliken charges on nitrogen in triazole ring

To investigate the electronic properties of the Cu-triazole complexes in the catalysts, the Mulliken charges on the nitrogen in triazole ring are calculated. The Mulliken charge is one measure of electron density on atoms. The more negative the charge, the higher the electron density. In order to compare nitrogen Mulliken charges on a triazole ring, the lowest energy tautomer was found by calculating the single point energies for three possible tautomers L1, L2 and L3 indicated in Fig. 4.4.

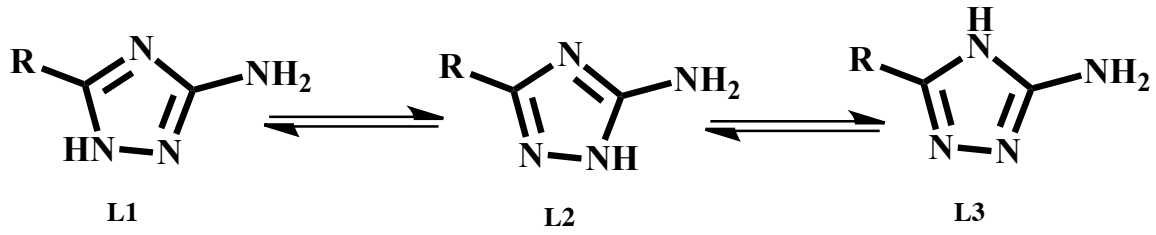


Figure 4.4 Three most favorable tautomers of DATZ in aqueous solution: L1, L2 and L3.

It has been reported by many researchers that 1H and 4H are the most favorable structures existing in both gas phase and aqueous solution for DATZ.[40,134] There is no difference in structure for DATZ when the ring H is at 1 or 2 position because of the symmetry of DATZ. However, for the other four ligands, L1(1H) has been proved to be the most favorable tautomer. The single point energy of L1 in our calculation with DATZ is very close to that reported in Aznar's work using the same basis set and method.[92] The single point energies E of the other four substituted triazoles in L1, L2 and L3 forms are calculated. For the convenience of comparison and instead of listing all the absolute

energy values, the energy differences ΔE of L2 and L3 from L1 are listed in Table 4.2 for all triazoles.

Table 4.2 Single point energies E of three most possible tautomers for five substituted triazoles in gas phase, The more negative of ΔE values, the lower energy of the tautomer than L1 and vice versa.

Substituents R	E(B3LYP)(Hartree)			ΔE (kJ/mol)		
	L1	L2	L3	L1	L2	L3
H	-297.603	-297.603	-297.588	0.000	-1.418	41.495
NH_2	-352.955	-352.955	-352.947	0.000	0.000	20.846
SCH_3	-735.103	-735.099	-735.081	0.000	8.962	46.718
$COOCH_3$	-525.452	-525.461	-525.452	0.000	-23.331	22.540
SH	-695.787	-695.782	-695.769	0.000	13.837	32.320

All L3 energies are higher than L1. L2 energies are lower than L1 except in the case of -SCH_3 and –SH. Their single point energies are higher by about 8.962 kJ/mol and 13.837 kJ/mol respectively. This energy difference could lead to about two orders of magnitude difference in equilibrium constant between L1 and L2. Basically, two species with this energy difference will exist in equilibrium with both present in fair amounts. Accordingly, the L1 form is chosen to compare the Mulliken charges on N1 and N2 for all triazoles for the sake of consistency.

Table 4.1 lists Mulliken atomic charges on N1, N2, and N4 in L1 tautomer for all substituents. We assume that N1 and N2 are the two metal binding sites.[39,42,111] The N4 nitrogen bears high negative Mulliken atomic charges and there is no strong relationship between the metal binding amount and N4 charge. The N2 electron density for all

substituents decreases in an order of -NH_2 -SCH_3, -H, -SH, -$COOCH_3$. A higher electron density on N2 can increase the bonding strength with Cu(II) via the attracting effect of heterogeneous charges. N2 has a higher electron density in the case of -SH than -$COOCH_3$ but its activity is the least. It is likely that S can also bind a certain amount of Cu and compete with the N2 to form non-active complexes according to the high metal binding facility of functional group -SH. When it comes to N1, lower electron density will be more favorable since Cu(II) has to deprotonate the H on it before binding. The electron density on N1 increases in an order of -NH_2, -H, -SH, -SCH_3, -$COOCH_3$. The catalyst with -NH_2 substituent exhibits the least electron density on the H so it can be removed more easily than others. The catalyst with -H shows better ORR performance than the one with -SCH_3 probably because that their N2 electron densities are comparable but the N1 of -SCH_3 has a much higher electron density, making it difficult for deprotonation leading to less Cu binding. Both low electron density on N2 and high electron density on N1 contribute to the low performance of the catalyst with -$COOCH_3$ in the series. For whatever reason, the catalyst with -SH does not fit with this series of compounds. As noted, its high number of electrons transferred shown in ORR might be taken advantage of through structure study of this kind of complex.

4.6 Conclusions

A series of substituted Cu-triazole complex-based catalysts were synthesized in this part. The effect of electronic properties of the ligand, redox potentials of complexes, and Cu binding amount on the ORR performance of these catalysts were discussed. It was found that electron-donating groups on the triazole ring are favorable for ORR activity in general but steric effects and other metal binding sites should be considered. This is

because electron donating groups increase the electron density on N2 but decrease that in N1. Both effects facilitate the binding of Cu to the triazole ring and contribute to effective catalytic sites.

However a strong relationship between ORR performance and the binding amount by copper complexes was not observed. For instance, the –SH substituted triazole exihibits strong metal binding ability but its activity is worst. This might be caused by metal binding with heterogenous atoms other than nitrogen, such as sulfur, which might result in inactive catalytic sites. The selection of substituents should be taken with great care. More systematic results would be obtained to choose substituents with similar sizes and less side reactions with Cu(II).

5 Elemental analysis and spectroscopic studies of Cu(II) based electrocatalysts

5.1 Introduction

Considering the different ORR activities of different substituted Cu(II)-complex-based electrocatalysts from the last chapter, more information about the structures of these complexes would be helpful to gain more understanding about factors contributing to the differences in their performance.

The first spectroscopic experiment proposed is the attenuated total reflected (ATR) FTIR experiment. It can provide information about complexes on the surface of a substrate up to 5 μm in depth. FTIR is sensitive to the vibration of organic bonds at frequencies in the infrared region of the spectrum. However the metal shows no adsorption in the mid-infrared spectrum. As discussed in section 2.5, Cu(II) itself is barely adsorbed on carbon surface but in the presence of ligands, the formation of Cu(II) complexes is significantly increased on the carbon surface. By looking at the ligand on the catalyst surface, we can probe the complexes on the carbon surface.

Elemental analysis of the complexes formed without the carbon support was conducted to provide approximate Cu(II)/ligand ratio in the complexes on the carbon surface given that the complexes formed without carbon surface are the same as those formed with carbon surface.

Electron paramagnetic resonance (EPR) is a valuable method to investigate materials that possess unpaired electrons, such as ions, radicals, and peroxides *etc.* Applications of EPR range from analyses of proteins,[135,136] degradation processes in polymers for energy related applications[137,138], metals and metal oxides.[139,140] One simple application of EPR spectroscopy is to determine the geometry of complexes formed with a wide range of

metal ions.[141–143] The method of evaluating the geometry of Cu(II) complexes is described in detail in section 5.5.

5.2 Experimental procedures

5.2.1 Attenuated total reflected FT-IR (ATR-FTIR)

ATR-FTIR spectra of all samples (that is, the carbon support, pure ligands, catalysts, modified carbon and pure complexes made without carbon support) of five substituents were collected with a Bruker Vertex 70 FTIR spectrometer using a liquid nitrogen-cooled detector. The refractive crystal is ZnSe. Samples of about 5 mg with methanol were sonication for 20 min before deposition on the crystal. Sample was deposited on the crystal plate until the amplitude of reflected beam is around 5000. The spectrum is scanned from 450 to 4000 cm^{-1}.

5.2.2 Elemental analysis

The Cu amount in the complexes prepared without carbon support was measured by ICP using the same method described in section 2.2.7 after aqua regia digestion. The content of N was measured by Galbraith Laboratories for each sample.

5.2.3 EPR measurement

EPR spectra of five substituted catalysts were collected using an X band Magnettech EPR spectrometer with a rectangular cavity at room temperature. Ground catalyst powder was loaded into a capillary tube with a diameter of 1mm. The end of the capillary was then capped with paraffin. The field is scanned from 500-4500G. Parameters including modulation amplitude, attenuation, number of passes and gain were adjusted for optimal signal intensity for each sample.

5.3 Simulation method

EPR spectra were simulated using Matlab R2012b with a computational package Easyspin 4.5.5. The 'pepper' function was chosen to simulate the solid state EPR spectra.[144] A doublet Cu(II) was used as the nucleus. An axial geometry of g values was adopted. The variables are $g_{\perp}$ and $g_{\parallel}$, hyperfine splitting $A_{\perp}$ and $A_{\parallel}$, and line width.

5.4 ATR-FTIR spectra of Cu based electrocatalysts

IR spectra of DATZ have been reported in detail and the data is in agreement with this study.[145] Fig. 5.1 shows ATR-FTIR spectra of unmodified BP2K (purple), pure ligand (red), diazotization-modified BP2K (blue), Cu(II)-ligand complexes prepared without carbon(green), Cu (II)-DATZ complexes adsorbed on carbon support(catalysts, black). Figures 5.1a-e show the results when the substituents are $–NH_2$, -H, $-SCH_3$, $-COOCH_3$, -SH. In Fig. 5.1a, peaks near 3500-3000 cm^{-1} can be assigned to the typical stretching mode of an amino group including NH_2 and NH.[145] Peaks from 1650-1300 cm^{-1} represent a mixture of the bending modes of N-H and in-plane and out-of-plane deformation of the triazole ring.[145] Cu(II)-DATZ complexes prepared without carbon support, show major peaks between 1650-1300 cm^{-1} that are similar to those in the spectrum of Cu(II)-DATZ complexes adsorbed on carbon support. This result indicates that Cu(II) complexes structures are well preserved on the surface of carbon substrate. The spectrum of DATZ-modified carbon shows very similar peaks to the unmodified carbon spectrum (spectrum in purple in Fig. 5.1b). Diazotization chemistry cannot be verified by ATR-FTIR spectra of diazotization-modified carbon support because the triazole ring structure of ligands is not observed on the modified carbon surface. It could be possible that triazole rings were just embedded in the macrocyclic carbon support or

within pores rather than on the outer surface. The peaks from complexes on the carbon support are less resolved than that of complexes prepared without the carbon support, indicating the dilution effect of the carbon support towards the IR signal. The strong peak at 610 cm^{-1} is from carbon support since it only occurs at samples with carbon support.

In Fig. 5.1b, c, d and e, peaks around 3500-3000cm^{-1}, 1650cm^{-1} to 1300cm^{-1} and the strong peak at 600 cm^{-1} in the spectrum of the ligand represent the same bond mode as those described in Fig. 5.1a. In Fig. 5.1c, one additional peak related to C-S stretching is seen around 800-600cm^{-1} in both the catalyst and the complex spectra.[146,147] This is an indication that $–SCH_3$ substituted ligands form complexes with Cu(II) and the complexes are on the surface of the carbon support.[134,148] In Fig. 5.1d, the occurrence of typical strong C-O stretching mode around 1250cm^{-1} and C=O stretch mode at 1710 cm^{-1} provide support for $–COOCH_3$ group in Cu-CATZ (see the structure of CATZ in Fig. 4.1) complexes on carbon surface.[146,147,149] In Fig. 5.1e, modes related to S-H stretching at 2500 cm^{-1} are only seen in the ligand spectrum and very weak.[148] The relative intensity of C-S stretching modes in the spectrum of the complex only (green) is significantly stronger than that in the ligand spectrum.[146–148] These observations can be explained as follows: when Cu(II) forms a complex with an –SH substituted ligand, -SH tends to form C-S-Cu(II). This assumption is in line with the observation that ligand with -SH does not dissolve in water but once Cu(II) solution, which is blue, was added, most metal formed complexes, ending up with colorless supernatant.

In general, Cu(II) complex structures are preserved on the surface of the carbon support. Bands of complexes on the carbon support are less resolved than that of complexes prepared without the carbon support, indicating the dilution effect of the

carbon support towards the IR signal. Diazotization chemistry cannot be verified by ATR-IR spectra of the ligand modified carbon support because the triazole ring structures of covalently bonded ligands on the modified carbon surface were not observed. Basically, the modified carbons show the same spectra as that of unmodified carbon. It could be possible that without coordinating to central Cu(II), triazole rings were just embedded in the macrocyclic carbon support rather than appeared on the surface.

5.5 Elemental analysis of Cu based electrocatalysts

The ATR-FTIR study of complexes and catalysts supports the conclusion that complexes adsorbed on the carbon supports have the same structures as complexes prepared without carbon support. However limited information has been obtained on the structure of the Cu(II) complexes. Elemental analysis of complexes synthesized without the carbon support was done to estimate the Cu(II)/ligand ratio and to provide insight regarding the complexes adsorbed on the carbon surface.

The data are shown in Table 5.1. R groups include $–NH_2$, $-SCH_3$, $-COOCH_3$ and -SH. The contents of N were measured by Galbraith Laboratories. Cu content was determined by ICP after aqua regia digestion. Thorum *et al.* measured the elemental compositions of their Cu(II)-DATZ-based catalyst and found the ratio of Cu(II) to DATZ is about 1:1.[32] In our study, it was found Cu/ligand ratio is close to 2:1 when the substituents are $-NH_2$ and -SH. This agrees with the data in the copper binding amounts in Table 4.1 that the ligand with $-NH_2$ and -SH substituents bind the most Cu(II) amount. For substituent -SH, -SH is very possible to be the binding site with Cu besides N in the triazole ring. $-NH_2$ could also bind Cu(II). One possible structure frame with Cu:ligand ratio 2:1 is proposed in Fig. 5.2. for the situation with $–NH_2$, the S atom changes into NH.

Figure 5.1 ATR-FTIR spectra of unmodified BP2K (purple), pure ligand (red), diazotization modified BP2K (blues), Cu(II)-ligand complexes prepared without carbon support (greens), Cu(II)-DATZ complexes adsorbed on carbon support(catalysts, blacks) when the substituents on ligands are $–NH_2$, -H, $-SCH_3$,$-COOCH_3$, -SH.

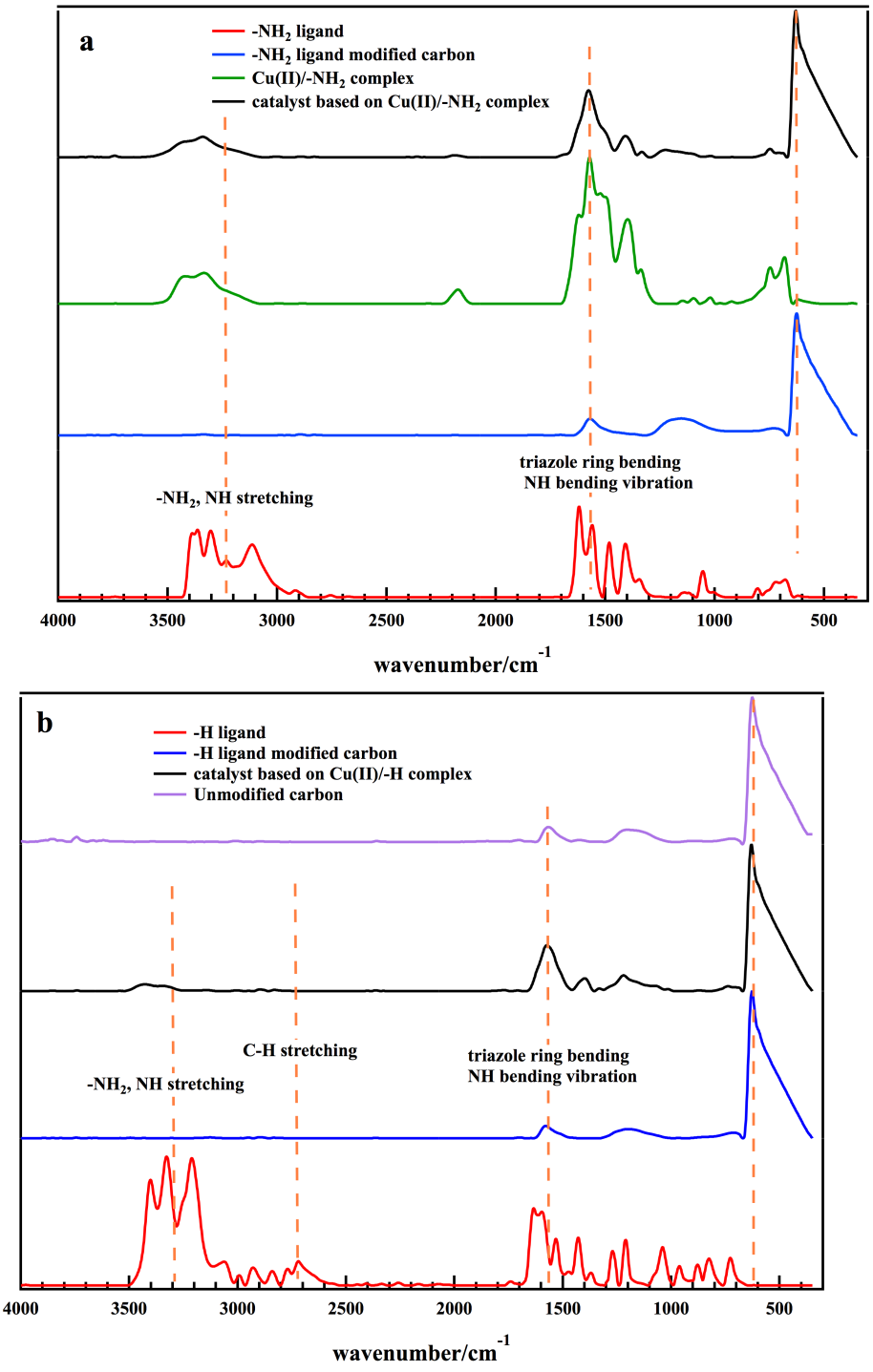


Figure 5.1 continued

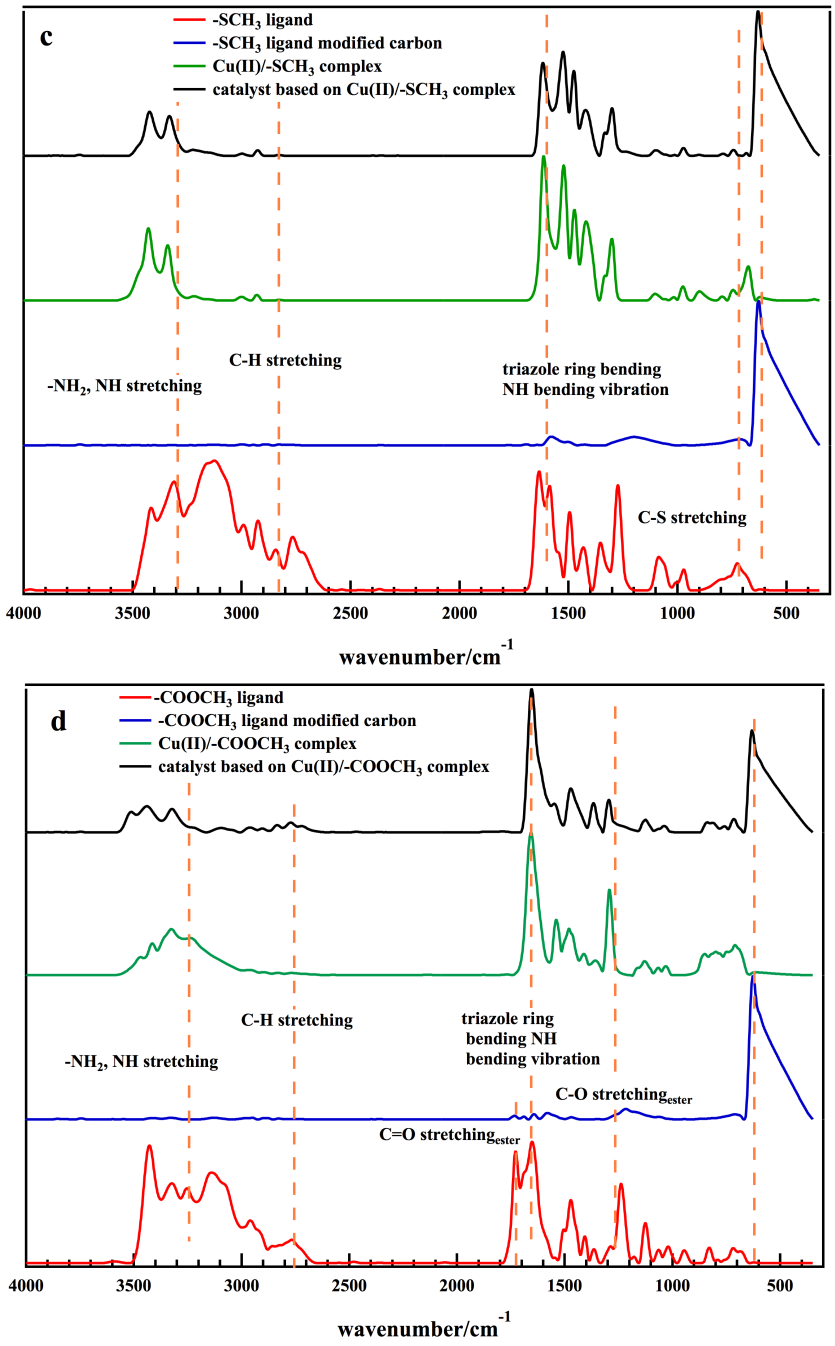


Figure 5.1 continued

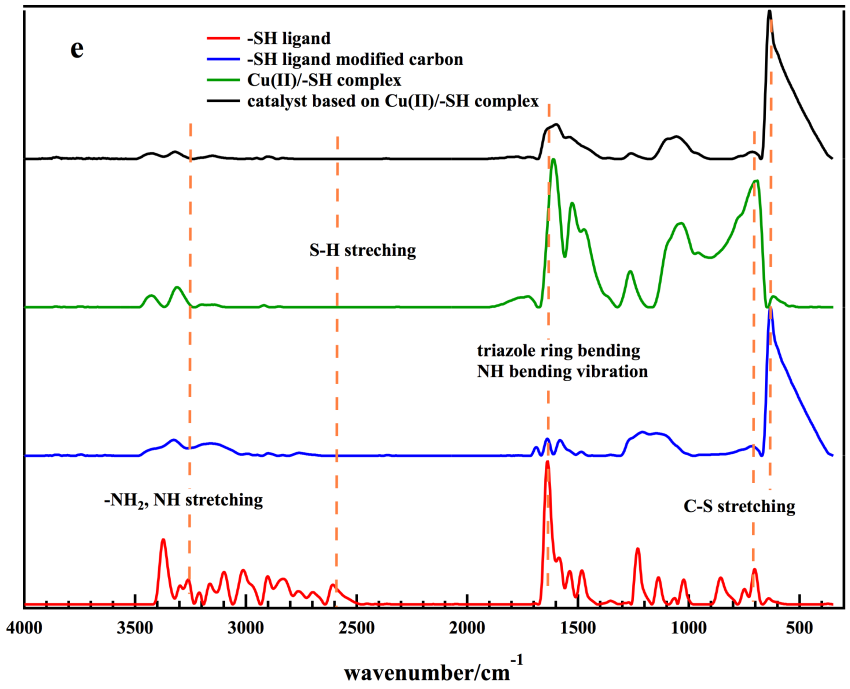


Figure 5.1 continued

When the substituent is SH on the triazole ring, this complex structure agrees with previous explanation in chapter 4 that S acts as an additional metal binding sites besides N1 and N2. When the substituent is NH_2, NH_2 acts as additional metal binding sites from this complex structure. This has been seen in other literature.[41]

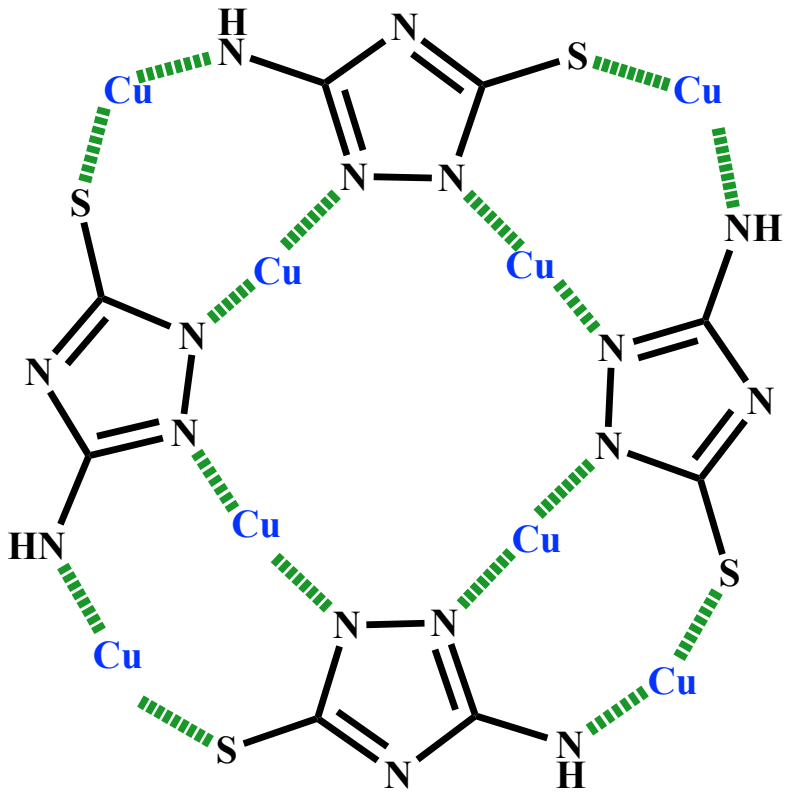


Figure 5.2 Possible structure frame for Cu: ligand ratio 2:1.

The Cu/ligand ratio is about 1:1 for the substituents $-SCH_3$ and $-COOCH_3$. This agrees with the observation that their total Cu(II) binding amounts are similar to the data shown in Table 4.1, but less than the cases when the substituents are NH_2 and SH. In the case of non-substituted ligand, there was no precipitation of complexes out of the solution.

5.6 EPR spectra of Cu-substituted triazole-based electrocatalysts

Extensive research has been done by Solomon *et al.* to investigate the spectroscopic features and electronic structures of multi-copper containing enzymes, reflecting their biological catalytic function.

Table 5.1 Elemental analysis for complexes Cu(II)-3-amino-5-substituent-1,2,4-triazoles.

R	NH_2	SCH_3	$COOCH_3$	SH
Cu/N w.t.%	38.33/22.69	24.18/23.2	25.19/26.97	41.5/22.48
Cu/ligand ratio	2:1	1:1	1:1	2:1

They identified electronic features of exchange coupled triagonal trimeric Cu(II) complexes as a spin frustrated ground state undergoing zero field splitting into two doublets states and coupling interactions via the spin orbit coupling mechanism. While the former is reflected by their unusual ground state EPR spectral features, the latter is manifested in the magnetic circular dichroism (MCD) spectrum.[150,151]

Cu(II) has an unpaired electron and could be detected by EPR due to the net electron spin. EPR spectra of multinuclear forms of Cu(II) exhibit characteristic features resulting from coupling interactions between the unpaired electrons.[114,115,152–154] Additionally the geometry of mononuclear Cu(II) complexes could be determined from the measurement of g factors of EPR spectra.[143,155] Theoretically, the free electron has a g factor = 2.0023 determined from the equation below:

$$g = \frac{h\nu}{\mu_B B} \quad (5.1)$$

Where h is the Plank's constant, ν is the frequency of microwave, μ_B is the Bohr magneton. B is the magnetic field position where the g values are measured. In this study, the resonance field of the free electron occurs around 3340-3380 G.

The external magnetic field causes the electron spin to lose its degeneracy and form different spin states. This effect is called electronic Zeeman interaction. In a transition metal, the spin-orbital coupling is an important effect causing the g factor to shift from the g factor values for the free electron. Another important interaction is the nuclear Zeeman effect caused by the non-zero angular momentum of transition metal nuclei and ligand nuclei. Both effects result in fine lines in the major transition peak since they are weaker than the electron Zeeman effect. The former is called hyperfine splitting and the latter is superhyperfine splitting.[141] The following study focuses mostly on the spin-orbital interaction which is observed in the EPR spectra of different substituted catalysts, as shown in Fig. 5.3. The deviation of g values (Δg) from free electron (g_e) along any direction can be explained by applying the following theory:

$$g = g_e \pm \frac{n\lambda}{\Delta E} \quad (5.2)$$

Where n is the amount of orbit mixing. ΔE is the transition energy. λ is the ground state spin-orbital coupling constant. The plus sign $+$ applies to the case mixing with a more than half-filled orbital. The minus sign applies to the case mixing with less-than-half-filled configuration. Cu(II) with a d^9 satisfies more-than-half-filled situation. n values can be taken from the magic pentagon in Fig. 5.3.[141,156]

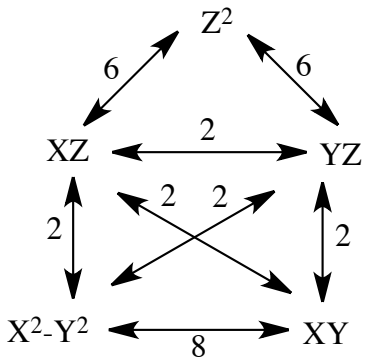


Figure 5.3 Magic pentagon for determining the value of n in equation 5.2.[141] (copied from reference 141)

For Cu(II) with d^9 orbital, if the unpaired electron resides in d_{x2-y2}, indicating d_{x2-y2} is the ground state, then

$$g_{||} = g_e + \frac{8\lambda}{\Delta E(d_{x^2-y^2} - d_{xy})} \quad (5.3)$$

$$g_{\perp} = g_e + \frac{2\lambda}{\Delta E(d_{x^2-y^2} - d_{xz,yz})} \quad (5.4)$$

The relationship $g_{||} > g_{\perp} > g_e$ will be observed from the EPR spectrum. For a compound with an axial coordination geometry, $g_{||}$ occurs when the direction of magnetic field is parallel to the axis of the coordination geometry. $g_{\perp}$ occurs when the direction of magnetic field is perpendicular to the the axis of the coordination geometry. The geometry of the electron configuration of ground state d_{x2-y2} determines that the coordination geometry of the formed complex is a square planar-based geometry. Other possibilities based on this geometry are listed in Table 5.2.

If the unpaired electron resides in d_{z2}, indicating d_{z2} is the ground state, then

$$g_{||} = g_e \quad (5.5)$$

$$g_{\perp} = g_e + \frac{6\lambda}{\Delta E(d_{z^2} - d_{xz,yz})} \quad (5.6)$$

The relationship $g_{\perp} > g_{||} \approx g_e$ will be observed from the EPR spectrum. The possible coordination geometries of the complexes are listed in Table 5.2. These results from the measured g values of mononuclear Cu(II) complexes are summarized in Table 5.2.

Table 5.2 Implication from g values

g values	Ground state	Possible geometries
$g_{||} > g_{\perp} > g_e$	d_{x2-y2}	Elongated octahedron, square pyramid, square planar
$g_{\perp} > g_{||} \approx g_e$	d_{z2}	Compressed octahedron, triagonal bi-pyramid

Fig 5.4 shows the EPR spectra collected at room temperature at X band along with several simulated spectra. The g values determined from the simulation are listed in Table 5.3. When the substituents are -NH_2 and -$COOCH_3$, the simulated g values satisfied $g_{||} > g_{\perp} > g_e$, this strongly suggests that the catalysts based on -NH_2 and -$COOCH_3$ substituted triazoles have square planar structure with axial elongation, probably by anions.[156,157] The catalyst synthesized with ligand with -$COOCH_3$ has well-defined $g_{||}$ and $g_{\perp}$, indicating that the complex in this catalyst has more crystalline structure.[156] The EPR spectrum of the catalyst with the -NH_2 substituent on the triazole shows the unresolved hyperfine splitting from 2000 to 3000 G. This could possibly be explained by the low concentration of Cu(II) in the catalyst.[158] The simulated EPR spectrum of the catalyst with -H satisfies the case where $g_{\perp} > g_{||} \approx g_e$, indicating a compressed octahedral coordination geometry in the complex.[141,155,156] The EPR spectra of catalysts

with -SCH_3 and -SH look like a square-planar Cu(II) spectrum with $g_{||} > g_{\perp} > g_e$ and with small difference in $g_{||}$ and $g_{\perp}$, resulting in unresolved peaks where $g_{||}$ and $g_{\perp}$ are.[159] This suggests that the axial bond in the octahedral structure is weaker in the cases of catalysts with -SH and -SCH_3 than the catalyst with -$COOCH_3$ and -NH_2. All the complexes in the catalysts have axially symmetric structures. The catalyst with H has a compressed octahedron structure while the catalysts with NH_2, $COOCH_3$, SH and SCH_3 have an elongated octahedron, in which the Cu(II) in the catalysts with SH and SCH_3 are weakly bonded in axial position.

From the simulated parameters $A_{\perp}$ and $A_{\parallel}$ in Table 5.3, in the complexes formed with ligand with R=-H and –$COOCH_3$, the hyperfine interaction is much weaker than that with complexes synthesized using ligand with R=NH_2, This suggests that their nuclear effect of the coordinated atoms on the electron spin is weaker, indicating a weaker bond between ligands with R=H and R=$COOCH_3$ and Cu than the ligand with R=NH_2. As the ligand with NH_2 leads to the highest ORR performance, this might provide a clue in synthesizing better catalyst that bond strength weaker than Cu and DATZ will not be a good catalyst. Additionally, comparing the values of $A_{\perp}$ and $A_{\parallel}$ in catalyst based on Cu and DATZ, the hyperfine interaction at the axial direction is much stronger than that in the perpendicular direction. All these features of Cu-DATZ based catalyst could be taken as possible references in synthesis better catalysts.

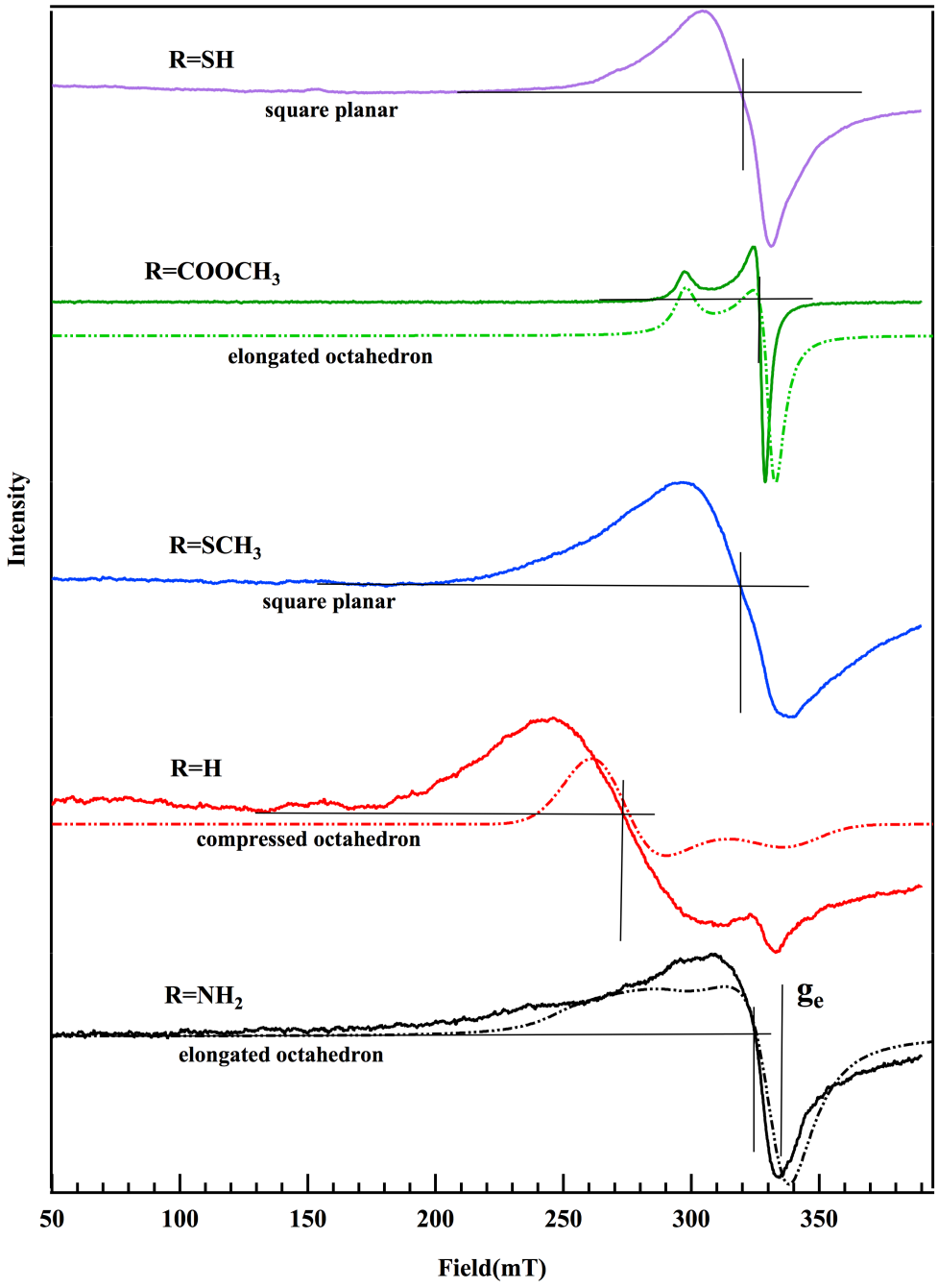


Figure 5.4 Powder EPR spectra of five substituted catalysts studied in chapter 4 at X band and room temperature (solid lines). The dashed lines are simulated EPR spectra using Easy Spin 4.5.5. The vertical lines of the cross mark are the possible position of $g_{\perp}$.

Table 5.3 Simulated results for EPR spectra of catalysts when the substituents are NH_2, H and $COOCH_3$.

Catalyst	$g_{\perp}$	$g_{\|\|}$	$A_{\perp}$ (MHz)	$A_{\|\|}$ (MHz)
R=NH_2	2.03	2.5	1	400
R=H	2.52	2.00	0.01	0.01
R=$COOCH_3$	2.04	2.27	0.01	0.01

5.7 Conclusions

In this chapter, ATR-FTIR, elemental analysis and EPR techniques were used to obtain a general idea about the structural information of the different substituted complexes studied in chapter 4. ATR-FTIR technique was employed to verify the covalently bonded ligand on carbon surface by diazotization modification and observe the change of complex structures with and without carbon support. However, the characteristic triazole ring structure was not observed on diazotization modified carbon surface. The ATR-FTIR spectra of the complexes are similar with and without carbon support except that the peaks of spectrum of complexes with carbon support are weaker than those without carbon support. Cu complexes are generally well-preserved on the carbon surface.

Elemental analysis of the different substituted complexes without carbon showed the Cu/ligand ratio is about 2:1 for substituents NH_2 and SH, and 1:1 for substituents SCH_3 and $COOCH_3$. The predicted Cu/ligand ratio for substituent H is 1:2 combining the data from Cu binding amount during synthesis in chapter 4.

EPR spectra of the different substituted catalysts at room temperature exhibited tetragonal geometry with different distortions at the axial positions for all substituents. The mechanism proposed in chapter 3 suggested that two Cu(I) centers are responsible the active sites in the Cu-DATZ-based catalyst. However, the binuclear feature was not observed from the EPR spectrum of the solid state of this catalyst. The reason is possibly that the two electron spins consisting of active sites are too far to demonstrate a coupling interaction.

For heterogeneous catalysts, solid-state information is helpful in defining the structure of the catalysts. It is still difficult to know what is really changing during the catalytic process. An *in situ* technique would be more promising to investigate the feature that plays a significant role in real time during catalysis.

6 Simultaneous electrochemical EPR study

6.1 Introduction

In situ electrochemical EPR has been of great interest due to the advantages of this technique in the identification of intermediates, elucidation of mechanism and evaluation of kinetic parameters of electrode processes.[160–162] It is advantageous to gain insight into the material via spectroscopic means to validate the electrochemical observations.

X-ray absorption/emission spectroscopy (XA/ES) can identify the electronic structure of metal center. Emerging *in situ* XAS techniques have provided a new perspective on the catalyst evolution at multiple potentials of ORR catalysis.[163,164] Most XAS measurements are time consuming, making it impossible to observe the catalyst evolution in real time.

The majority of *in situ* electrochemical cells for EPR have been designed to look at radical formation in solution. Recently, the design of an *in situ* fuel cell has been described [165] and it has been used to observe radical formation on carbon particles at the electrode surface as well as to monitor membrane degradation through spin trapping[166,167]. The design of a half-cell for *in situ* electrochemical EPR measurement allows the processes on the working electrode to be isolated and more easily distinguished.

A design of an electrochemical half-cell with parallel working and counter electrodes is described in a rectangular cavity of an EPR spectrometer. The main objective was to develop a strategy to observe changes in materials at the electrode surface. The material examined in this chapter is Cu-DATZ complexes adsorbed on diazotization modified carbon support.

6.2 Experimental procedure

6.2.1 Cell Design of in situ electrochemical cell in EPR spectrometer

Applications involving aqueous electrolytes in the *in situ* electrochemical cell require a cell thickness of less than 0.5 mm due to significant absorption of microwaves by the aqueous electrolyte solution.[168] However, this narrow width could cause high resistance for an electrochemical cell. Previous groups have tried to put counter electrode (CE) parallel to working electrode (WE) to reduce the potential drop caused by non-uniform current distribution between CE and WE. Unfortunately, the target paramagnetic species produced at WE were either consumed at CE or interfered with by species produced at CE through side reactions.[168,169] In this experiment the paramagnetic species are on the electrode surface. They are unlike the organic radicals in solution that could diffuse. As long as the EPR signal of target paramagnetic species can be resolved in a spectrum, it is valid to use this method to investigate the target paramagnetic species on the electrode.

A block diagram of the components of the *in situ* electrochemical EPR apparatus is shown in Fig. 6.1a. The electrolyte in the reservoir was purged with gas continuously during electrochemical measurements and circulated in the flat cell with a multichannel pump at a flow rate of 0.0325 ml/s (Cole Parmer). The *in situ* electrochemical cell was built in a quartz flat cell as indicated in Fig. 6.1b.

The arrangement of the WE and CE is shown in Fig. 6.1c. The WE and CE are separated by a 25 μm thick Celgard separator. The sides of the WE and CE with deposited active material face each other. This arrangement minimizes potential drop and encourages uniform current distribution in the cell. The covered area of the electrodes is the same length as the quartz window of the flat cell to maximize the EPR intensity of

paramagnetic species. The tip of the RE was positioned as near as possible to the WE to reduce the uncompensated resistance between the RE and WE. The cell assembly is sandwiched by two PTFE inserts of thickness 0.05 mm of the same length and width as the gold foil electrodes. These alignment features minimize the volume of lossy electrolyte in the cell and hold the electrodes in the center of the cavity in the electric field node. This design can be applied to other catalysts of this category simply by replacing the catalyst deposited on the unetched side of the gold foil. In many reports of *in situ* cell designs, the CE was mostly positioned outside the quartz window, which resulted in significant potential drop caused by the thickness of the flat cell. Chronopotentiometry experiments were conducted more often than potential controlled experiments because the cells did not offer enough potential control to allow well-defined reactions to occur on the WE.[168,170,171] Some side reactions on the CE could also produce radicals that interfere with the EPR signal of target species produced at the WE in their cell designs.[168,172,173]

6.2.2 Electrode preparation

Two gold foils were purchased from ESPI with purity 5N. The dimensions are 152mm in length, 3 mm in width and 0.05mm in thickness. The geometry of the gold foil was critical to tuning the microwave bridge. The microwave bridge of the EPR was found to not be tuned if the gold foil was inserted in the cavity without size adjustment. This is because the frequency of the microwave was shifted out of range by inserting extra metal in the cavity. [169,174]

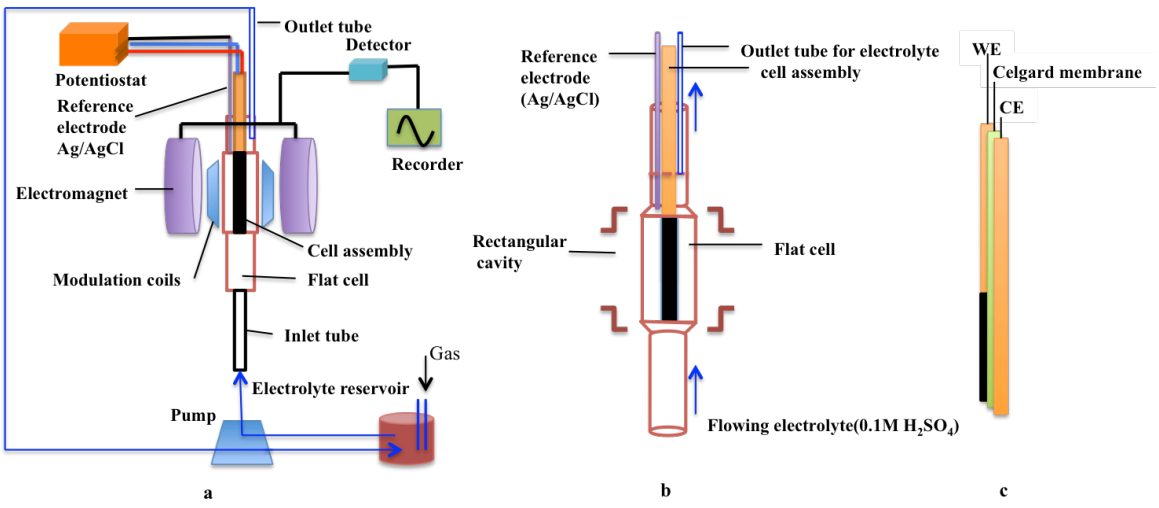


Figure 6.1 a. Block diagram of the *in situ* electrochemical EPR apparatus. b. Detail of *in situ* flat cell. c. Electrode arrangement in cell assembly.

To reduce the amount of metal present in the cavity, the part of the gold foil present in the cavity was etched thin by aqua regia and the width of the etched part is trimmed to 2.5 mm. The unetched side of the electrode was coated with catalyst to form the WE and with diazotization modified carbon support for CE using an airbrush. The geometry of the etched electrode is shown in Fig. 6.2.

The ink preparation protocol is as follows: a ground sample of 3 mg was mixed with 600 μL isopropanol and 300 μL H_2O and sonicated for 10 min. Then Nafion ionomer solution (5 w.t.%, 40 mg) was added to the above mixture. The mixture was stirred on a magnetic stirring plate for 3 days. The ink was sonicated for 30 min immediately before deposition on the unetched side of the gold foil. The estimated loading of the catalyst on the gold foil is about 800 $\mu g/cm^2$.

6.3 Electrochemical characterization of the *in situ* cell

6.3.1 Potential step experiment

A preliminary experiment to test the cell design involved observing the signal evolution at different steady states of the electrochemical reaction.

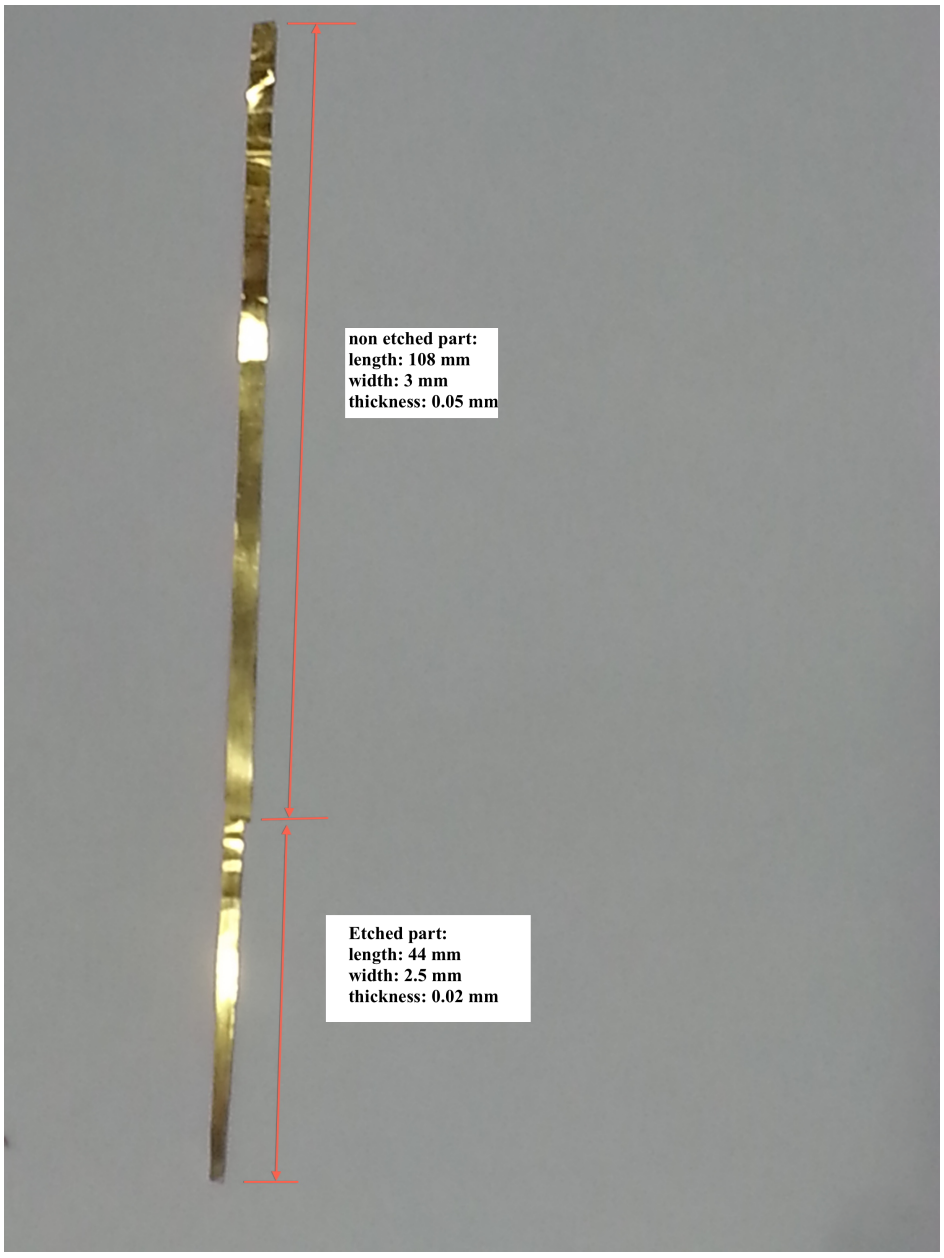


Figure 6.2 Geometry of etched gold foil.

While holding the WE at different potentials in N_2 saturated electrolyte, EPR is scanned over the field range of interest to record the spectra while holding the WE at each potential, as shown in Fig. 6.3. A background scan of the empty cell with only flowing electrolyte was used to correct the data. The broad peak from 290 to 330 mT indicated in Fig. 6.3 is the Cu(II) signal of interest while Cu(I) is EPR-silent. The peak position occurs at around 323 mT on the electrode while the solid-state study of powdered catalyst showed that the peak is around 310 mT. The shift toward high field might be caused by the interaction of H^+ and H_2O with Cu(II) center. The strong signal centered at 337mT in Fig. 6.3 is attributed to carbon-centered radicals formed on the CE. [165] Most of the Cu(II) signal in the catalyst from the cell assembly still can be resolved. The Cu(II) spectrum obtained without applying a potential is consistent with that typically observed for axially-elongated octahedral coordination geometry of Cu(II) centers, evidenced by the two components of the g factor ($g_{\parallel}$ and $g_{\perp}$) in the spectrum of Fig. 6.3. The fact that $g_{\parallel} > g_{\perp}$ suggests a d_{x2-y2} ground state.[156,175] The unresolved hyperfine splitting in the $g_{\parallel}$ region makes it impossible to draw more detailed conclusions about the ligand bonding.[176]

In Fig. 6.3, the dashed black box surrounds the Cu(II) signal at different potentials. As the potential is decreased, more EPR-silent Cu(I) forms and the paramagnetic Cu(II) signal decreases. The peak height at 320 mT is taken as an indication of the intensity of Cu(II) signal. The intensity of the Cu(II) peak is plotted vs. potential in the inset of Fig. 6.3, and shows three regions. This plot has the shape of a sampled steady state voltammogram for Cu(II) reduction, though detected in a spectroelectrochemical mode using the unpaired electrons in the system.

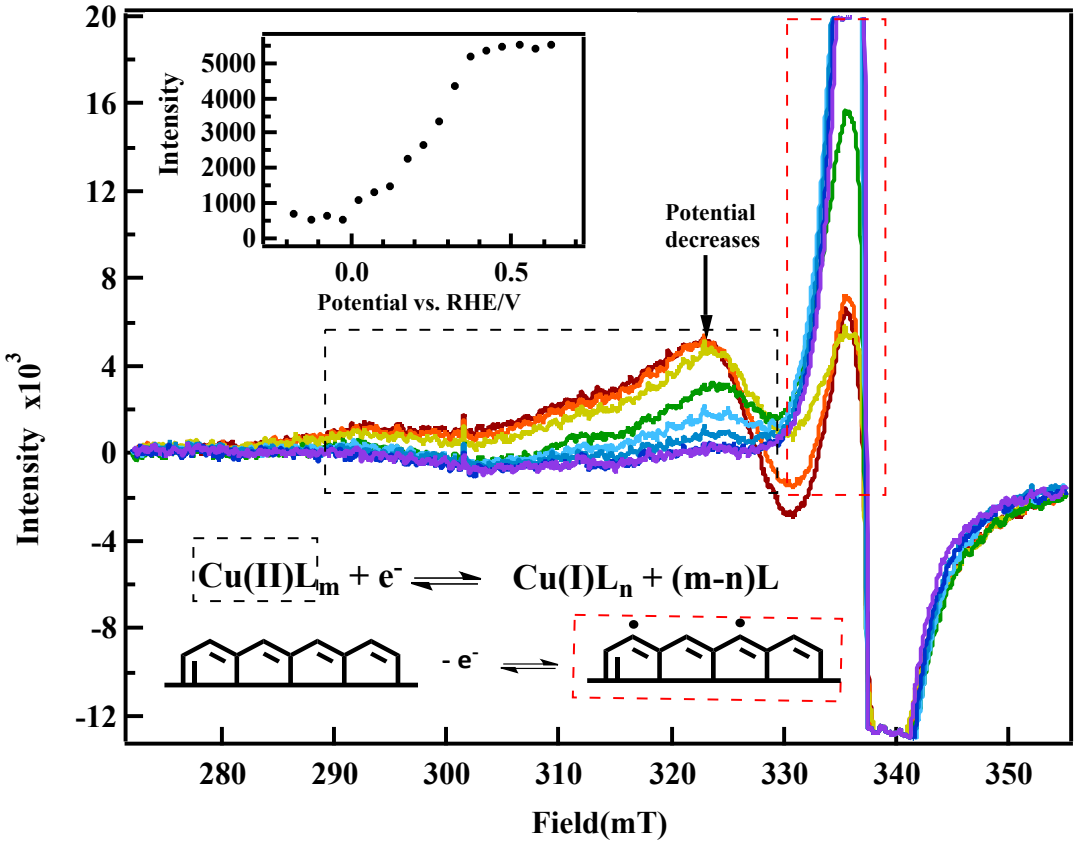


Figure 6.3 EPR spectra measured without applying potential (black), while holding potential of WE 0.57V(red), 0.47V(dark red), 0.37V(cantaloupe), 0.27V(green), 0.17V(blue), 0.07V(Teal), -0.03V(orchid), -0.13V(purple) in N_2 saturated electrolyte for 440s for each potential. L represents DATZ, m and n are the ligand coordination numbers. Inset: intensities of the peaks at the field 320 mT at different potentials after baseline correction. The actual measurement was at potentials ranging from 0.62V to -0.18V with a potential interval of 0.05V. Spectra are shown at a potential interval of 0.1V for the convenience of reading.

The intensity at the first plateau at potentials greater than 0.4V suggests that the same percentage of Cu(II) species exist as Cu(II) in the initial scan (in black in Fig. 6.3) of the cell assembly without applied potential. This excludes the possibility that Cu(II) was reduced to Cu(I) during synthesis. The first plateau also implies that none of Cu(II) in the catalyst is converted to Cu(III) at the potentials studied since the Cu(II) signal does not decrease at the most positive potential investigated.

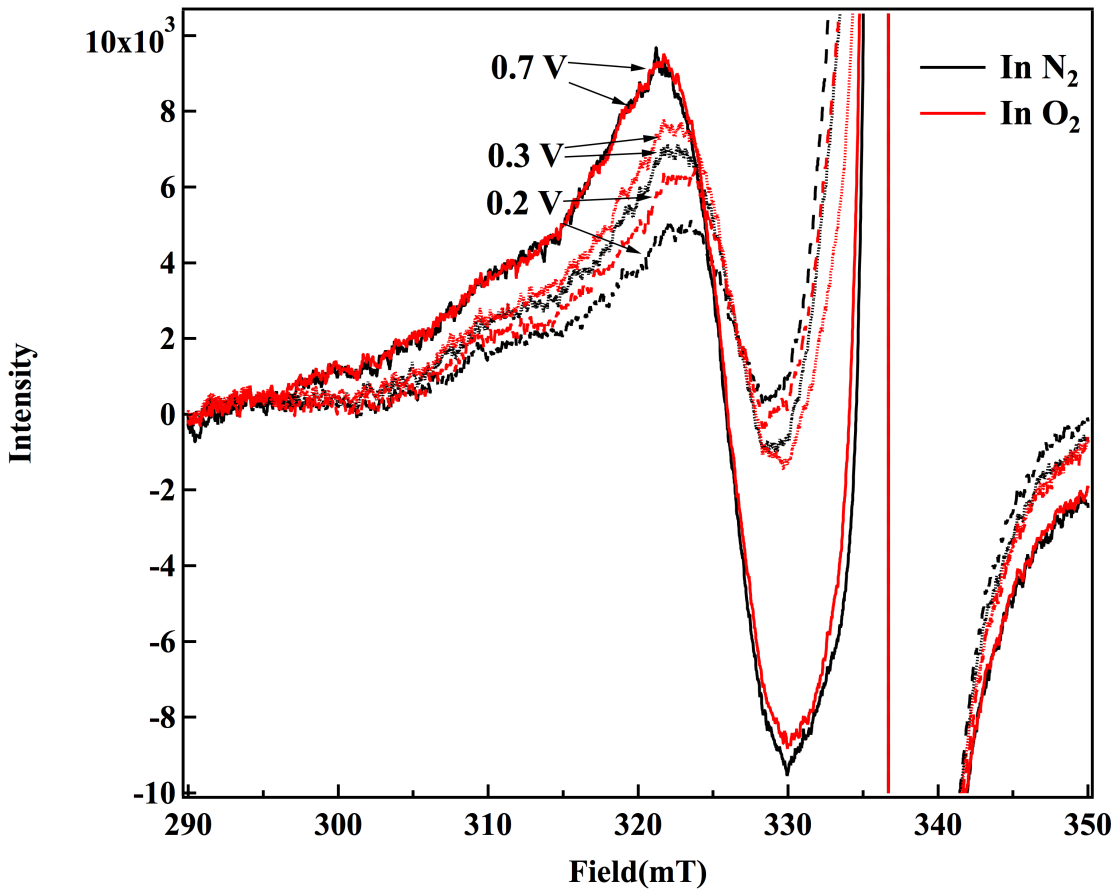


Figure 6.4 EPR spectra in the presence of N_2 and O_2 at potentials 0.7 V, 0.3 V, 0.2 V.

To investigate if there is any difference of Cu(II) amount in the presence and absence of O_2, potential decreases in the order of 0.7, 0.3 and 0.2 V when the electrolyte was satuated with N_2 first. Then same experiment was done when the electrolyte is saturated with O_2. The intensity of the Cu signal at lower potentials is higher in the presence of O_2 than that in presence of N_2, as shown in Fig. 6.4. This could be an indication of Cu species coupling with O_2 species during ORR catalysis. While the presence of singlet O_2 molecules or the oxygen superoxide O_2^- radical have been recognized as a possible intermediate species on adsorbed metal oxide in both solution and solid phase.[177,178] There is no obvious change in the lineshape of the EPR spectra due to the presence of O_2

species. O_2^- has three principal g values around g = 2 and would appear around 3370 G, which is where the strong carbon radical signal occurs. If directly adsorbed on metal, hyperfine-splitting features would be expected to be visible. Additional experiments possibly involving spin trapping methods have to be designed to investigate the existence of the state of the adsorbed oxygen species on the catalyst surface.

6.3.2 Transient EPR experiment

Transient EPR was used to record the EPR signal intensity at the field of maximum intensity of the Cu signal. In this case, the transient EPR signal cannot be baseline corrected. The transient EPR signal is good for observing the trend of changing intensity of paramagnetic species. The change in the EPR signal is not related to a hydrodynamic process, such as diffusion or convection of the species in the electrolyte but to the potential applied on the electrode.

CVs collected in the flat cell described above are shown in Fig. 6.5b and d. Clearly one redox couple can be observed from the CV in the presence of N_2 which can be attributed to Cu(II)/Cu(I). The onset potential calculated at a current density of -5 μA/cm^2 of CVs in O_2 after subtracting CVs in the presence of N_2 is ca. 0.36V, which is close to the onset potential obtained from a conventional three-electrode RDE cell. This is an indication of well-controlled potential on the WE in the cell design. While running the CVs, the EPR spectrometer is held at constant field 320mT to monitor the peak intensities of Cu(II) signal simultaneously. The spectra are indicated in Fig. 6.5a and c. The major difference between the EPR intensity loop in N_2 and O_2 saturated electrolyte is that the Cu(I) is oxidized at a more negative potential in the presence of O_2 during the

anodic scan. This is evidence that Cu(I) binds with O_2 resulting in a more negative oxidizing potential. This is consistent with the mechanism proposed in chapter 3.

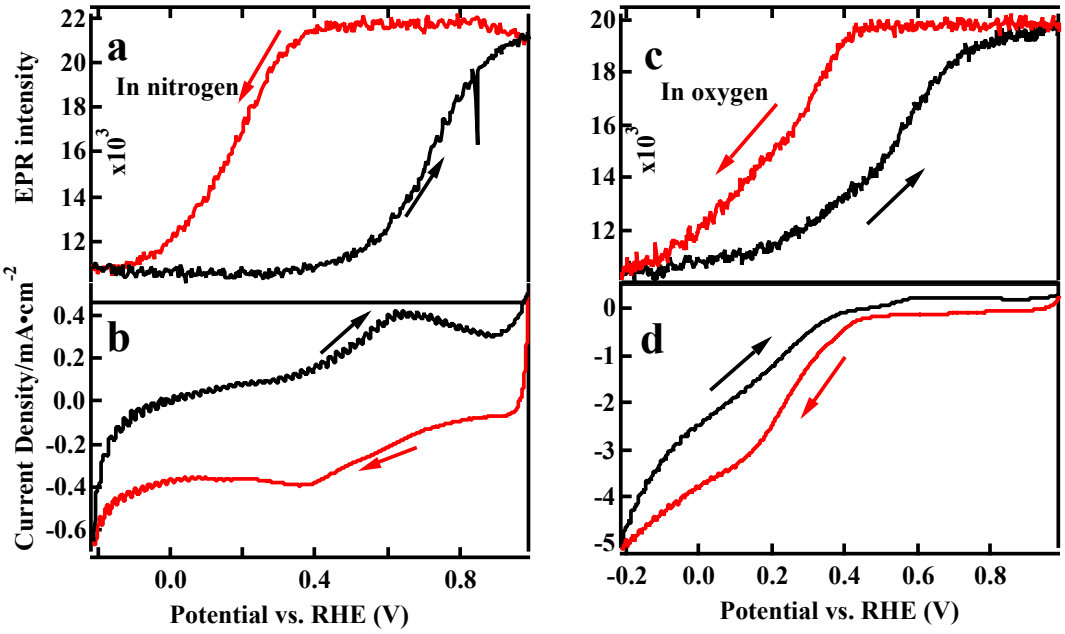
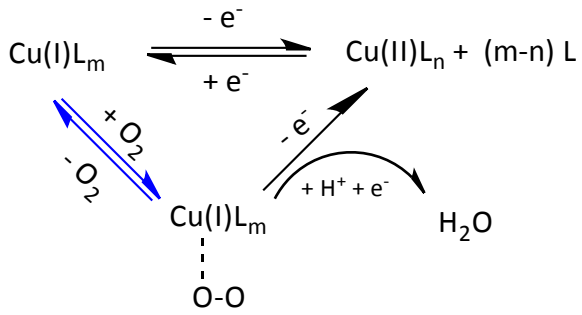


Figure 6.5 a. EPR intensities at constant field 320mT, b. CV at 10mV/s in N_2 saturated 0.1M H_2SO_4 electrolyte. c. EPR intensity at constant field 320mT, d. CV at 10mV/s in O_2 saturated 0.1M H_2SO_4 electrolyte. Scans in red are cathodic scans and in black are anodic scans.

The proposed mechanisms of Cu(II) reduction in the presence of N_2 and O_2 are depicted in scheme 1. In the presence of N_2, Cu(II) and Cu(I) species are reversibly interconverted during a CV. However with O_2 in the electrolyte, the complex formed by $Cu(I)L_m$ bound to O_2 can be oxidized at a more negative potential as indicated by the blue arrows during the anodic scan (L represents DATZ, m and n are the coordination numbers). During the cathodic scan, a slightly smaller slope of decreasing EPR intensity is observed in the potential negative than 0.2V in O_2. This might suggest that a minimum amount of Cu(I) has to be produced to bind O_2 and be oxidized to effectively make up the

Cu(II) consumed by reduction, which leads to assertion that metal reduction is a prerequisite for the O_2 reduction reaction. This agrees with the observation from Figure 6.5c and d that Cu(II) begins to be reduced as the ORR onset potential is approached.



Scheme 6.1 Proposed first step mechanism for Cu(II) and Cu(I) conversion in the presence of N_2 and O_2.

7 Semi-quantitative study using *in situ* electrochemical EPR spectroscopy

7.1 Introduction

In situ electrochemical X-ray adsorption/emission spectroscopy (XA/ES) has emerged as a useful technique to study electrocatalysts for ORR catalysis. Researchers have been trying to explore the electronic structures of electrocatalysts at different potentials in the presence of O_2 and N_2 using this technique.[163,164] Erickson *et al.* found that there is a direct correlation of the Pt-O bonding present to d-state occupancies in their Pt based catalyst from their *in situ* XAS experiment. Niwa *et al.* successfully observed the electronic structure variation of iron under various conditions in their iron phthalocyanine-based catalyst from the operando soft XES spectroscopy.[163,164] However, in their study, limited potentials and work variables were explored due to the demanding measurement conditions of XA/ES, such as time-consuming data collection process and vacuum working environment in addition to the requirement for a synchrotron source. By contrast, *in situ* electrochemical EPR spectroscopy offers a small-scale option for direct study of metallic centers.

In the present case, the electronic features from EPR measurement of Cu(II) based catalyst were explored at more specific conditions, such as more potentials and various O_2 concentrations in the electrolytes. In this chapter, the cell performance was correlated between an *in situ* electrochemical cell and conventional RDE cell. The advantage of the *in situ* electrochemical cell was its capability to measure the Cu(II) amount present in the catalyst while catalyzing the ORR. A semi-quantitative study was conducted to evaluate the reaction order of Cu(I) in ORR catalysis. In order to prove the effectiveness of the *in situ* cell, data obtained from this method was applied to calculate the Tafel slope and

reaction order of O_2 to compare with the results from RDE cell. In other cases, this could help to define the kinetically dominated potential region under flowing electrolyte. The catalyst used in this study is Cu-DATZ based-catalyst, the mechanistic aspects of which have been described in chapter 3 for studies in a conventional RDE cell.

7.2 Experimental procedure

The cell design is described in chapter 6.2. Different oxygen concentrations in the electrolyte were obtained as described in chapter 3. The order of experiment for potential step experiment and transient EPR experiment for each O_2 concentration is: purging O_2 for 40 min, conducting potential step experiment (potential decreases), and transient EPR experiment. The O_2 concentration is increased in the order of 0, 20, 60, 80 and 100%.

7.3 Cell performance comparison of *in situ* electrochemical cell and RDE cell

In the last chapter, the *in situ* electrochemical cell was designed and deployed in the EPR cavity and the catalyst evolution during ORR catalysis was observed. Cu(I) bound with O_2 and shifted the oxidation potential of Cu(I) more negative in the preliminary results. EPR is a sensitive tool to observe the paramagnetic Cu(II) in the catalyst on the electrode. One possible use of this is calculating the reaction order of Cu(I) with the *in situ* electrochemical cell. In chapter 3, the reaction order of Cu(I) was calculated by measuring the Cu(I) amount from the integral of the cathodic peak. This measurement might not be accurate due to the not very well defined redox peaks. Using EPR to calculate the relative amounts of Cu(II) and Cu(I) is achieved via a direct measurement of Cu(II) present in the catalyst. It could be strong evidence for the dual site Cu(I) catalysis mechanism of the ORR on these catalysts if *the situ* measurement agrees with the RDE measurement.

A semi-quantitative calculation of Tafel slope, reaction order of O_2 and Cu species was conducted based on the measurement from the *in situ* electrochemical cell. These results are compared with the data obtained from conventional RDE cell.

Fig. 7.1 shows the CVs obtained in the *in situ* electrochemical cell and RDE cell in N_2 and O_2 saturated electrolyte. With comparable catalyst loading (about 600~800 $\mu g/cm^2$) on the WE electrode, the onset potential of ORR measured in *in situ* cell is about 100 mV lower than that in RDE cell. With a current of 1-4 mA, the cell resistance is about 100-20 Ω, which is one order of magnitude lower than the resistance estimated from the cell designed by Goldberg and Bard.[168] The resistance in the cell could be caused by non-uniform current distribution originated from the non-uniformly coated materials on WE and CE and uncompensated resistance between RE and WE. There is still room for the improvement of cell resistance mentioned above, perhaps by coating electrode materials more evenly and using a new electrode which possesses a relatively smoother surface than those used.

7.4 Transient EPR experiment at different O_2 concentrations

Fig. 7.2 shows the CVs and transient EPR signal intensity at different O_2 concentrations in the electrolyte. As O_2 concentration in the electrolyte increases, the cathodic currents increase and the corresponding transient EPR signals shift upward until O_2 concentration reaches 100%. This suggests that the EPR visible Cu(II) increases as O_2 concentration increases from 0 to 80%. This corresponds with the equilibrium of Cu(II) to Cu(I) shifting to Cu(II) side in the presence of O_2 because O_2 is an oxidant. The anodic scans of EPR signal show the evolution of Cu(I) converting to Cu(II) as potentials scan toward positive values.

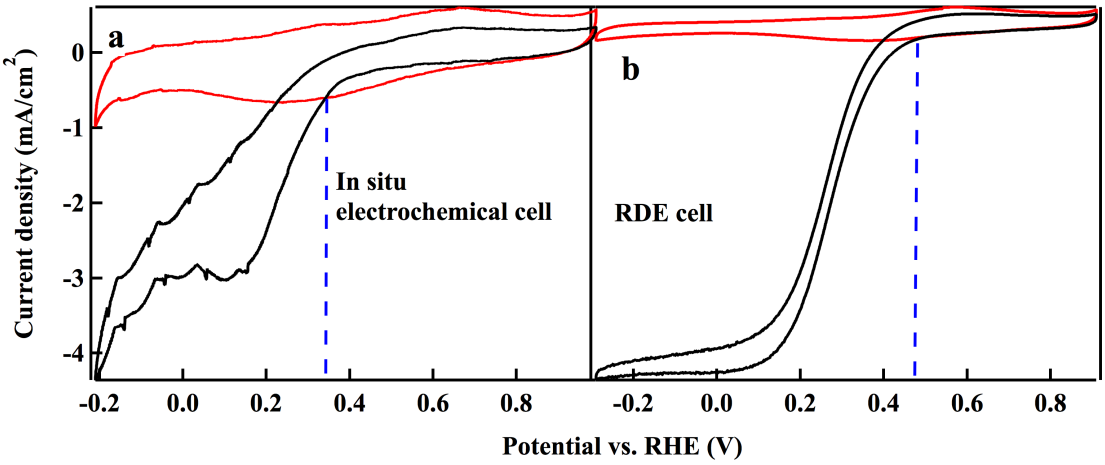


Figure 7.1 a. CVs of *in situ* electrochemical cell in N_2 (in red) and O_2 (in black) saturated 0.1 M H_2SO_4 with a flow rate 0.0325 ml/s at scan rate 50 mV/s. b. CVs of catalyst deposited on glassy carbon rotating disk electrode in N_2 (in red) and O_2 (in black) saturated 0.1 M H_2SO_4 with rotation rate 1600 rmp and scan rate 10 mV/s. The blue dashed lines point out the approximate position of the onset potential of ORR.

When the O_2 concentration is 0%, Cu(I) starts being oxidized around 0.45V. When the O_2 is higher than 0%, Cu(I) is oxidized at potentials negative to 0.45V. The plateau at anodic scan of EPR intensity shrinks at higher O_2 concentration. This indicates that Cu(I) oxidization potentials shift to more negative potentials at higher O_2 concentration, probably due to the simultaneous oxidation of Cu(I) by O_2. The plateau of cathodic scan of EPR intensity at positive potential side extends as O_2 concentration increases, indicating that Cu(II) reduction begins at more negative potentials at higher O_2 concentration. The presence of O_2 facilitates the oxidation of Cu(I) and hinders the reduction of Cu(II). Cu(II) reduction occurs at a more positive potential than O_2 reduction. This suggests that O_2 binds with Cu(I) rather than Cu(II). If Cu(II) bound with O_2 and O_2 hinders the reduction of Cu(II), the electron would have gone to reduce O_2 first. However, the observation that Cu(II) reduction happens at more positive potential than O_2 reduction

contradicts with this assumption that Cu(II) binds with O_2 and O_2 hinders Cu(II) reduction. Therefore Cu(I) binds O_2 species during ORR catalysis.

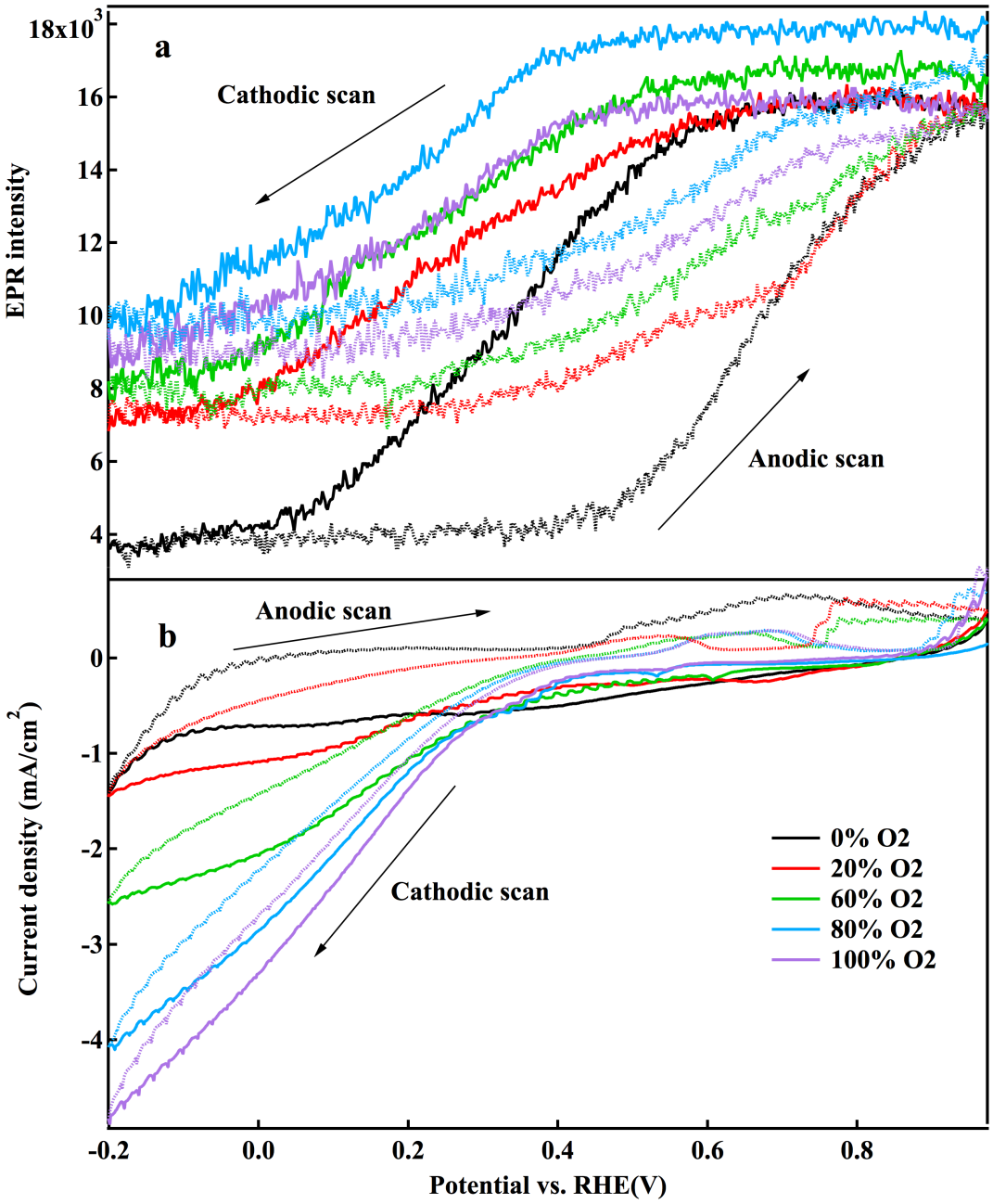


Figure 7.2 a. Transient EPR spectra at constant magnetic field 321 mT and b. CVs from the *in situ* electrochemical cell at different O_2 concentration saturated electrolytes. Solid lines are spectra collected during the cathodic scans of CVs and dotted lines are spectra CVs collected during the anodic scan of CVs. The scan rate is 10mV/s.

Transient EPR is one method to observe the trend of changing EPR signal of paramagnetic species at a constant magnetic field qualitatively. However, it is difficult to see other features like the hyperfine splitting. Also the baseline shifts due to the high modulation amplitude and history effect of the initial state of the catalyst make it difficult to make use of the absolute intensity of the spectra obtained from transient EPR. In later calculations, potential step experiments were used for more quantitative calculations.

7.5 Potential step experiment at different O_2 concentrations

Fig. 7.3 shows the EPR spectra of the cell assembly at different potentials for O_2 concentrations 0, 20, 60, 80 and 100% in the electrolyte. As reported previously, the broad peak around 320 mT is the Cu(II) signal on the WE while the strong peak centered at 335 mT belongs to carbon radicals on the CE.[179] For EPR spectra at each O_2 concentration and different potentials, as the potential decreases, a slight shift of Cu(II) peak position to the high field, a decreasing Cu(II) intensity and a broader carbon signal can be observed. The carbon signal is broaden at lower potentials because there are more carbon radicals produced at the counter electrode to correspond the increasing currents at the working electrode. We cannot completely exclude the possibility that the signal of carbon radicals interferes with Cu(II) signal here since they are still partially overlapped. However, the peak intensity of Cu(II) signal was chosen with care to lower the effect of the signal of carbon radicals as much as possible. When the O_2 concentration is 0%, the Cu(II) is completely reduced at the lowest two potentials since the spectra are flat at where the Cu(II) signal is supposed to be. At higher O_2 concentrations and lowest potentials, the Cu(II) signal is still visible as a little bump. The carbon signal is not broad

enough to cover up the lowest Cu(II) signal. Later in our calculation, the Cu peak intensities are picked at magnetic field lower than 324 mT to be safe.

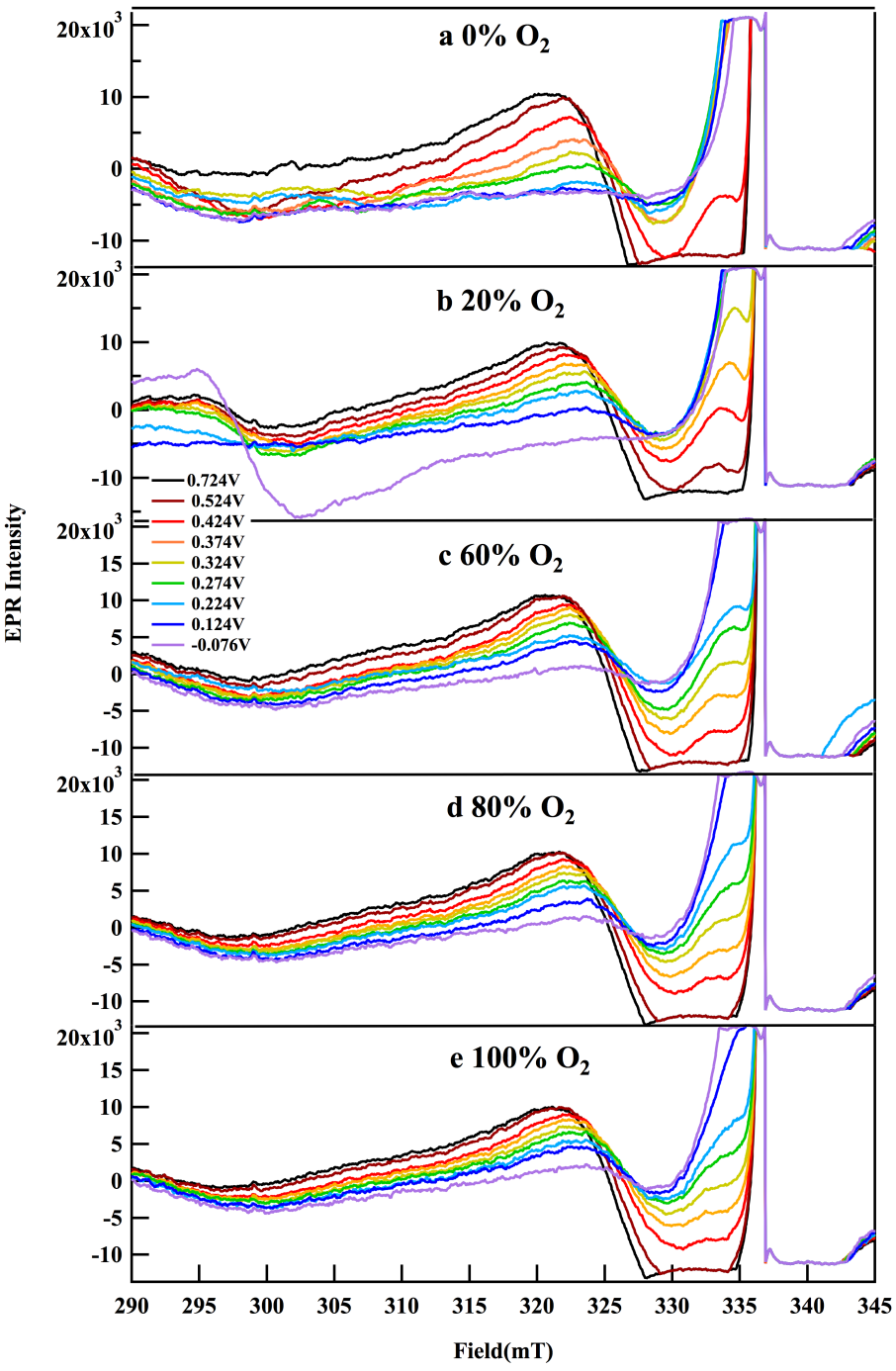


Figure 7.3 EPR spectra collected at different potentials for each O_2 concentration a) 0%, b) 20%, c) 60%, d) 80%, e) 100% in the 0.1 M H_2SO_4. Each potential step is 400 s.

To clearly observe the trend of changing amount of Cu(II) at different potentials and O_2 concentrations, the peak heights of the Cu(II) EPR signal for each potential vs. the potentials were plotted in Fig. 7.4. The peak height of Cu(II) can be taken as a measure of the Cu(II) amount in the catalyst. The amount of Cu(II) in the catalyst decreases as the potential is stepped toward negative values, indicating that Cu(II) is reduced to Cu(I). As the O_2 concentration in the electrolyte increases from 0% to 60%, the Cu(II) amount in the catalyst decreases at a slower rate than potential. The decreasing rates of Cu(II) are similar when the O_2 concentrations are 60%, 80% and 100%. This might suggest that the active sites are saturated in binding O_2.

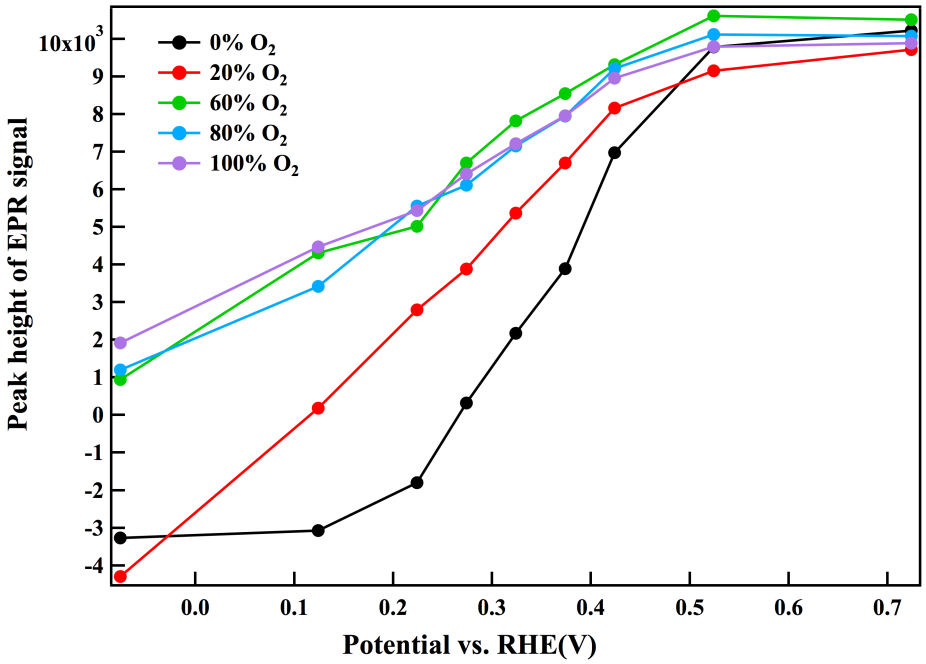


Figure 7.4 Peak heights of EPR signal at different potentials for each O_2 concentration. The corresponding magnetic fields where the peak of Cu(II) EPR signal occurs shift to high field slightly as potential decreases. At 0.724V, the peak height was taken at the magnetic field 321mT. At 0.524V and 0.424V, the peak heights are measured at 322 mT. At the rest of the lower potentials, the peak heights are measured at 323 mT.

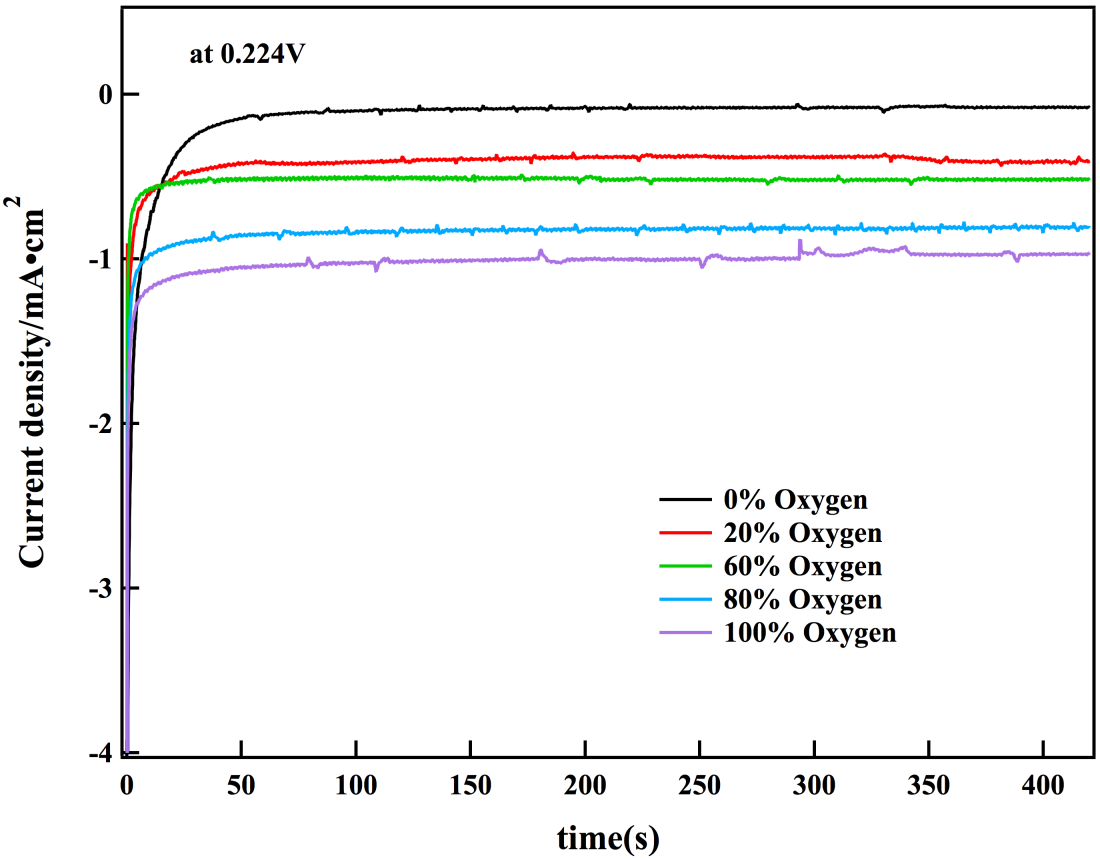


Figure 7.5 Typical current response at each potential for different oxygen concentrations in the electrolyte. the values at potential 0.224 V is shown as an example.

The potential in these experiments varies from a potential at which no ORR takes place (0.724V) to one with both kinetic and mass transport effects present (-0.076V). Fig. 7.5 plots the potential vs. current measured from the *in situ* electrochemical cell. With the flow of electrolyte in the *in situ* cell, the electrode surface was constantly supplied with fresh electrolyte purged with different concentration of O_2. The constant current implies that there is no depletion of O_2 species in the boundary layer of electrolyte on the electrode surface under these steady-state conditions. Both kinetic and mass transport effects contribute to limit the currents obtained. In the inset, plots of the potential vs. logarithm of current density from the data shown in Fig. 7.6 are shown. A turning point of the fitting lines of the points around the potential 0.274V was observed. The slopes

bend more to the logarithm of current density axis as potentials are lower than 0.274V. It is likely that mass transport becomes increasingly important in this potential region due to the increasing consumption of O_2 species at lower potentials. The potential region higher than 0.274 V will be used when calculating the Tafel slope to avoid mass transport effects. The slopes of the fitted lines at potentials higher than 0.274V are listed as mV/decade in the legend of the inset in Fig. 7.6. This catalyst has been well studied previously by RDE. The Tafel slopes calculated from RDE are about 130 mV/decade in chapter 3. The Tafel slope from the *in situ* electrochemical cell shows about 20 to 50mV deviation from the values calculated from RDE cell. At 20% O_2 in the electrolyte, the value deviates more, about 50 mV/decade since the mass transport limitation is more prominent at lower O_2 concentration. At 60%, 80% and 100% O_2, the Tafel slopes are still about 20 to 30 mV/decade lower than the values from RDE cell. This suggests that a constant resistance exists in the *in situ* electrochemical cell since the increasing O_2 concentration did not alleviate the deviation of Tafel slopes at these concentrations. The constant resistance could originate from the non-uniform current distribution between the WE and CE and the uncompensated resistance between the RE and WE. In conclusion, when the O_2 concentration is higher than 60%, the currents are mostly limited by slow kinetics of ORR rather than mass transport besides the constant resistance. This is an important conclusion to support the later calculation using these currents as kinetic currents.

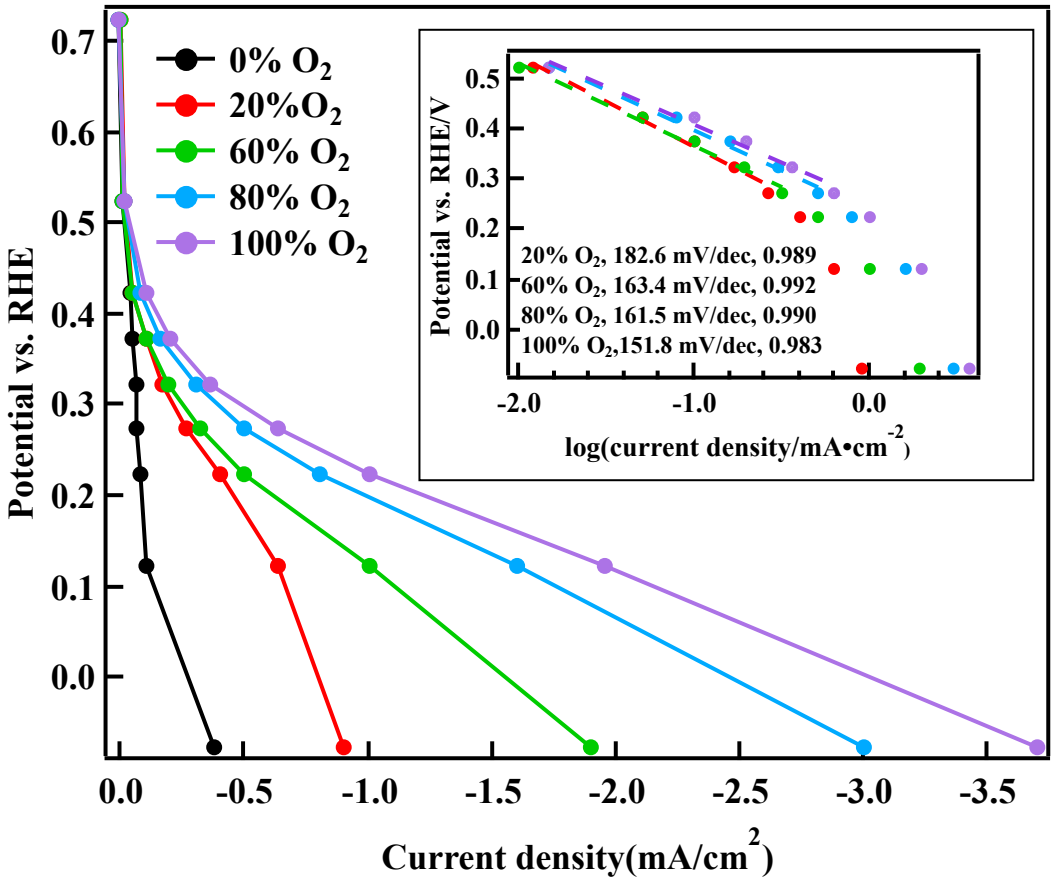


Figure 7.6 Potential vs. current density measured from *in situ* electrochemical cell at different O_2 concentration in the electrolytes. In *in situ* electrochemical cell measurement, the potential is the applied potential step; the current is the constant current reached after first few seconds of the applied potential step. Inset: potential vs. logarithm of current density measured from *in situ* electrochemical cell. Legends show the calculated Tafel slopes in mV/decade and the relative coefficients of the dashed fitting lines.

Similar to classic chemical reaction kinetics, the electrokinetic current can be expressed as a rate relationship, with rate constant and concentration terms for species involved in the RDS, as shown in equation (3.12).

$$J_k = nFkc_{O2}^{m}c_{Cu(I)}^{p}c_{H^+}^{q} \qquad (3.12)$$

The meanings of the symbols were mentioned in section 3.3.

The reaction order of molecular O_2 could be evaluated from the oxygen concentration experiment and provide information about the form of oxygen species involved in RDS. Plots of the logarithm of current density vs. logarithm of O_2 concentration in Fig. 7.6 enable calculation of the reaction order of O_2 in the *in situ* electrochemical cell. The calculation from *in situ* electrochemical cell shows that there is a systematic dependence on the O_2 concentration at potential region investigated. The values are about 1.3 while the value was about 1 from the conventional RDE cell. The higher reaction order measured from the *in situ* electrochemical cell could be caused by the constant resistance mentioned before or could simply reflect uncertainty in defining a purely kinetically limited range. Also, high error would be expected given the small number of data points available for this plot.

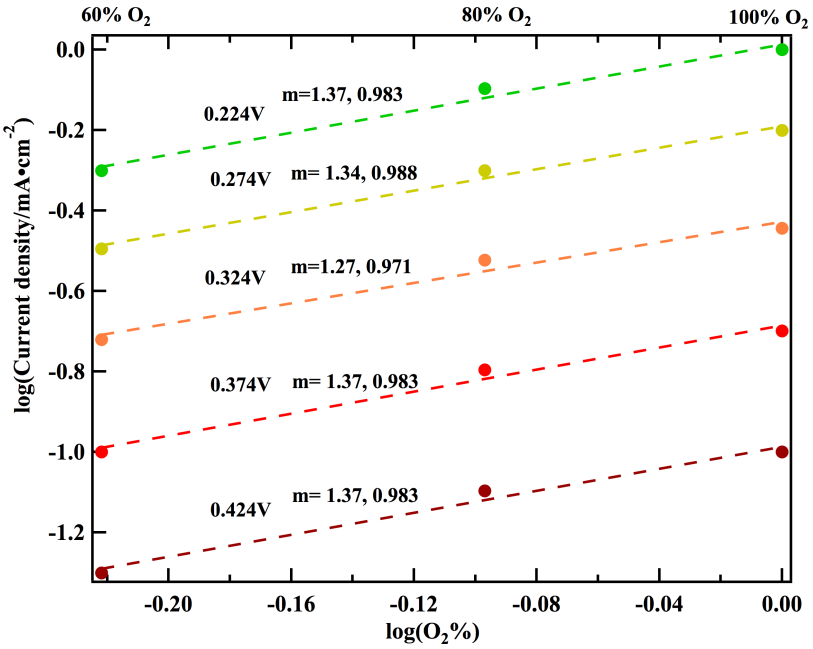


Figure 7.7 Logarithm of current density vs. logarithm of O_2 concentration at kinetic dominant potential region in the *in situ* electrochemical cell. The legend shows the reaction order of m calculated and the relative coefficient of the dashed fitting lines at different potentials.

The Cu(II) signal at different potentials was then used to probe the reaction order of Cu species in the catalysts to explore the Cu species involved in the RDS of ORR catalysis. It is important to note here that the peak height of the Cu(II) signal is related to the relative amount of Cu(II) present. However it is possible that the relationship between peak height and molar concentration is non-linear and must be investigated further. To calculate the reaction order of Cu(I), the logarithm of kinetic current vs. logarithm of Cu(I) intensity was plotted at each O_2 concentration in Fig. 7.7. The value of the reaction order of Cu(I) is listed in the legend of Fig. 7.7. The reaction order of Cu(I) is around 1~2, which suggests that Cu(I) might be involved in RDS as first or second order and binds O_2 in a mononuclear or dinuclear form. This observation agrees with the earlier observation in the transient EPR experiment that Cu(I) species binds with O_2 rather than Cu(II) species.

7.6 Conclusion

A mechanistic study of Cu(II) based electrocatalysts for ORR was conducted using an *in situ* electrochemical EPR cell. The Cu(II) signal evolution during the ORR catalysis was recorded both during a CV and at different constant potentials in the presence of different O_2 concentrations. The transient EPR data during a CV suggests that O_2 binds with Cu(I) in the catalysts rather than Cu(II). The potential step experiment data shows that the kinetically dominated region of the ORR in the *in situ* electrochemical cell is around 0.274 V to 0.524 V for this catalyst. It also reveals that there is a dependence of ORR rate on O_2 concentration in the electrolyte and on Cu(I) species in the catalyst, with reaction orders of 1 and 1~2 respectively.

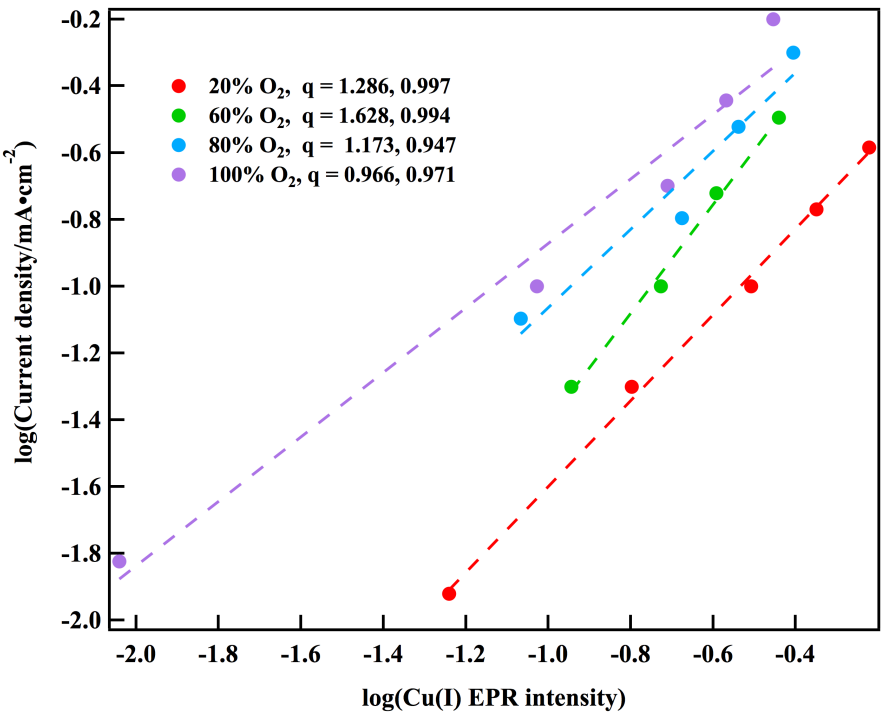


Figure 7.8 Logarithm of current density vs. logarithm of Cu(I) EPR intensity from measurement in *in situ* electrochemical cell at different O_2 concentrations in the electrolytes. The intensity values here are normalized by the intensity at 0.724 V for each O_2 concentration. The legend shows the values of Cu(I) reaction order q and the relative coefficient of the dashed fitting lines.

The accuracy of the cell was intrinsically limited by the electrode position in the flat cell. The position is not fixed for each experiment in the cell. The flat cell was hand made, resulting in non-perfect smooth inner wall. All above factors could affect the flow on the electrode surface. To obtain more accurate quantitative study, the cell structure needs to be optimized in the future.

8 Simultaneous electrochemical EPR study of electrocatalysts before and after pyrolysis

8.1 Introduction

The previous *in situ* study using the simultaneous EPR study has been focused on the non-pyrolyzed catalyst that shows relatively poor performance compared to the pyrolyzed samples. In this chapter, the performance of a non-pyrolyzed catalyst and its pyrolyzed counterpart will be investigated using simultaneous electrochemical EPR spectroscopy. This catalyst as prepared and after pyrolysis are reported recently and are the highest performing synthesized and pyrolyzed Cu catalysts to date.[129]

8.2 Experimental procedure

8.2.1 Catalyst synthesis and electrode preparation

The synthesis of the catalyst as-prepared was described previously and summarized in Fig. 8.1.[129] Basically there are two steps for the synthesis. The first step was to covalently anchor 1,2-benzenedinitrile to the carbon support BP2K though diazotization chemistry. In the second step, the modified carbon was mixed with $Cu(OAc)_2$ and DATZ at 140 ^oC for 4 hours in a microwave reactor to form the catalyst: Cu-TriazoloPhthalocyanine supported on carbon (Cu-TrPc/C). The pyrolyzed sample was obtained in heat treatment at 950 ^oC under a N_2 atmosphere for 1 hour.[129] This chapter will focus on comparing this non-pyrolyzed Cu-TrPc/C sample and its pyrolyzed sample using *ex situ* and *in situ* EPR technique. The *in situ* experiment is to measure the EPR spectra of powder sample in a capillary. The preparation of the capillary is described in chapter 6. The *in situ* EPR measurement is to measure the EPR of sample deposited on the gold foil in the flowing electrolyte. The catalyst loadings for sample as-prepared and for sample after pyrolysis

on the gold foil are about 800 μg/cm^2 and 600 μg/cm^2 respectively. Electrode preparation for *in situ* study is the same as described in Chapter 6.

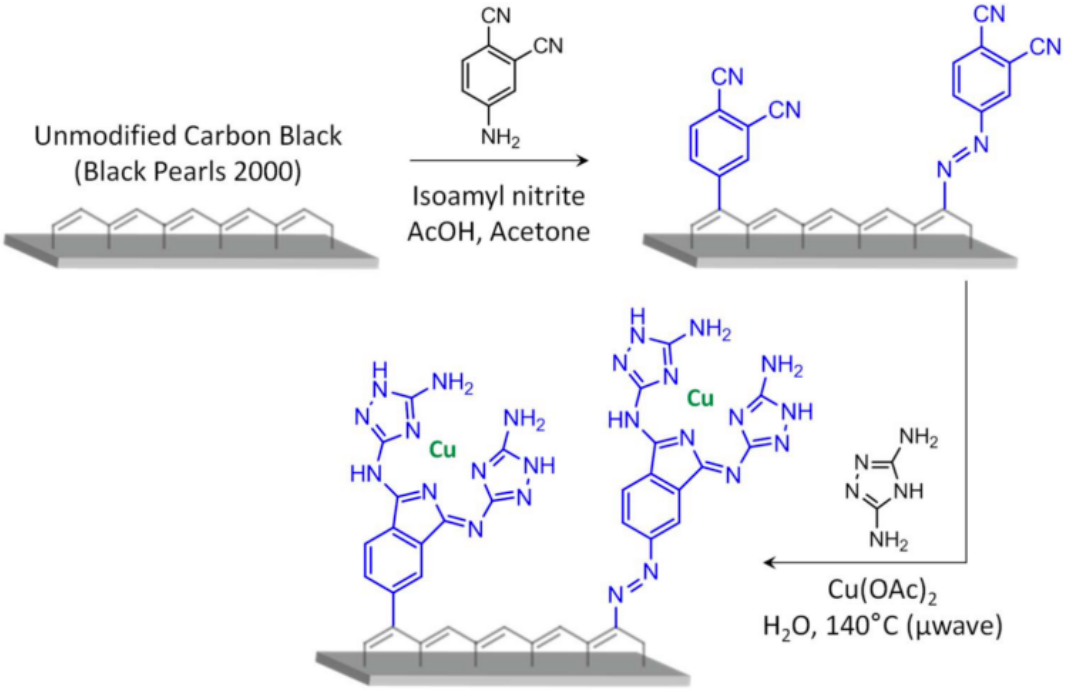


Figure 8.1 Synthesis for non pyrolyzed catalyst[129] (copied from reference 129)

8.2.2 EPR measurement

The method of solid-state measurement is the same as described in chapter 5. The *in situ* measurement was the same as those in Chapter 6. The spectra shown are corrected by the spectra of a empty capillary for solid state measurement and the spectra of flowing electrolyte in flat cell for *in situ* measurement. The order of experiments for the *in situ* measurement is described below for both non-pyrolyzed and pyrolyzed samples: purging gas mixture into the electrolyte for 40 min, conducting potential experiment in an order of decreased potentials and then transient EPR experiment. The O_2 concentrations

increased in an order of 0, 20, 40, 60, 80 and 100%. In the potential step experiment, the holding time for each potential is 200s.

8.3 Solid state study of powder catalyst before and after pyrolysis

The solid state and *in situ* EPR spectra of catalyst before and after pyrolysis are shown in Fig. 8.2. The vertical lines marked the approximate position of $g_{\|}$. When the baseline is flat, the position of $g_{\|}$ is the cross point of the line of the intensity equal to zero with the transition peak. The positions of the g factor of the solid-state measurements for catalyst as-prepared and after pyrolysis and the *in situ* measurement for catalyst as prepared are determined using this method. When the baseline is not flat, the position of the g factor lies at the middle point of the upper and lower isotropic peak summit of the transition. The position of g factor for the *in situ* measurement of catalyst after pyrolysis is determined in this way because the peak of the transition is isotropic ($g_{\perp} = g_{\|}$) (and baseline is not flat.

Table 8.1 shows the g factors and hyperfine tensors of the simulated EPR spectra in Fig. 8.2. Excepting the *in situ* EPR spectrum of pyrolyzed sample, the EPR spectra for the other three cases demonstrate similar features: $g_e < g_{\perp} < g_{\|}$, $A_{\perp} << A_{\|}$. This relationship of g factors implies that the Cu center has octahedral coordination geometry from Table 5.3. The much larger value of $A_{\|}$ than $A_{\perp}$ is reflected by a broad peak shape at the lower field, resulting in unresolved hyperfine splitting The EPR spectrum of *in situ* measurement of catalyst after pyrolysis exhibits an isotropic peak with $g_{\perp} = g_{\|}$=2.19, indicating a tetrahedral coordination geometry of Cu(II) center.[156] The change in the spectra from solid state powder and *in situ* measurements of pyrolyzed catalyst implies the breakdown of octahedral geometry of Cu(II) centers in the presence of electrolyte. In

our later experiments, it was found that this isotropic Cu(II) signal disappears after soaking the electrode in the flowing acid electrolyte for a few hours. This suggests that Cu(II) in the pyrolyzed sample is very unstable on the carbon surface and quickly dissolved in the electrolyte. Though the g values of the solid state EPR of pyrolyzed sample still imply a octahedral coordination geometry, the coordination ligands apparently do not bind as strongly as those in the as-prepared sample. This agrees with the previous statement that heat treatment leads to the breakdown of complex structure, here specifically the structure of triazoloPhthalocyanine. The Cu(II) sites in as-prepared catalyst have similar coordination geometry in both the presence and absence of the electrolyte. Even after the *in situ* EPR experiment, the complex structures were still well preserved, implying stable complex structures for the as prepared sample in acid.

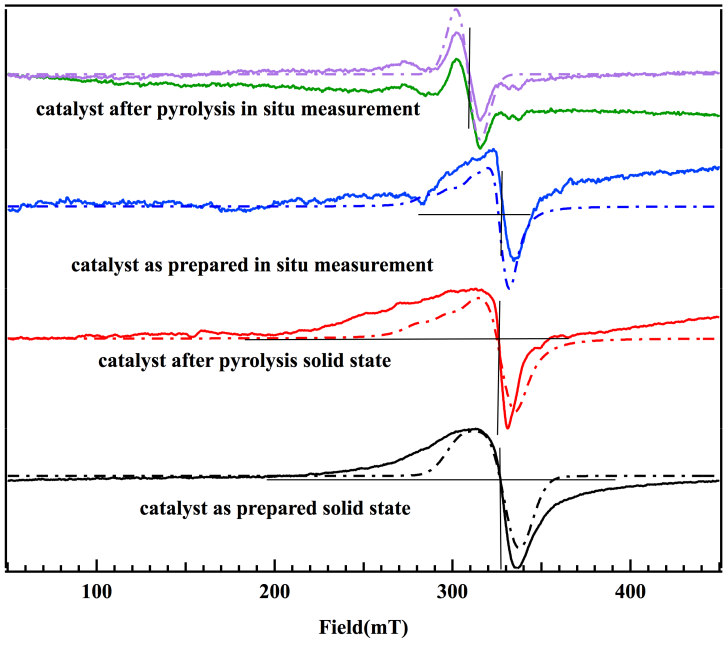


Figure 8.2 Solid state and *in situ* measurement of catalysts before and after pyrolysis at 950 ^{o}C at room temperature. The dashed lines are fitted curves using Matlab R2012b with toolbox Easyspin 4.5.5. For the spectrum in green, the baseline was corrected using first order polynomial, as shown in spectrum in purple with solid.

The fitted parameters including g factors $g_{\perp}$and $g_{\parallel}$ and hyperfine tentors $A_{\perp}$ and $A_{\parallel}$ are listed in Table 8.1.

Table 8.1 g factors $\boldsymbol{g}_{\perp}$and $\boldsymbol{g}_{\parallel}$ and hyperfine tentors $\boldsymbol{A}_{\perp}$ and $\boldsymbol{A}_{\parallel}$ for simulated EPR spectra in Fig. 8.1.

	$g_{\perp}$	$g_{\parallel}$	$A_{\perp}$	$A_{\parallel}$
Catalyst as prepared solid state	2.03	2.22	1	40
Catalyst as prepared *in situ* measurement	2.07	2.22	1	400
Catalyst after pyrolysis solid state	2.07	2.22	1	500
Catalyst after pyrolysis *in situ* measurement	2.19	2.19	10	10

8.4 Potential step experiments with as-prepared catalysts

Potential step experiments were conducted at potentials of 0.7, 0.5, 0.45, 0.4, 0.35, 0.3, 0.2, 0.1, 0, -0.1V for O_2 concentrations of 0, 20, 40, 60, 80, 100% in the electrolyte for catalyst as prepared. The plot for each of the oxygen concentrations is shown in Fig. 8.2. Interestingly, the intensity of the Cu(II) wave increases as potential decreases from 0.7 to 0.35 V and then starts decreasing from 0.35 to -0.1V at O_2 concentration higher than 20% in the electrolyte. When the experiment is performed in N_2 saturated electrolyte, the intensity starts decreasing since 0.1 V. This strongly suggests that there is Cu(I) in the catalyst as prepared.

To clearly observe the trend of Cu(II) intensity at different potentials, the peak intensity was plotted vs. potential for each O_2 concentration in Fig. 8.3. The trend of the peak intensity change is the same as mentioned above.

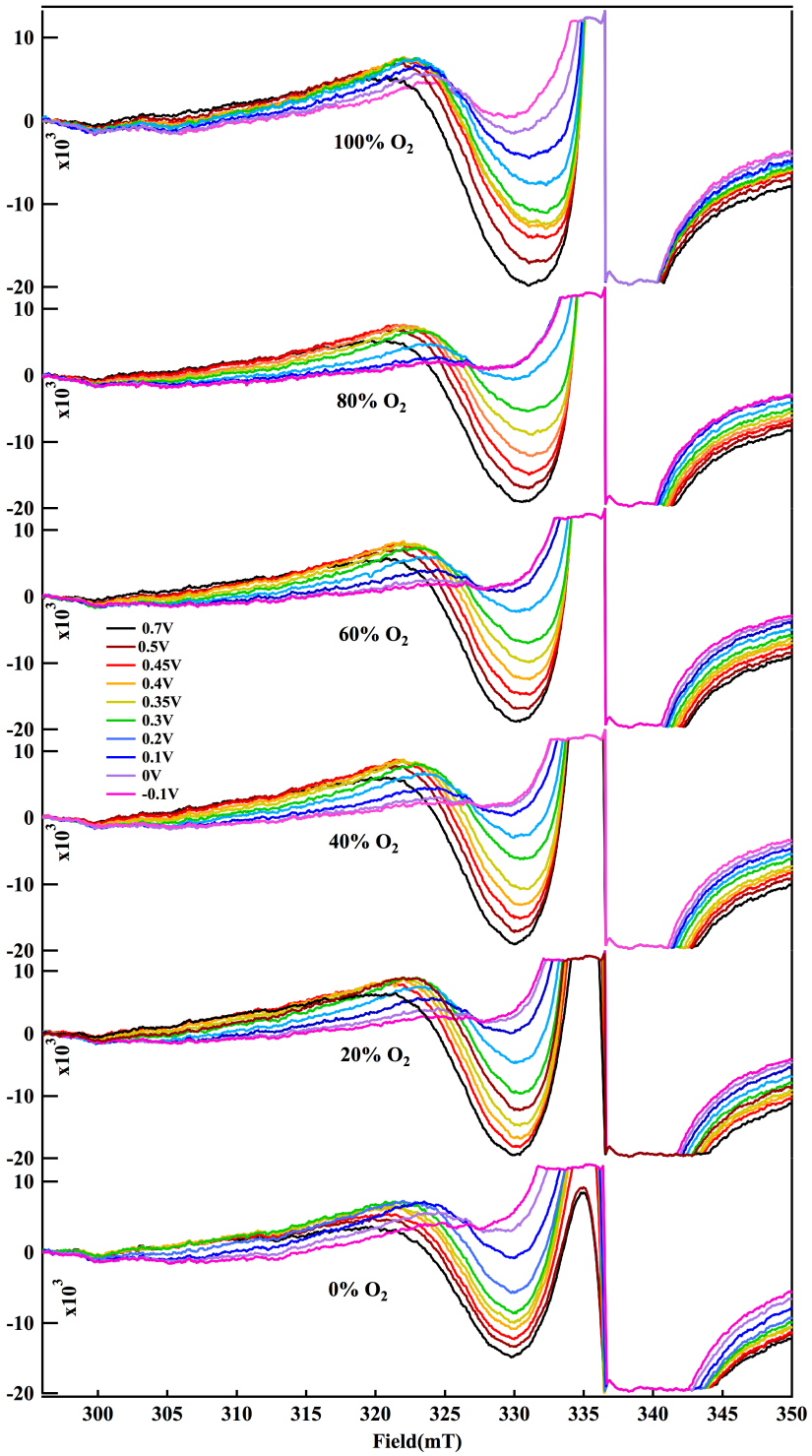


Figure 8.3 EPR spectra at different potentials for each O_2 concentration in the electrolyte

As oxygen concentration changes from 20 to 100%, the intensity of Cu(II) decreases in the potential region from 0.7 to 0.35 V. This disagrees with previous conclusion that when more O_2 is present, Cu(I) binds to more O_2 and is more easily to being oxidized to Cu(II). The intensity of Cu(II) would have increased as O_2 concentration increases. This means there might be other processes going on. The peak intensity of the first scan at 0.7 V exhibits lower intensity as O_2 concentration increases from 20% to 80%. At 0.7 V, there is no ORR occurring according to the report that onset potential of ORR is 0.52 V.[129] Every time the potential is returned to 0.7V, the peak intensity decreases. This is unrelated to O_2 since no ORR takes place at this potential but is likely related to the decomposition of the catalyst. When there is no O_2, the intensity of Cu(II) is the lowest at this potential. This might be explained by the decomposition of unstable Cu(II) species on the electrode at the beginning.

At potentials lower than 0.35V, the peak intensity decreases as O_2 concentration increases from O_2 concentration 20% to 80%. This trend is plausible since the decomposition of the catalyst makes the sum of Cu(II) visible to EPR lower at the beginning of each potential step. However, when O_2 concentration is increased to 100%, the intensity of Cu(II) decreases much more slowly and exhibits the highest intensity. This is because the 100% O_2 makes the Cu(I) more inclined to be oxidized to Cu(II) at these potentials. This makes up for the loss of Cu(II) at the beginning due to partially decompostion. This catalyst is different from Cu(II)-DATZ based catalyst in several aspects. Cu(I) is observed in the catalyst at the beginning since the Cu(II) intensity increases and then decreases as potential decreases for each O_2 concentration. The partially decomposition of Cu(II) in the catalyst is more obvious than for Cu-DATZ

based catalyst . This statement is supported by the observation the Cu(II) intensity decreases at no-ORR-reaction potential region as O_2 concentration increases. For both catalysts, Cu(I) binding with O_2 is observed at 100% O_2 concentration.

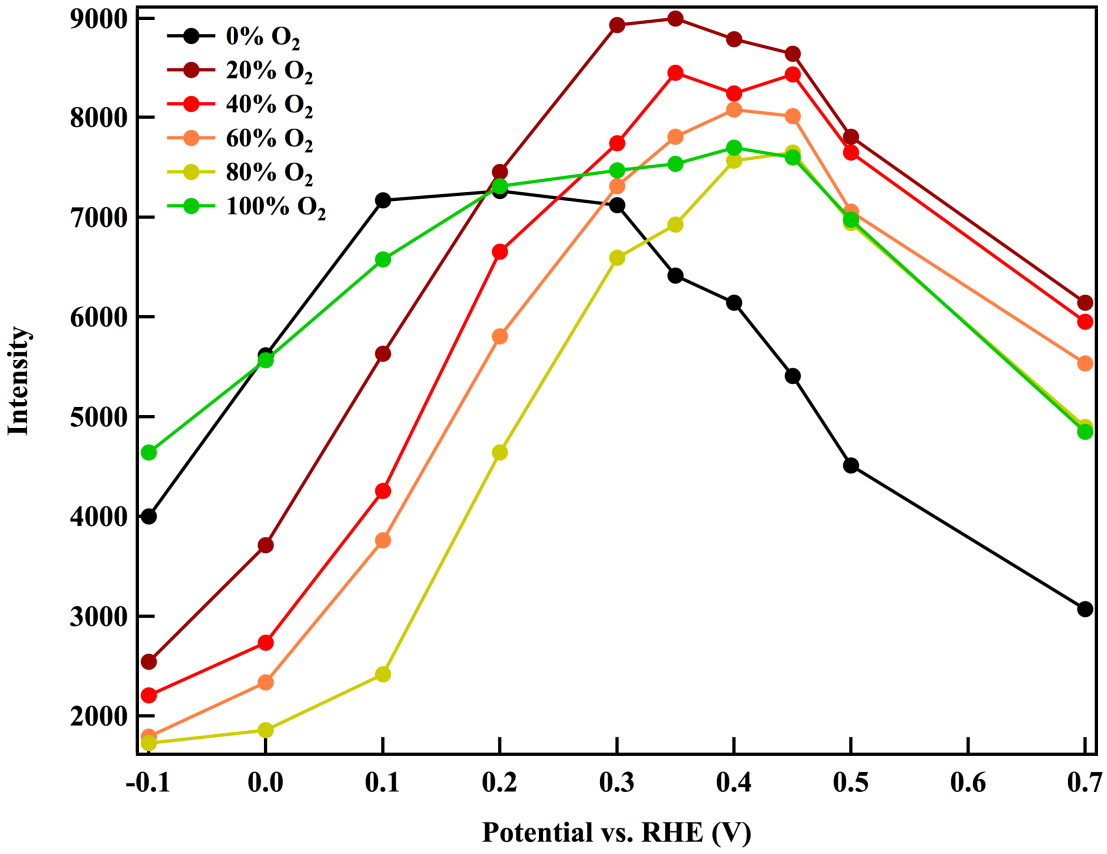


Figure 8.4 Peak intensity of Cu(II) EPR signal at different potentials. The magnetic field for taking the values of peak intensities are: 321 mT for potential 0.7 to 0.45 V, 322 mT for potential 0.4 to 0.2 V and 323.5 mT for potential 0.1 to -0.1 V.

8.5 Potential step experiments probing the catalyst after pyrolysis

Potential step experiments were conducted at potentials of 1.1, 0.9, 0.8, 0.7, 0.6, 0.4, 0.3, 0.2, 0.2, 0.1, -0.1V for O_2 concentration 0, 20, 40, 60, 100% in the electrolyte for catalysts after pyrolysis at 950 ^{o}C. At 0% O_2 concentration and 1.1 V, the Cu(II) signal is the peak centered around 308 mT. As mentioned in the work of *Goenaga et al.*, metallic

Cu and Cu(I) oxide are detected after pyrolysis at 950 ^{o}C from their XRD data.[129] Since both species have no EPR signal, this peak is attributed to Cu(II) in the catalyst. As the potential decreases, the intensity does not decrease gradually. After the potential steps to the lowest potentials, the intensity of Cu(II) stays at 0 for all other potentials steps. This indicates that the coordination environment of Cu(II) in the catalyst as prepared was destroyed during pyrolysis and Cu(II) probably exists in the catalyst after pyrolysis as an independent entity without being held by ligand strongly to the carbon surface. As it is reduced to Cu(I), copper species are dissolved in the electrolyte. To ascertain that the Cu(II) can be dissolved in the electrolyte without applied potentials, the electrode was soaking in the flowing electrolyte for hours. The Cu(II) signal also disappeared. Since EPR could not observe the metallic Cu and Cu(I) oxide in the catalyst, it is unknown about their existence after being in the electrolyte for some time. However, it is certain that the catalyst as prepared and catalyst after pyrolysis possess different active sites in catalyzing ORR. The catalytic centers in pyrolyzed samples are not Cu(II).

CVs were run at each O_2 concentration after the potential step experiment for the pyrolyzed sample. The plot is shown in Fig. 8.5. The decomposition of the Cu(II) centers does not have an dramatic impact on the CVs since the ORR current increases gradually with increasing O_2 concentration, similar to the situation at different O_2 concentrations in RDE experiment. The limiting current is reached at potential lower than 0.3 V, suggesting the depletion of O_2 on the electrode surface. The observations support the statement that Cu(II) in this catalyst is not responsible for the ORR activity.

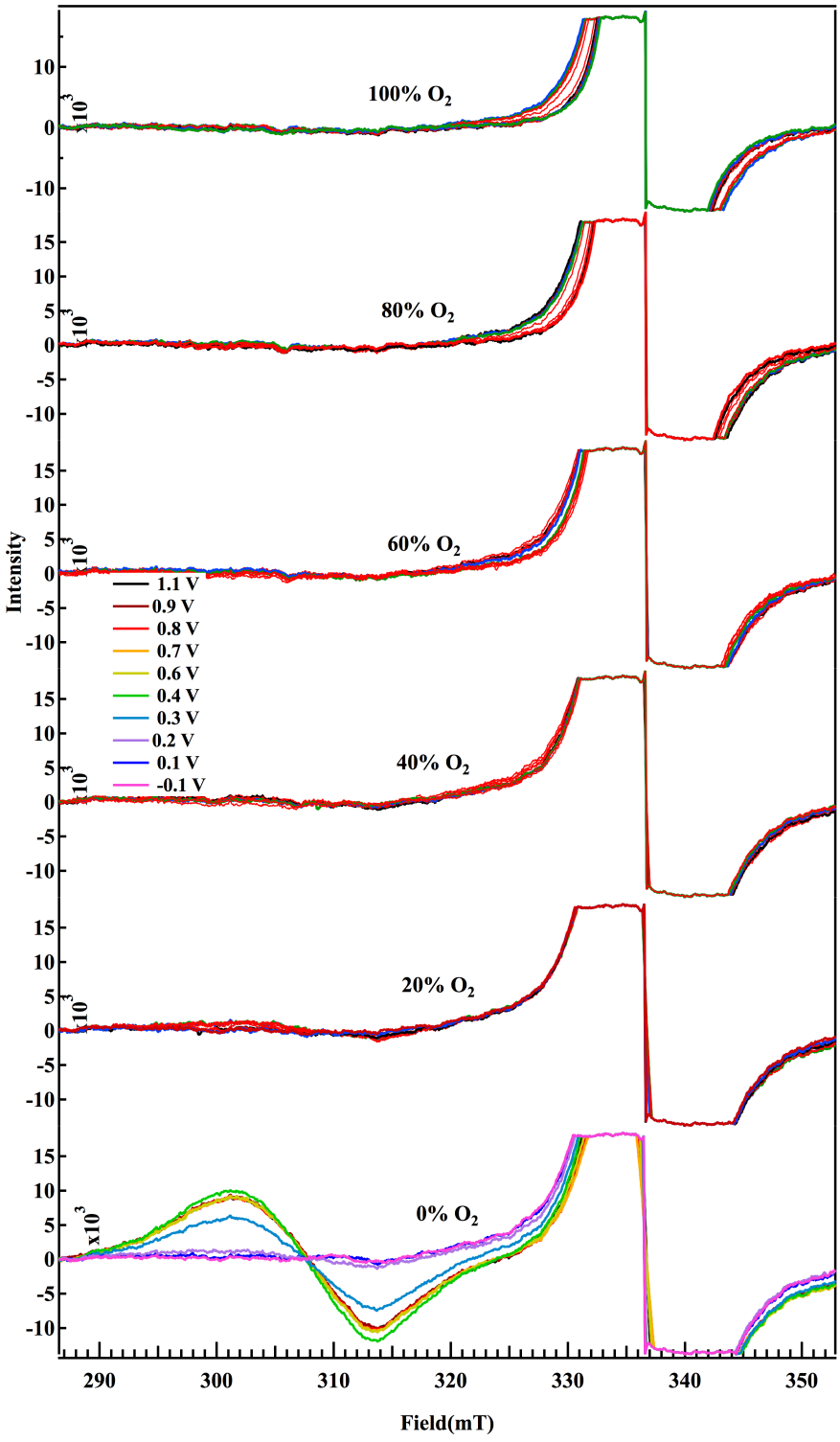


Figure 8.5 EPR spectra of catalyst after pyrolysis at 950 ^{o}C at different potentials for each O_2 concentration in the electrolyte

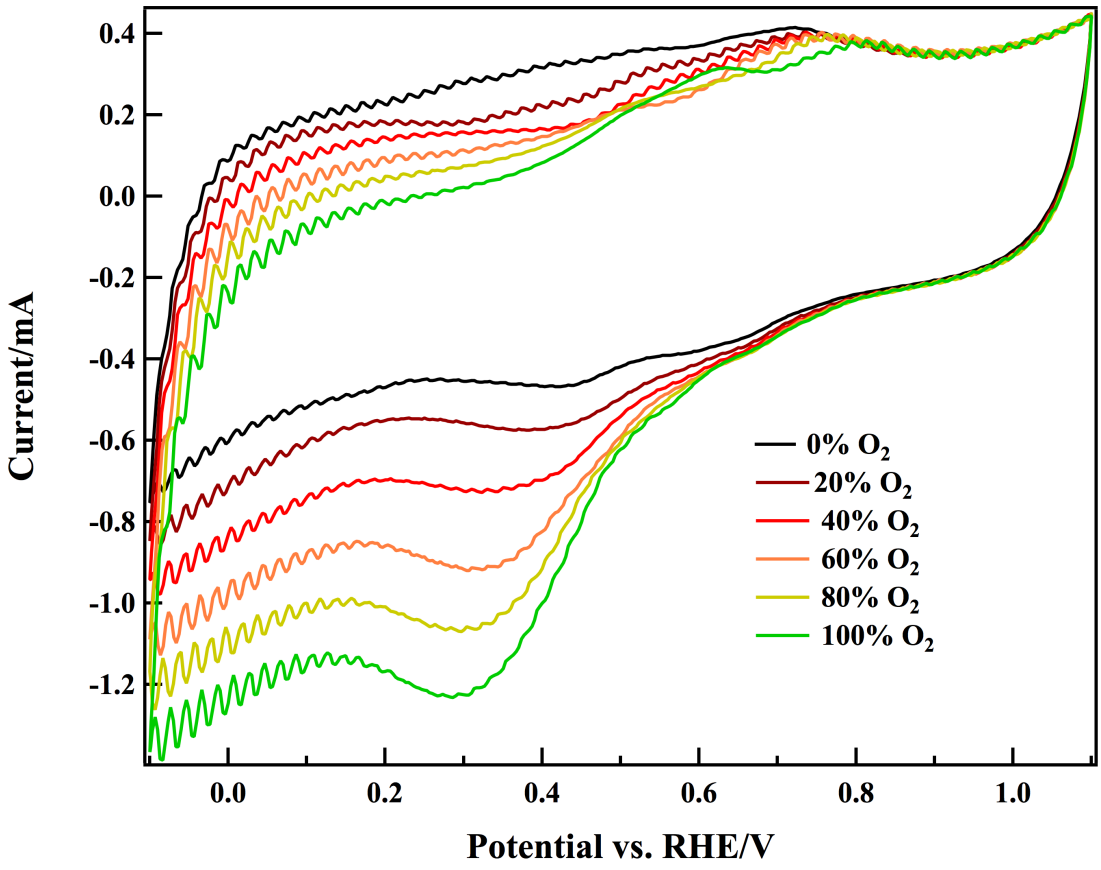


Figure 8.6 CVs of the pyrolyzed catalyst at different O_2 concentrations in the *in situ* electrochemical cell.

8.6 Conclusions

In this chapter, the behavior of a synthesized catalyst and its analogous pyrolyzed sample in the *in situ* electrochemical cell in EPR was investigated. The Cu(II) EPR intensity of the non-pyrolyzed sample Cu-TrPc/C increases first as potential decreases from no ORR reaction potential region, which is around 0.7V. This is different from the Cu(II)-DATZ-based catalyst. The intensity then decreases as potential is further decreased from 0.35 V to -0.1V. At this potential region, the Cu(II) EPR intensity shows similar behavior to that observed for the Cu-DATZ-based catalyst in that the presence of O_2 tends to facilitate the oxidation of Cu(I) into Cu(II), resulting in a higher Cu(II)

intensity at high O_2 concentration for the same potential. Regarding the pyrolyzed sample, the solid state EPR showed octahedral coordination of Cu(II) based on the simulated g values that $g_e < g_\perp < g_\parallel$. In the electrolyte, EPR spectra display an isotropic Cu(II) center with a tetrahedral coordination geometry based on isotropic g values: $g_\perp = g_\parallel = 2.19$. In the simultaneous electrochemical study of this catalyst, the Cu(II) peak disappeared after a few potential steps, indicating the decomposition of the catalyst and loss of Cu(II) from the catalyst. These as prepared and pyrolyzed samples demonstrate different catalytic centers from this *in situ* study. Cu(II) is responsible for the ORR activity in the synthesized sample but this is not true for the pyrolyzed sample.

9 Summary

This work was set out to explore the ORR mechanism by Cu-1,2,4-triazole complex-based electrocatalysts and use what we have learn to guide us to synthesize better metal complex-based electrocatalysts. Developing non-noble metal-based electrocatalysts to replace the costly Pt based catalysts is a necessity in order to realize the commercialization of PEMFCs. Most efforts now have been focused on pursuing high ORR performance of non-noble catalysts by severe thermal and chemical treatment.[56,73] Comparable ORR performance to Pt based catalyst has been achieved among non-noble metal complex-based electrocatalysts, especially for transition metals.[10,43] However, the fundamental understanding of catalytic sites leading to the improved ORR performance remains unclear. This hinders the further improvement of non-noble metal-based catalyst. Cu-1,2,4-triazole complex-based catalysts were chosen due to their significance in biomimetic study and well-preserved structures resulting from simple chemical synthesis.[41,42,92] My study intended to add to answers to the following questions:

1) What do the catalytic sites look like in our Cu-1,2,4-triazole complex-based catalysts?
2) What is the ORR mechanism by Cu-1,2,4-triazole complex-based catalysts?
3) How could above knowledge be used to synthesize better electrocatalysts?

To answer the first question, It is necessary to learn the compositions of the Cu-1,2,4-triazole complex-based catalysts and understand the role of each composition since they are heterogeneous systems with complications between the compositions.

9.1 Carbon surface functionalities improve the ORR performance of the Cu-DATZ-based electrocatalyst.

Oxygen functional groups on carbon support introduced by soaking BP2K in H_2O_2/H_2SO_4 solution significantly enhanced the onset potential and limiting current of ORR activity of Cu-DATZ based catalyst, as shown in Fig. 2.3. The number of electron transferred is above 3.9 in the limiting current region, indicating an increased selectivity towards 4e- pathway. Similar conclusions have been made among pyrolyzed catalysts: a carbon support with oxygen functionality on the surface after pyrolysis demonstrated better complex dispersion ability towards metal complexes. It is also possible that oxygen groups act as the axial ligand in the complex structure leading to a change in the energy splitting of d orbitals in the metal. This could have a favorable effect on the ORR performance.

Introduction of nitrogen in pyrolyzed non precious metal catalysts has been an effective method to improve the ORR performance.[73,76,78] In Cu-DATZ based catalyst, DATZ was covalently bonded to the carbon surface through diazotization chemistry. After 2000 cycles in O_2 saturated electrolyte at potential 0.2-0.7, the immobilized catalyst demonstrated a smaller decrease in half-wave potential than does an adsorbed catalyst which has no chemical bond between DATZ and carbon support, as shown in Fig. 2.4. In our case, the covalently bonded ligand binds metal to form bonded complexes on carbon surface. This improves the stability of the catalyst.

9.2 Cu complexes adsorbed on the carbon surface are mainly responsible for the ORR activity of Cu-1,2,4-triazole-based electrocatalysts.

In chapter 5, the ATR-FTIR spectra show that major peaks of the complexes formed in solution phase are similar to those formed with corresponding ligands on modified carbon support. This is strong evidence that the Cu complexes are adsorbed on the carbon surface. Cu-DATZ complexes have been deposited on the RRDE disk electrode to test its ORR activity. However, the complexes dissolved in the electrolyte quickly after several cycles before any electrochemical tests can be conducted. Therefore the complex structures are more stable on carbon surface. In Fig. 2.5, it shows either only Cu(II) or only DATZ ligand on the carbon surface cannot lead to a high ORR performance. Without DATZ ligand, the adsorbed Cu(II) on carbon surface decreased dramatically. The electroactive ones are even less according to the much smaller reduction peak in the CV. The modified carbon support demonstrated certain ORR activity but it is much weaker than that with Cu-DATZ complexes on the surface. Therefore Cu complexes adsorbed on carbon surface take major responsibility for the ORR activity of Cu-1,2,4-triazole based electrocatalysts.

Several features of the Cu-triazole complexes were identified to contribute active ORR catalytic sites. Catalysts synthesized with OAc^- as anion in the Cu salts exhibit higher ORR activity than other anions explored. In the synthesis, the optimal Cu:DATZ ratio was 1:2. The presence of either less or more DATZ could not lead to optimal ORR activity due to formation of not enough complexes or complexes precipitate not adsorbed on carbon surface. However the actual Cu:DATZ ratio in the formed complexes in the catalyst was calculated as 2:1 according to the elemental analysis. Another feature of the

Cu complexes is the octahedral coordination geometry with large hyperfine splitting at the axial direction compare to the perpendicular direction. This was recognized in immobilized Cu-DATZ based catalyst that demonstrates the highest performance among the five substituted triazoles investigated. This feature was also identified in the non-pyrolyzed CuTrPc based catalyst in chapter 8. All these features could be the references when making catalysts of this kind.

9.3 Dinuclear Cu(I)-Cu(I) active site binds O_2 molecule.

One of the major conclusions from this study is the dinuclear Cu(I) binding site with O_2 molecule during the ORR catalysis by Cu-DATZ based electrocatalyst. The dinuclear Cu(I) requires that two Cu(I) ions are located in proximity in the catalyst. The distance should be larger than O=O bond length (1.21 Å) to break the O=O bond. Cu(I) binding with the O_2 molecule was directly observed from the *in situ* electrochemical EPR technique. In the presence of O_2, Cu(I) oxidation potential decreased compared to the situation in the absence of O_2. From MO theory, two d_{z2} orbitals filled with electrons of Cu(I) have a similar orbital symmetry to the antibonding π^* orbital of O_2 (Fig. 1.6) and are more likely to form a bond if we agrees the conclusion that the center metal is an electron donor and O_2 molecule is an electron acceptor from many researchers' work.[26,28] The existence of dinuclear Cu(I) was experimentally proved by calculating the reaction order of Cu(I) as about 2 from catalyst loading experiment and semi-quantitative analysis from *in situ* electrochemical EPR technique. The reaction order of O_2 molecule is calculated around 1 from oxygen concentration experiment, indicating one O_2 molecule involved in the RDS reaction.

9.4 Electron donating groups are favorable for ORR performance of Cu-3-amino-5-substitutents-1,2,4-triazole based catalysts

Five Cu(II)-3-amino-5-substituent-1,2,4-triazole complex based electrocatalysts were investigated to study the effect of electronic structures on the ORR performance of these catalysts. According to the calculation of Mulliken charges on N1 and N2 on triazole ring of optimized structures, electron donating group such as $–NH_2$ enables stronger binding between ligand and Cu(II) and the corresponding catalyst demonstrated higher ORR activity and selectivity. Electron withdrawing groups such as $–COOCH_3$ and –SH have inverse effect on ligand and Cu(II) binding and results in low ORR activity of their catalysts. However, besides electronic properties, the steric effect and other binding sites of the substituents should also be considered. Great care should be taken when choosing substituents to make sure they have similar sizes and no side reactions.

9.5 Catalysts as prepared and after pyrolysis studied in Goenaga *et al*'s work demonstrate different catalytic centers for ORR. Cu(II) centers are responsible for the catalytic sites in catalyst as prepared while Cu(II) decomposed rapidly and was not observed for this sample after pyrolysis during ORR catalysis.

In the catalyst as synthesized, the major Cu complex is Cu(II)-triazolophthalocyanine (Fig. 8.1). The Cu(II) evolution during ORR catalysis was observed from potential step experiment using *in situ* electrochemical EPR technique. XRD spectra did not show any diffraction peak from Cu(I) and Cu(0).[129] All of this evidence supports the inference that Cu(II) sites are responsible for the catalytic centers in non-pyrolyzed Cu(II) complex based catalyst. Meanwhile, in the pyrolyzed sample, the Cu(II) peak of the EPR spectra

disappears quickly after soaking the electrode in the electrolyte for some time. These Cu(II) in the pyrolyzed sample are unstable and may be not strongly coordinated. The CVs in different oxygen concentrations did not show a dramatic change due to the loss of Cu(II) in the catalyst. XRD spectra showed that the major Cu forms in pyrolyzed sample are Cu_2O and metallic Cu, both of which are EPR silent.[129] These excluded the possibility that Cu(II) is the catalytic center for the pyrolyzed sample.

The above findings lead to the following conclusions about the role of different compositions in non pyrolyzed catalysts: the catalytic centers are central Cu coordinated by nitrogens from the triazole ring. Active Cu centers have to be reduced to Cu(I) and two Cu(I) in proximity work together to bind one O_2 molecule. Functionalities on carbon supports are either co-bonded to the centeral metal to affect the energy level of d orbitals or facilitate the dispersion of metal complexes on the carbon surface. The activity of Cu centers can be affected directly by varying the electronic properties of peripheral nitrogens.

The ORR mechanism by non-noble metal-based catalysts has been a subject of extensive debate for decades. The RDS, which is the focus of most researchers, might be derived by combining multiple experimental and theoretical evidences. The reaction intermediates in other fast steps are impossible to know due to the limitation of detection techniques. Based on our findings, the RDS of ORR mechanism by Cu-DATZ-based catalyst is proposed in reaction (3.20).

$$2Cu(I) + O_2 + H^+ \rightarrow Cu(I)_2O_2H \qquad (3.20)$$

The reaction order of two Cu(I) and one O_2 molecule has been discussed in section 9.3. The number of H^+ in above reaction cannot be calculated experimentally. It is reasonable

to protonate superoxide $Cu(I)_2O_2^-$ since the reaction occurs in acidic media. The Tafel slope calculated in the kinetic region is about 130 mV/decade, close to the value 118 mV/decade value derived from Butler-Volmer equation for a one electron transfer process. This one electron transfer occurs in the fast step before the RDS to turn Cu(II) into Cu(I).

9.6 H_2O_2 is an intermediate in the ORR, rather a side product for Cu-DATZ based catalyst.

Catalyst loading experiment showed that increased catalyst loading on the disk electrode results in decreased amount of H_2O_2 detected at the ring electrode. This is strong evidence that H_2O_2 is an intermediate in ORR, indicating a 2×2 reaction pathway. The increased catalyst loading could cause a decreased collection efficiency by the ring electrode due to the increased thickness of catalyst layer. However, at our catalyst loadings investigated, collection efficiency is not a major factor but rather the increased tortuosity causes the decreasing H_2O_2 detected at the ring electrode. As the produced H_2O_2 travels through the catalyst layer, H_2O_2 has a higher chance of running into active sites and turns into water with a thicker catalyst layer. If H_2O_2 were a side product from certain undesired catalytic sites, the production of H_2O_2 would have increased as the catalyst loading increases since more undesired catalytic sites would have occurred with more catalyst loading. The onset potential of H_2O_2 by Cu-DATZ based catalyst is higher than that of O_2. Addition of H_2O_2 in the electrolyte improves the onset potential for the ORR. These evidences support the idea that H_2O_2 is involved in the fast step in the mechanism as an intermediate.

In the future synthesis, efforts could be focused on developing multinuclear Cu complexes. This could increase the density of available Cu(I) in the complexes to bind more O_2 molecule. Another strategy is varying the electronic properties of ligand coordinating the central metal. Complexes with better-defined complex structures after introducing functional groups will lead to a more systematic variation in their ORR performance.

List of References

1. M. A. Thorseth, C. E. Tornow, E. C. M. Tse, and A. a. Gewirth, *Coord. Chem. Rev.*, **257**, 130–139 (2013) http://linkinghub.elsevier.com/retrieve/pii/S001085451200077X.

2. O. Antoine, Y. Bultel, and R. Durand, *J. Electroanal. Chem.*, **499**, 85–94 (2001) http://linkinghub.elsevier.com/retrieve/pii/S0022072800004927.

3. D. B. Sepa, M. V. Vojnovic, and A. Damjanovic, *Electrochim. Acta*, **26**, 781–793 (1981).

4. R. Jasinski, *Nature*, **201**, 1212–1213 (1964).

5. E. S. S. A, H. Behret, H. Binder, G. Sandstede, and G. G. Scherer, **117**, 29–42 (1981).

6. F. Beck, *J. Appl. Electrochem.*, **7**, 239–245 (1977).

7. A. Elzing, V. A. Putten, W. Visscher, and E. Barendrecht, *Jounal Electroanal. Chem.*, **233**, 99–112 (1987).

8. A. Kozawa, V. E. Zilionis, and R. J. Brodd, *J. Electrochem. Soc.*, **117**, 1470–1474 (1971).

9. M. Lefèvre, E. Proietti, F. Jaouen, and J.-P. Dodelet, *Science*, **324**, 71–4 (2009) http://www.ncbi.nlm.nih.gov/pubmed/19342583.

10. E. Proietti et al., *Nat. Commun.*, **2**, 416 (2011) http://www.ncbi.nlm.nih.gov/pubmed/21811245.

11. G. Wu, K. L. More, C. M. Johnston, and P. Zelenay, *Science*, **332**, 443–7 (2011) http://www.ncbi.nlm.nih.gov/pubmed/21512028.

12. N. Mano, V. Soukharev, and A. Heller, *J. Phys. Chem. B*, **110**, 11180–7 (2006) http://www.ncbi.nlm.nih.gov/pubmed/16771381.

13. C. F. Blanford, R. S. Heath, and F. A. Armstrong, *Chem. Commun. (Camb).*, 1710–2 (2007) http://www.ncbi.nlm.nih.gov/pubmed/17457416.

14. L. Hussein et al., *Biosens. Bioelectron.*, **26**, 4133–8 (2011) http://www.ncbi.nlm.nih.gov/pubmed/21543222.

15. M. Pita et al., *J. Phys. Chem. C*, **115**, 13420–13428 (2011) http://pubs.acs.org/doi/abs/10.1021/jp203643h.

16. M. Sosna, J.-M. Chrétien, J. D. Kilburn, and P. N. Bartlett, *Phys. Chem. Chem. Phys.*, **12**, 10018–26 (2010) http://www.ncbi.nlm.nih.gov/pubmed/20577679.

17. A. Zloczewska, M. Jönsson-Niedziolka, J. Rogalski, and M. Opallo, *Electrochim. Acta*, **56**, 3947–3953 (2011) http://linkinghub.elsevier.com/retrieve/pii/S0013468611002337.

18. S.-K. Lee et al., *J. Am. Chem. Soc.*, **124**, 6180–93 (2002) http://www.ncbi.nlm.nih.gov/pubmed/12022853.

19. E. I. Solomon, *J. Inorg. Biochem.*, **47**, 29 (1992) http://linkinghub.elsevier.com/retrieve/pii/0162013492841002.

20. E. I. Solomon, U. M. Sundaram, and T. E. Machonkin, *Chem. Rev.*, **96**, 2563–2605 (1996).

21. T. Tsukihara et al., *Science*, **272**, 1136–44 (1996) http://www.ncbi.nlm.nih.gov/pubmed/8638158.

22. H. S. Carr and D. R. Winge, *Acc. Chem. Res.*, **36**, 309–16 (2003) http://www.ncbi.nlm.nih.gov/pubmed/12755640.

23. R. Boulatov, *Pure Appl. Chem.*, **76**, 303–319 (2004).

24. K. Piontek, M. Antorini, and T. Choinowski, *J. Biol. Chem.*, **277**, 37663–9 (2002) http://www.ncbi.nlm.nih.gov/pubmed/12163489.

25. H. Jahnke, M. Schonborn, and G. Zimmermann, *Top. Curr. Chem.*, **61**, 133–181 (1976).

26. H. Alt, H. Binder, and G. Sandstede, *J. Catal.*, **28**, 8–19 (1973).

27. M. Zerner, M. Gouterman, and H. Kobayashj, *Theor. Chim Acta(Berlin)*, **6**, 363–400 (1966).

28. H. Zhu, S. J. Paddison, and T. a. Zawodzinski, *Electrochim. Acta*, **101**, 293–300 (2013) http://linkinghub.elsevier.com/retrieve/pii/S0013468612019676.

29. Z. Shi and J. Zhang, *J. Phys. Chem. C*, **111**, 7084–7090 (2007) http://pubs.acs.org/cgi-bin/doilookup/?10.1021/jp0671749.

30. L. M. Proniewicz, I. Paeng, and K. Nakamoto, *J. Am. Chemitry Soc.*, **113**, 3294–3303 (1991).

31. J. H. Zagal, *Coord. Chem. Rev.*, **119**, 89–136 (1992).

32. M. S. Thorum, J. Yadav, and A. a Gewirth, *Angew. Chem. Int. Ed. Engl.*, **48**, 165–7 (2009) http://www.ncbi.nlm.nih.gov/pubmed/19035597.

33. J.-P. Randin, *Electrochim. Acta*, **19**, 83–85 (1974).

34. N. Kobayashi, M. Fujihira, K. Sunakawa, and T. Osa, *Jounal Electroanal. Chem.*, **101**, 269–273 (1979).

35. C. C. L. . McCrory, X. Ottenwaelder, T. D. P. Stack, and C. E. D. Chidsey, *J. Phys. Chem. A*, **111**, 12641–12650 (2007).

36. M. Savy, P. Andro, and C. B. et G. Magner, *Electrochim. Acta*, **18**, 191–197 (1973).

37. Â. H. Zagal, M. Gulppi, M. Isaacs, G. Cacardenas-Jiron, and M. Aguirre, *Electrochim. Acta*, **44**, 1349–1357 (1998).

38. E. E. Chufán, S. C. Puiu, and K. D. Karlin, *Acc. Chem. Res.*, **40**, 563–72 (2007) http://www.ncbi.nlm.nih.gov/pubmed/17550225.

39. E. Aznar et al., *Eur. J. Inorg. Chem.*, **2006**, 5115–5125 (2006) http://doi.wiley.com/10.1002/ejic.200600711.

40. A. Ray, S. Mitra, and G. M. Rosair, *Inorg. Chem. Commun.*, **11**, 1256–1259 (2008) http://linkinghub.elsevier.com/retrieve/pii/S1387700308002992.

41. R. Zhang et al., *Cryst. Growth Des.*, **4**, 3735–3644 (2008).

42. J. G. Haasnoot, *Coord. Chem. Rev.*, **200-202**, 131–185 (2000) http://linkinghub.elsevier.com/retrieve/pii/S0010854500002666.

43. G. Wu, K. L. More, C. M. Johnston, and P. Zelenay, *Science*, **332**, 443–7 (2011) http://www.ncbi.nlm.nih.gov/pubmed/21512028.

44. K. Lee et al., *Electrochim. Acta*, **54**, 4704–4711 (2009) http://linkinghub.elsevier.com/retrieve/pii/S0013468609004794.

45. M. Yuasa et al., *Chem. Mater.*, **17**, 4278–4281 (2005).

46. Y. Feng, T. He, and N. Alonso-Vante, *Chem. Mater.*, **20**, 26–28 (2007) http://dx.doi.org/10.1021/cm7024763.

47. R. A. Sidik and A. B. Anderson, *J. Phys. Chem. B*, **110**, 936–941 (2005) http://dx.doi.org/10.1021/jp054487f.

48. E. Vayner, R. A. Sidik, A. B. Anderson, and B. N. Popov, *J. Phys. Chem. C*, **111**, 10508–10513 (2007) http://dx.doi.org/10.1021/jp072056m.

49. D. Xia et al., *J. Power Sources*, **177**, 296–302 (2008) http://www.sciencedirect.com/science/article/pii/S037877530702558X.

50. F. Yin, K. Takanabe, J. Kubota, and K. Domen, *J. Electrochem. Soc.*, **157**, B240 (2010) http://jes.ecsdl.org/cgi/doi/10.1149/1.3267041.

51. S. Izhar, M. Yoshida, and M. Nagai, *Electrochim. Acta*, **54**, 1255–1262 (2009) http://linkinghub.elsevier.com/retrieve/pii/S0013468608010463.

52. A. Ishihara et al., *Electrochem. Solid-State Lett.*, **8**, A201 (2005) http://esl.ecsdl.org/cgi/doi/10.1149/1.1865612.

53. A. Ishihara, Y. Ohgi, K. Matsuzawa, S. Mitsushima, and K. Ota, *Electrochim. Acta*, **55**, 8005–8012 (2010) http://linkinghub.elsevier.com/retrieve/pii/S0013468610003749.

54. S. C. Barton, J. Gallaway, and P. Atanassov, *Chem. Rev.*, **104**, 4867–86 (2004) http://www.ncbi.nlm.nih.gov/pubmed/15669171.

55. Z. Chen, D. Higgins, A. Yu, L. Zhang, and J. Zhang, *Energy Environ. Sci.*, **4**, 3167 (2011) http://xlink.rsc.org/?DOI=c0ee00558d.

56. C. W. B. Bezerra et al., *Electrochim. Acta*, **53**, 4937–4951 (2008) http://linkinghub.elsevier.com/retrieve/pii/S0013468608002193.

57. R. Othman, A. L. Dicks, and Z. Zhu, *Int. J. Hydrogen Energy*, **37**, 357–372 (2012) http://linkinghub.elsevier.com/retrieve/pii/S0360319911020192.

58. G. Liu, X. Li, J.-W. Lee, and B. N. Popov, *Catal. Sci. Technol.*, **1**, 207 (2011) http://xlink.rsc.org/?DOI=c0cy00053a.

59. B. Wang, *J. Power Sources*, **152**, 1–15 (2005) http://linkinghub.elsevier.com/retrieve/pii/S0378775305008864.

60. D. Scherson et al., *Electrochim. Acta*, **31**, 1247–1258 (1986).

61. D. Ohms et al., *J. Power Sources*, **38**, 327–334 (1992) http://linkinghub.elsevier.com/retrieve/pii/037877539280122R.

62. a. L. Bouwkamp-Wijnoltz et al., *J. Phys. Chem. B*, **106**, 12993–13001 (2002) http://pubs.acs.org/doi/abs/10.1021/jp0266087.

63. F. Charreteur, F. Jaouen, S. Ruggeri, and J. Dodelet, *Electrochim. Acta*, **53**, 2925–2938 (2008) http://linkinghub.elsevier.com/retrieve/pii/S0013468607013655.

64. G. Lalande, *Electrochim. Acta*, **40**, 2635–2646 (1995) http://linkinghub.elsevier.com/retrieve/pii/001346869500104M.

65. M. Ferrandon et al., *J. Phys. Chem. C*, **116**, 16001–16013 (2012) http://pubs.acs.org/doi/abs/10.1021/jp302396g.

66. J. Herranz et al., *J. Phys. Chem. C*, **115**, 16087–16097 (2011).

67. E. Yeager, *Electrochim. Acta*, **29**, 1527–1537 (1984) http://linkinghub.elsevier.com/retrieve/pii/0013468684850069.

68. S. Gupta, D. Tryk, I. Aldred, and E. Yeager, *J. Appl. Electrochem.*, **19**, 19–27 (1989).

69. M. Lefèvre, J. P. Dodelet, and P. Bertrand, *J. Phys. Chem. B*, **106**, 8705–8713 (2002) http://pubs.acs.org/doi/abs/10.1021/jp020267f.

70. R. Bashyam and P. Zelenay, *Nature*, **443**, 63–6 (2006) http://www.ncbi.nlm.nih.gov/pubmed/16957726.

71. U. I. Kramm et al., *J. Electrochem. Soc.*, **158**, B69 (2011) http://link.aip.org/link/JESOAN/v158/i1/pB69/s1&Agg=doi.

72. F. Jaouen et al., *ACS Appl. Mater. interfaces*, **1**, 1623–39 (2009) http://www.ncbi.nlm.nih.gov/pubmed/20355776.

73. D. Villers, X. Jacques-Bédard, and J.-P. Dodelet, *J. Electrochem. Soc.*, **151**, A1507 (2004) http://jes.ecsdl.org/cgi/doi/10.1149/1.1781611.

74. F. Charreteur, S. Ruggeri, F. Jaouen, and J. Dodelet, *Electrochim. Acta*, **53**, 6881–6889 (2008) http://linkinghub.elsevier.com/retrieve/pii/S0013468607015204.

75. F. Jaouen, F. Charreteur, and J. P. Dodelet, *J. Electrochem. Soc.*, **153**, A689 (2006) http://link.aip.org/link/JESOAN/v153/i4/pA689/s1&Agg=doi.

76. F. Jaouen, M. Lefevre, J. P. Dodelet, and M. Cai, *J. Phys. Chem. B*, **110**, 5553–5558 (2006).

77. N. P. Subramanian et al., *J. Power Sources*, **157**, 56–63 (2006) http://linkinghub.elsevier.com/retrieve/pii/S0378775305008992.

78. H. Wang, R. Côté, G. Faubert, D. Guay, and J. P. Dodelet, *J. Phys. Chem. B*, **103**, 2042–2049 (1999) http://pubs.acs.org/doi/abs/10.1021/jp9821735.

79. P. Ehrburger, a Mongilardi, and J. Lahaye, *J. Colloid Interface Sci.*, **91**, 151–159 (1983) http://linkinghub.elsevier.com/retrieve/pii/0021979783903223.

80. P. Gouerec, M. Savy, and J. Riga, *Electrochim. Acta*, **43**, 743–753 (1998).

81. L. Wu et al., *Chem. Commun. (Camb).*, **46**, 6377–9 (2010) http://www.ncbi.nlm.nih.gov/pubmed/20697640.

82. G. Liu, X. Li, P. Ganesan, and B. N. Popov, *Appl. Catal. B Environ.*, **93**, 156–165 (2009) http://linkinghub.elsevier.com/retrieve/pii/S0926337309003798.

83. V. Nallathambi, J.-W. Lee, S. P. Kumaraguru, G. Wu, and B. N. Popov, *J. Power Sources*, **183**, 34–42 (2008) http://linkinghub.elsevier.com/retrieve/pii/S037877530800952X.

84. Z. Chen, D. Higgins, A. Yu, L. Zhang, and J. Zhang, *Energy Environ. Sci.*, **4**, 3167 (2011) http://xlink.rsc.org/?DOI=c0ee00558d.

85. F. R. Brushett et al., *J. Am. Chem. Soc.*, **132**, 12185–7 (2010) http://www.ncbi.nlm.nih.gov/pubmed/20715828.

86. P. Vasudevan, N. Mann, and S. Tyagi, *Transit. Met. Chem.*, **15**, 81–90 (1990).

87. S. Yoshimoto, A. Tada, K. Suto, and K. Itaya, *J. Phys. Chem. B*, **107**, 5836–5843 (2003) http://pubs.acs.org/doi/abs/10.1021/jp027825a.

88. R. Guilard, J.-M. Barbe, S.-J. Dong, and Q.-S. Qiu, *Chinese J. Chem.*, **10**, 309–319 (1992) http://dx.doi.org/10.1002/cjoc.19920100404.

89. Q. He et al., *J. Power Sources*, **216**, 67–75 (2012).

90. J. Zhang and F. C. Anson, *Electrochim. Acta*, **38**, 2423–2429 (1993).

91. J. Zhang and F. C. Anson, *J. Electroanal. Chem.*, **348**, 81–97 (1993) http://linkinghub.elsevier.com/retrieve/pii/002207289380124Z.

92. E. Aznar et al., *Eur. J. Inorg. Chem.*, **2006**, 5115–5125 (2006) http://doi.wiley.com/10.1002/ejic.200600711.

93. M. Eguchi et al., *Polymers (Basel).*, **4**, 1645–1656 (2012) http://www.mdpi.com/2073-4360/4/4/1645/.

94. C.-M. Lai, J.-C. Lin, F.-P. Ting, S.-D. Chyou, and K.-L. Hsueh, *Int. J. Hydrogen Energy*, **33**, 4132–4137 (2008) http://linkinghub.elsevier.com/retrieve/pii/S036031990800520X.

95. D. Lee and S. Hwang, *Int. J. Hydrogen Energy*, **33**, 2790–2794 (2008) http://linkinghub.elsevier.com/retrieve/pii/S0360319908003261.

96. L. Lee, thesis, University of Canterbury (2011).

97. A. Devadoss and C. E. D. Chidsey, *J. Am. Chem. Soc.*, **129**, 5370–1 (2007) http://www.ncbi.nlm.nih.gov/pubmed/17425323.

98. F. Jaouen et al., *ACS Appl. Mater. Interfaces*, **1**, 1623–39 (2009) http://www.ncbi.nlm.nih.gov/pubmed/20355776.

99. L. Welte et al., *Adv. Mater.*, **21**, 2025–2028 (2009) http://doi.wiley.com/10.1002/adma.200802886.

100. G. Wang et al., *Int. J. Hydrogen Energy*, **35**, 11245–11253 (2010) http://linkinghub.elsevier.com/retrieve/pii/S0360319910013753.

101. D. Pantea, H. Darmstadt, S. Kaliaguine, and C. Roy, *Appl. Surf. Sci.*, **217**, 181–193 (2003) http://linkinghub.elsevier.com/retrieve/pii/S0169433203005506.

102. E. B. Easton, Z. Qi, A. Kaufman, and P. G. Pickup, *Electrochem. Solid-State Lett.*, **4**, A59 (2001) http://esl.ecsdl.org/cgi/doi/10.1149/1.1361234.

103. Z. Xu, Z. Qi, and A. Kaufman, *Electrochem. Solid-State Lett.*, **6**, A171 (2003) http://esl.ecsdl.org/cgi/doi/10.1149/1.1592373.

104. Z. Xu, Z. Qi, and A. Kaufman, *Electrochem. Solid-State Lett.*, **8**, A313 (2005) http://esl.ecsdl.org/cgi/doi/10.1149/1.1912018.

105. L. Zhang, C. Song, J. Zhang, and H. Wang, *Jounal Electrochem. Soc.*, **152**, A2421–A2426 (2005).

106. J. Zhang and F. C. Anson, *Jounal Electroanal. Chem.*, **341**, 323–341 (1992).

107. Y. Lei and F. C. Anson, *Inorg. Chem.*, **33**, 5003–5009 (1994).

108. S. Turley et al., *J. Mol. Biol.*, **200**, 417–419 (1988).

109. A. D. Modestov, A. V. Kapustin, V. B. Avakov, I. K. Landgraf, and M. R. Tarasevich, *J. Power Sources*, **272**, 735–742 (2014) http://linkinghub.elsevier.com/retrieve/pii/S0378775314013780.

110. J. Xie et al., *Electrochim. Acta*, **55**, 7404–7412 (2010) http://linkinghub.elsevier.com/retrieve/pii/S0013468610008832.

111. B. Ding et al., *Cryst. Growth Des.*, **9**, 593–601 (2009).

112. M. Boudart, *Chem. Rev.*, **95**, 661–666 (1995) http://pubs.acs.org/doi/abs/10.1021/cr00035a009.

113. A. J. Bard and L. R. Faulkner, *Electrochemical Methods: Fundamentals and Applications*, Wiley, (2000) http://books.google.com/books?id=kv56QgAACAAJ.

114. B. Bleaney and K. D. Bowers, *Proc. R. Soc. A Math. Phys. Eng. Sci.*, **214**, 451–465 (1952) http://rspa.royalsocietypublishing.org/cgi/doi/10.1098/rspa.1952.0181.

115. P. Sharrock and M. Melnik, *Can. J. Chem.*, **63**, 52–56 (1985).

116. F. Strobridge, N. Judas, and T. Friscic, *CrystEngComm*, **12**, 2288 (2010) http://xlink.rsc.org/?DOI=c001020k.

117. A. Damjanovic and M. A. Genshaw, *Electrochim. Acta*, **15**, 1281–1283 (1970).

118. A. Damjanovic, D. B. Sepa, and M. V. Vojnovic, *Electrochim. Acta*, **24**, 887–889 (1979).

119. a. Damjanovic, *J. Chem. Phys.*, **45**, 4057 (1966) http://scitation.aip.org/content/aip/journal/jcp/45/11/10.1063/1.1727457.

120. H. S. Wroblowa and G. Razumney, *J. Electroanal. Chem. Interfacial Electrochem.*, **69**, 195–201 (1976) http://linkinghub.elsevier.com/retrieve/pii/S0022072876802501.

121. N. A. Anastasijevic, V. Vesovic, and R. R. Adzic, *Jounal Electroanal. Chem.*, **229**, 317–325 (1987).

122. N. A. Anastasijevic, V. Vesovic, and R. R. Adzic, *Jounal Electroanal. Chem.*, **229**, 305–316 (1987).

123. H. Behret, H. Binder, G. Sandstede, and G. G. Scherer, *J. Electroanal. Chem.*, **117**, 29–42 (1981).

124. H. Behret, H. Binder, W. Clauberg, and G. Sandstede, *Electrochim. Acta*, **23**, 1023–1029 (1978).

125. D. Sepa, M. Vojnovic, and A. Damjanovic, *Electrochim. Acta*, **25**, 1491–1496 (1980).

126. A. Damjanovic and M. A. Genshaw, *Jounal Electrochem. Soc.*, **114**, 1107–1112 (1968).

127. A. Serov, U. Tylus, K. Artyushkova, S. Mukerjee, and P. Atanassov, *Appl. Catal. B Environ.*, **150-151**, 179–186 (2014) http://linkinghub.elsevier.com/retrieve/pii/S0926337313007546.

128. M. H. Robson, A. Serov, K. Artyushkova, and P. Atanassov, *Electrochim. Acta*, **90**, 656–665 (2013) http://linkinghub.elsevier.com/retrieve/pii/S0013468612018191.

129. G. a. Goenaga et al., *ECS Electrochem. Lett.*, **3**, F68–F71 (2014) http://eel.ecsdl.org/cgi/doi/10.1149/2.0071411eel.

130. C. C. L. McCrory et al., *J. Am. Chem. Soc.*, **133**, 3696–9 (2011) http://www.pubmedcentral.nih.gov/articlerender.fcgi?artid=3077299&tool=pmcentrez&rendertype=abstract.

131. J. P. Collman, R. Boulatov, and C. J. Sunderland, *Porphyr. Handb. biosynthesis, Struct. Degrad. Vol. 13, Chlorophylls bilins biosynthesis, Synth. Degrad. Vol. 14, Med. Asp. porphyrins Vol. 15, Phthalocyanines Synth. Vol. 16, Phthalocyanines Spectrosc.*, 1 (2003).

132. J. H. Zagal and G. I. Cárdenas-Jirón, *J. Electroanal. Chem.*, **489**, 96–100 (2000) http://linkinghub.elsevier.com/retrieve/pii/S0022072800002096.

133. R. Baker, D. Wilkinson, and J. Zhang, *Electrochim. Acta*, **53**, 6906–6919 (2008) http://linkinghub.elsevier.com/retrieve/pii/S001346860800131X.

134. a. Lalitha, S. Ramesh, and S. Rajeswari, *Electrochim. Acta*, **51**, 47–55 (2005) http://linkinghub.elsevier.com/retrieve/pii/S0013468605003403.

135. J. A. Hendricks, S. V Gullà, D. E. Budil, and R. N. Hanson, *Bioorg. Med. Chem. Lett.*, **22**, 1743–6 (2012).

136. Y. Sueishi, S. Iwamoto, K. Miyazono, S. Nakatani, and K. Nakagawa, *Colloids Surfaces A Physicochem. Eng. Asp.*, **415**, 262–267 (2012).

137. J. S. Lawton and D. E. Budil, *J. Memb. Sci.*, **357**, 47–53 (2010).

138. J. S. Lawton and D. E. Budil, *Macromolecules*, **43**, 652–661 (2010).

139. K. Dyrek and M. Che, *Chem. Rev.*, **97**, 305–332 (1997).

140. J. S. Lawton, D. S. Aaron, Z. Tang, and T. A. Zawodzinski, *J. Memb. Sci.*, **428**, 38–45 (2013).

141. P. Basu, *J. Chem. Educ.*, **78**, 666–669 (2001).

142. E. T. Valdes and G. C. Trivino, *J. chile Chem. Soc.*, **541**, 1–5 (2009).

143. E. Garribba and G. Micera, *J. Chem. Educ.*, **83**, 1229–1232 (2006).

144. S. Stoll and A. Schweiger, *J. Magn. Reson.*, **178**, 42–55 (2006) http://www.ncbi.nlm.nih.gov/pubmed/16188474.

145. L. Guennoun et al., *Spectrochim. Acta. A. Mol. Biomol. Spectrosc.*, **78**, 347–53 (2011) http://www.ncbi.nlm.nih.gov/pubmed/21112810.

146. H. A. Hassan, *J. Al-Nahrain Univ.*, **16**, 53–59 (2013).

147. M. Al-Ajely, H. Al-Ajely, and A. Al-Naib, *J. pure Sci.*, **13** (2008).

148. W. Qian and S. Krimm, *Biopolymers*, **32**, 1503–1518 (1992).

149. O. Cretu, S. Barbuceanu, G. Saramet, and C. Draghici, *J. Serbian Chem. Soc.*, **75**, 1463–1471 (2010) http://www.doiserbia.nb.rs/Article.aspx?ID=0352-51391000122C.

150. J. Yoon and E. I. Solomon, *Coord. Chem. Rev.*, **251**, 379–400 (2007) http://linkinghub.elsevier.com/retrieve/pii/S0010854506001172.

151. J. Yoon, S. Fujii, and E. I. Solomon, *PNAS*, **106**, 6585–6590 (2009).

152. D. Ajo, A. Bencini, and F. Mani, *Inorg. Chem.*, **27**, 2437–2444 (1988).

153. S. Eaton, K. More, B. Sawant, and G. Eaton, *J. Am. Chemitry Soc.*, **105**, 6560–6567 (1983).

154. Bj. Mcvie, R. Sinclair, and T. G. Truscott, *J. Chem. Soc. Faraday Trans. 2*, **74**, 1870–1879 (1978).

155. M. Valko, P. Pelikan, S. Biskupic, and M. Mazur, *Chem. Pap.*, **44**, 805–813 (1990).

156. E. Garribba and G. Micera, *J. Chem. Educ.*, **83**, 1229 (2006) http://pubs.acs.org/doi/abs/10.1021/ed083p1229.

157. L. Najder-Kozdrowska, B. Pilawa, A. B. Więckowski, E. Buszman, and D. Wrześniok, *Appl. Magn. Reson.*, **36**, 81–88 (2009) http://link.springer.com/10.1007/s00723-009-0001-y.

158. D. Osiro, R. Franco, and A. Colnago, *J. Brazilian Chem. Soc.*, **22**, 1339–1345 (2011).

159. E. Coronado, M. Giménez-Marqués, G. M. Espallargas, and L. Brammer, *Nat. Commun.*, **3**, 828 (2012) http://www.ncbi.nlm.nih.gov/pubmed/22569372.

160. V. Bagchi, A. M. Bond, and F. Scholz, *Electroanalysis*, **1**, 1–11 (1988).

161. R. Wadhawan, J.; Compton, J. D. Compton, Richard G. Wadhawan, Editor. *Encycl. Electrochem.*, **2**, 170–220 (2003).

162. P. R. Murray and L. J. Yellowlees, in *Spectroelectrochemistry*, W. Kaim and A. Klein, Editors, p. 207–231, Royal Society of Chemistry, Cambridge (2008) http://ebook.rsc.org/?DOI=10.1039/9781847558404.

163. E. M. Erickson et al., *J. Am. Chem. Soc.*, **134**, 197–200 (2012) http://www.ncbi.nlm.nih.gov/pubmed/22188603.

164. H. Niwa et al., *Electrochem. commun.*, **35**, 57–60 (2013) http://linkinghub.elsevier.com/retrieve/pii/S138824811300307X.

165. A. Panchenko, H. Dilger, E. Möller, T. Sixt, and E. Roduner, *J. Power Sources*, **127**, 325–330 (2004).

166. M. Danilczuk, S. Schlick, and F. D. Coms, *Macromolecules*, **46**, 6110–6117 (2013).

167. L. Lin, M. Danilczuk, and S. Schlick, *J. Power Sources*, **233**, 98–103 (2013).

168. I. B. Goldberg and A. J. Bard, *J. Phys. Chem. B*, **76**, 3281–3290 (1971).

169. S. Allendoerfer, R., Martinchek, G., Bruckenstein, *Anal. Chem.*, **47**, 890–894 (1975).

170. I. B. Goldberg, D. Boyd, R. Hirasawa, and A. J. Bard, *J. Phys. Chem.*, **78**, 295–299 (1974).

171. B. A. Coles and R. G. Compton, *Jounal Electroanal. Chem.*, **144**, 87–98 (1983).

172. R. G. Compton, D. J. Page, and G. R. Sealy, *J. Electroanal. Chem. Interfacial Electrochem.*, **163**, 65–75 (1984) http://linkinghub.elsevier.com/retrieve/pii/S002207288480042X.

173. U. I. Kramm et al., *J. Electrochem. Soc.*, **158**, B69 (2011) http://link.aip.org/link/JESOAN/v158/i1/pB69/s1&Agg=doi.

174. R. G. Compton and A. M. Waller, *J. Electroanal. Chem. Interfacial Electrochem.*, **195**, 289–297 (1985) http://linkinghub.elsevier.com/retrieve/pii/0022072885800498.

175. U. Sakaguchi and A. W. Addison, *J. Chem. Soc. Dalt. Trans.*, 600–608 (1979).

176. L. . Philip, L. . Iyengar, and C. Venkobachar, *Water. Air. Soil Pollut.*, **119**, 11–21 (2000).

177. M. Setaka and T. Kwan, *Bull. Chem. Soc. Jpn.*, **43**, 2727–2731 (1970).

178. A. J. Tench and T. Lawson, *Chem. Phys. Lett.*, **8** (1971).

179. C. Zhang, J. Lawton, S. Foister, and T. Zawodzinski, *ECS Electrochem. Lett.*, Under revision (2014).

VITA

Congling Zhang was born in a town named Dongqiao in the city of Zhongxiang and raised in the city of Suizhou, Hubei, China. She attended the Second High School of Suizhou before entering Huazhong Agricultural University in Wuhan, Hubei. She worked in the lab, 'Laboratory of Biomass and Bioenergy' which is led by Prof. Liangcai Peng when she was a senior. She earned her Bachelor of Science degree in Applied Chemistry from Huazhong Agricultural University in 2010. She accepted a graduate assistantship at The University of Tennessee, Knoxville, then joined the research group led by Prof. Thomas Zawodzinski in the Department of Chemical and Biomolecular Engineering. She is currently a PhD candidate in Chemical Engineering in The University of Tennessee.